The Dissertation Committee for Nevena Ostojic Certifies that this is the approved version of the following Dissertation:

Electrocatalytic Reduction of Oxygen on Metal Nanoparticles in the Absence and Presence of Interactions with Metal-Oxide Supports

Committee:

Richard M. Crooks, Supervisor

Graeme Henkelman

Buddy Mullins

Michael Rose

Lauren Webb

Electrocatalytic Reduction of Oxygen on Metal Nanoparticles in the Absence and Presence of Interactions with Metal-Oxide Supports

by

Nevena Ostojic

Dissertation

Presented to the Faculty of the Graduate School of

The University of Texas at Austin

in Partial Fulfillment

of the Requirements

for the Degree of

Doctor of Philosophy

The University of Texas at Austin

August, 2018

Dedication

To my husband, my parents, and my sister.

Acknowledgements

First, I would like to express my sincere gratitude to my advisor, Dr. Richard Crooks, for the guidance, advice, encouragement, and many opportunities he has provided me with throughout my graduate education. You have been very understanding and helped me through some difficult times which allowed me to focus on the research and become a better scientist. I will always be grateful for that.

I would also like to thank Drs. Graeme Henkelman, Buddy Mullins, Michael Rose, and Lauren Webb for serving on my committee. Additionally, I would like to acknowledge Dr. Henkelman and Dr. Zhiyao Duan of the Henkelman group for their feedback, insight, and enthusiasm during our collaborative project.

I also wish to thank my entire research group and Angela Missildine, who all made my time spent in graduate school very enjoyable. I would specifically like to acknowledge my collaborators, Dr. Morgan Anderson and Aigerim Galyamova.

Importantly, I would like to express my sincere gratitude to my parents, who have always believed in me, provided me with opportunities, and inspired me to overcome any barriers. I would love to acknowledge my sister who has been working tirelessly to take care of my parents so that I can focus on graduate school. I will always be indebted to you. I would like to thank my husband who has been my biggest supporter and who believed in me even when I did not believe in myself. You and Olive have been the main source of my strength throughout graduate school.

Finally, I would like to acknowledge the U.S. Department of Energy and the Robert A. Welch Foundation for their financial support that made the realization of this project possible.

Abstract

Electrocatalytic Reduction of Oxygen on Metal Nanoparticles in the Absence and Presence of Interactions with Metal-Oxide Supports

Nevena Ostojic, PhD

The University of Texas at Austin, 2018

Supervisor: Richard M. Crooks

A combined experimental and theoretical approach is reported with a goal to develop a deeper understanding of strong metal support interactions (SMSI) and particularly their role in the oxygen reduction reaction (ORR). This was accomplished by developing a well-defined experimental system that can almost perfectly be modeled using first principles theory.

First, an electrocatalytic model was constructed based on NP-mediated electron transfer (eT). That is, thin films of Al_2O_3 (2.5-5.7 nm) were deposited onto pyrolyzed photoresist film (PPF) electrodes resulting in passivation of faradaic current. Next, previously passivated eT was recovered by immobilizing dendrimer-encapsulated PtNPs (Pt DENs) (1.3 nm) onto the Al_2O_3 surface. The resulting PPF/Al_2O_3/Pt DENs electrodes were stable under various electrochemical conditions and showed an activity for the ORR.

When DENs are immobilized onto solid supports, the dendrimers prevent direct contact between the encapsulated NPs and underlying supports. Consequently, in such systems, SMSI are not observed. Therefore, in the next step of the study we developed an

ultraviolet/ozone (UV/O_3)-based procedure that allows for the removal of dendrimers, as confirmed by X-ray photoelectron spectroscopy (XPS), without affecting shape, size, or composition of the encapsulated NPs.

Third, electrocatalytic activity of a PPF/Al_2O_3/G6-OH(Pt_{55}) electrode was studied before and after the UV/O_3 treatment using a novel microelectrochemical flow cell. The results indicated that direct interactions between Al_2O_3 and PtNPs do not affect the reaction pathway for the ORR. This was indeed anticipated because Al_2O_3 is a non-reducible oxide and will be used in the future studies as a control metal-oxide support.

Finally, we switched to a theory-first approach in which density function theory (DFT) was used to predict catalysts having desired properties based on the previously discussed experimental model. Based on the results of the DFT calculations, a PPF/SnO_x ($x = 1.9$ or 2.0)/Au_{147} DEN system was studied before and after the removal of dendrimers. Experimental results indicated that improvements in activity for the ORR were observed when Au_{147} NPs interacted directly with SnO_x supports. Moreover, XPS studies showed that the observed catalytic enhancements were due to eT from surface oxygen vacancies in SnO_x to Au_{147} NPs. These experimental results agreed with the theoretical predictions.

Table of Contents

List of Tables xii

List of Figures xiii

List of Illustrations xvi

Chapter 1. Introduction 1

Motivation and Objectives 1

Poly(amidoamine) (PAMAM) Dendrimers 3

Dendrimer-Encapsulated Nanoparticles (DENs) 4

Atomic Layer Deposition (ALD) 6

Nanoparticle-Mediated Electron Transfer 8

Oxygen Reduction Reaction 11

Strong-Metal-Support-Interactions (SMSI) 12

Chapter 2. Experimental 14

Chemicals 13

Fabrication of Pyrolyzed Photoresist Film (PPF) Electrodes 15

Deposition of $Al_{2.0}O_{3.0}$, $SnO_{1.7}$, $SnO_{2.0}$ Films on PPF Electrodes 15

Synthesis of Pt DENs 16

Characterization of Au and Pt DENs 17

Chapter 3. Electron Transfer Facilitated by Dendrimer-Encapsulated Pt Nanoparticles Across Ultrathin, Insulating Oxide Films 18

Introduction 18

Experimental 22

Activation of PPF Electrodes 22

Surface Characterization....22
Electrochemical Characterization....23
Results and Disscussion....24
Characterization of PPF Elctrodes....24
Properties and Stability of Al_2O_3 ALD Films....27
Immobilization and Characterization of Pt DENs atop Al_2O_3-Modified PPF Electrodes....31
Pt DENs-Mediated eT....35
Location of Pt DENs....37
Effect of Al_2O_3 Thickness on Pt-DENs Mediated eT....38
The ORR at a Reactivated Al_2O_3 Thin Film Electrodes....40
Summary and Conclusions....42
Chapter 4. Electrocatalytic Reduction of Oxygen on Platinum Nanoparticles in the Presence and Absence of Interactions with the Electrode Surface....44
Introduction....44
Experimental....48
UV/O_3 Treatment....48
X-ray Photoelectron Spectroscopy (XPS)....48
Results and Disscussion....49
Effect of UV/O_3 on PPF Substrates....49
Effect of UV/O_3 on G6-OH Dendrimers....52
Effect of UV/O_3 on Pt DENs....56
Location of Pt DENs....59
The ORR in the Presence and Absence PtNP-PPF Support Interactions....61

Summary and Conclusions 64

Chapter 5. Microelectrochemical Flow Cell for Studying Electrocatalytic Reactions on Oxide-Coated Electrodes 66

Introduction.....66

Experimental.....71

Activation of PPF Electrodes.....71

Synthesis of Pt DENs.....71

UV/O_3 Treatment for Decomposition of G6-OH Dendrimers.....72

Flow Cell Design 73

Fabrication of Pt Collector Electrodes.....76

Results and Disscussion.....77

Flow Cell Design and Characterization 77

Decomposition of G6-OH Dendrimers.....81

Effect of UV/O_3 on Pt DENs and Al_2O_3.....84

Evaluation of the ORR Pathway in the Absence and Presence of Contact between PTNPs and the Al_2O_3 Support using the Levich Equation.....88

Evaluation of the ORR Pathway in the Absence and Presence of Contact between PTNPs and the Al_2O_3 Support using Generation-Collection ...91

Summary and Conclusions 95

Chapter 6. Electrocatalytic Study of the Oxygen Reduction Reaction at AuNPs in the Absence and Presence of Interactions with SnO_x Supports.....96

Introduction.....96

Experimental.....99

Computational Methods.....99

Deposition of SnO_x (x = 1.7 or 2.0) Films onto PPF Electrodes 102

Surface Characterization....102
Synthesis of Pt DENs....103
UV/O_3 Method for Decomposition of G6-NH_2 Dendrimers....105
Electrochemical Characterization....105
Results and Disscussion....106
Characterization Surface Pourbaix Diagram of SnO_2(110)....106
ORR Activity of SnO_2(110)....107
ORR Activity of Au_{147}....110
ORR Activity of Au/SnO_2....111
Characterization Surface Properties and Stability of SnO_x (x = 1.7 and 2.0)....116
Decomposition of G6-NH_2 Dendrimers....123
Effect of UV/O_3 Treatment on the Oxidation States of SnOx (x = 1.7 and 2.0) Films....124
Evaluation of the ORR Onset Potential and Kinetics in the Absence and Presence of Contact between AuNPs and SnO_x (x = 1.7, 1.9, and 2.0) Supports....127
Evaluation of the ORR Pathway in the Absence and Presence of Contact between AuNPs and SnO_x Supports....132
Electronic Interactions between AuNPs and $SnO_{1.7}$ and $SnO_{2.0}$ Supports..133
Summary and Conclusions....137
Chapter 7. Conclusion and Outlook....139
References....142

List of Tables

Table 1.1: Physical properties of amino-terminated PAMAM dendrimers (G0-G10) 4

Table 4.1: Summary of XPS Peak Assignments, Positions, Areas, and Concentrations for a PPF/G6-OH(Pt_{55}) Electrode before UV/O_3 Treatment 53

Table 4.2: Summary of XPS Peak Assignments, Positions, Areas, and Concentrations for a PPF/G6-OH(Pt_{55}) Electrode after UV/O_3 Treatment ..54

Table 6.1: Summary of XPS Sn 3d and O 1s atomic % concentrations and their ratios for PPF/$SnO_{1.7}$ and PPF/$SnO_{2.0}$ electrodes. 123

Table 6.2: Summary of XPS Sn 3d and O 1s atomic % concentrations and their ratios for PPF/$SnO_{1.7}$ and PPF/$SnO_{2.0}$ electrodes after the UV/O_3 treatment. 126

List of Figures

Figure 1.1: 7
Figure 1.2: 7
Figure 3.1: 25
Figure 3.2: 26
Figure 3.3: 27
Figure 3.4: 28
Figure 3.5: 29
Figure 3.6: 30
Figure 3.7: 31
Figure 3.8: 32
Figure 3.9: 33
Figure 3.10: 34
Figure 3.11: 36
Figure 3.12: 38
Figure 3.13: 39
Figure 3.14: 41
Figure 3.15: 42
Figure 4.1: 50
Figure 4.2: 51
Figure 4.3: 51
Figure 4.4: 56
Figure 4.5: 57
Figure 4.6: 59
Figure 4.7: 60

Figure 4.8: 63
Figure 4.9: 64
Figure 5.1: 72
Figure 5.2: 75
Figure 5.3: 76
Figure 5.4: 79
Figure 5.5: 81
Figure 5.6: 83
Figure 5.7: 86
Figure 5.8: 88
Figure 5.9: 90
Figure 5.10: 92
Figure 5.11: 93
Figure 5.12: 94
Figure 6.1: 101
Figure 6.2: 104
Figure 6.3: 107
Figure 6.4: 108
Figure 6.5: 109
Figure 6.6: 111
Figure 6.7: 113
Figure 6.8: 114
Figure 6.9: 115
Figure 6.10: 117
Figure 6.11: 119

Figure 6.12: 120
Figure 6.13: 121
Figure 6.14: 122
Figure 6.15: 124
Figure 6.16: 125
Figure 6.17: 129
Figure 6.18: 130
Figure 6.19: 131
Figure 6.20: 133
Figure 6.21: 135
Figure 6.22: 136
Figure 6.23: 137

List of Illustrations

Illustration 1.1: Schematic illustration of eT across an insulating layer in the absence and presence of a NP.....8

Illustration 3.1: Schematic illustration of eT across PPF/Al_2O_3 (top) and PPF/Al_2O_3/G6-OH(Pt_{55}) (bottom) electrodes. 18

Illustration 4.1: Schematic representation of G6-OH dendrimer removal from G6-OH(Pt_{55}) immobilized atop a PPF/Al_2O_3 electrode 44

Illustration 5.1: Schematic representation of a PPF/Al_2O_3/PtNPs electrode after the removal of the dendrimers 68

Illustration 5.2: Schematic illustration of (a) individual pieces of the microelectrochemical flow cell and (b) the side view of the flow cell ...70

Illustration 6.1: Schematic representation of a PPF/SnO_x/G6-NH_2(Au_{147}) electrode. 98

Illustration 6.2: Schematic representation of (a) PPF/$SnO_{1.7}$/G6-NH_2(Au_{147}) and (b) PPF/$SnO_{2.0}$/G6-NH_2(Au_{147}) electrodes before and after the UV/O_3 treatment. 127

Chapter 1: Introduction

MOTIVATION AND OBJECTIVES

The role of catalysts is becoming increasingly important, especially in the power generation, automotive and chemical industries. Unfortunately, the main method of catalyst design is still costly and time-consuming process of trial and error. What is needed is the development of an efficient and controlled approach that would lower the existing costs of catalysts design. Although computational methods and their speed are rapidly advancing, first principle calculations played a role in designs of only a few technical catalysts.[1] This is the justification for the study presented here - close collaboration between well-defined experimental methods and advance theory is the most productive way towards an efficient catalysts design.

However, development and characterization of an electrocatalytic experimental model against which theoretical predictions can be tested is very challenging. And this becomes even harder when it comes to including the support interactions in studying and understanding catalyst function. Strong metal support interactions (SMSI)[2–4] have attracted high research interest over the past four decades as an efficient means to improve catalyst activity in the field of gas-phase catalysis. However, such interactions are still not well understood and pose a challenge for both theory and experiment.[2,4] Understanding SMSI becomes even more challenging within the field of electrochemistry. This is because it is more difficult to prepare well-defined electrocatalyst models, and theoretical modeling of experimental results is more difficult in condensed phase. Therefore, a well-defined electrocatalyst model that would allow further understanding, control, and adjustment of SMSI is essential. This model would

also need to correlate very well to the first principle calculations.

Considerable portion of electrocatalytic studies on SMSI have been focusing on the oxygen reduction reaction (ORR)[5–7]. The ORR is a crucial reaction in electrochemical energy conversion, and it is the greatest source of inefficiency in fuel cells.[5] Recently, experimental achievements regarding the ORR have been predominantly led by theoretical works.[8] However, theoretical efforts have not been specifically focused on understanding the importance of reducible oxide supports in the ORR. On the other hand, experimental studies have established that supports can improve catalyst activity towards the ORR in several ways.[2,9] For instance, catalyst electronic properties can be tuned or the support itself can participate in electrocatalytic reactions, both resulting in improved ORR rates at low overpotentials. However, rate limiting steps in the ORR catalyzed at metal-oxide/metal composites are still not clear, and a collaborative experimental/theoretical approach would be an effective way towards addressing numerous unanswered questions in this field.

It is important to point out that the goal of this study is not to develop technical catalysts for commercial applications. Instead, this is a fundamental study, focusing on a collaboration between experiment and theory, with a goal to get to the point where theory will be leading experimental research. Several goals were accomplished in this work. First, an experimental electrocatalyst model partially based on nanoparticle (NP)-mediated electron transfer (eT) recovery was developed and characterized. The model consisted of an Al_2O_3 film with overlying dendrimer-encapsulated PtNPs (Pt DENs). Although dendrimers prevented direct contact between the encapsulated PtNPs and underlying Al_2O_3, the electrochemical construct was active for the ORR (Chapter III).

Second, a UV/O_3-based method was introduced allowing for removal of

dendrimers from DENs immobilized onto solid supports. Removal of the dendrimers is of critical importance as it provides a means to control interactions between NPs and their metal-oxide (MO) supports. Consequently, this allows the study of electrocatalytic reactions in the absence and presence of SMSI interactions (Chapter IV). Next, a novel dual-electrode microfluidic flow cell is introduced, which allows for a simultaneous study of kinetics and the mechanism of electrocatalytic reactions at complex surface modifications. Correspondingly, using the microfluidic flow cell, PtNPs activity for the ORR in the absence and presence of interactions with Al_2O_3 was studied (Chapter V). Finally, we switched to a theory-first approach, and based on the results of first principles calculations, we experimentally studied the effects of SnO_x (x = 1.9 or 2.0) supports on electrocatalytic activity of AuNPs for the ORR. The results of the experimental study converged well with the first principle theory predictions (Chapter VI).

POLY(AMIDOAMINE) (PAMAM) DENDRIMERS

First introduced by Vogtle in 1978,[10] dendrimers are highly monodisperse, spherically shaped (Generation 4 and above), tree-like macromolecules. In this work we used poly(amidoamine) (PAMAM) dendrimers which are synthesized using a divergent approach involving the growth of a molecule from the center to the periphery.[11] Dendrimers are synthesized in a repeated sequence of reaction steps, where each additional reaction sequence leads to a higher generation of dendrimer with a larger diameter. Dendrimers consist of three main parts: core, interior, and periphery. PAMAM dendrimers are composed of alkyl-diamine core and tertiary amine branches. Their periphery consists of tens to thousands of individual functional groups which can be

modified to adjust physical and chemical properties of the dendrimer. Table 1.1[12] shows certain properties of amine-terminated PAMAM dendrimers by generation.

Generation	Diameter (nm)	Number of Surface Groups
0	1.5	4
1	2.2	8
2	2.9	16
3	3.6	32
4	4.5	64
5	5.4	128
6	6.7	256
7	8.1	512
8	9.7	1024
9	11.4	2048
10	13.5	4096

Table 1.1: Physical properties of amino-terminated PAMAM dendrimers (G0-G10).

DENDRIMER-ENCAPSULATED NANOPARTICLES (DENS)

Dendrimers have been widely used as hosts for the synthesis of NPs. In this report hydroxyl and amino-terminated PAMAM dendrimers are used for the synthesis of Pt and Au DENs. Synthesis of dendrimer-encapsulated NPs (DENs) usually consists of two steps.[13] First, a precursor metal salt is mixed with dendrimer solution in a desired

stochiometric ratio. During this step, metal ions complex with the interior amine groups of the dendrimer. During the second step, a chemical reducing agent (e.g. BH_4^-) is added leading to reduction of the precursor ions and subsequent agglomeration of the resulting atoms to form dendrimer-encapsulated nanoparticles. This procedure usually leads to formation of completely reduced metal NPs (like Cu[14,15] and Au[16,17]). However, in the case of PtNPs this synthesis route results in formation of both fully reduced DENs and unreduced Pt^{2+} within the dendrimers.[18] Nonetheless, the Crooks group reported a method, based on galvanic exchange, that allows the synthesis of completely reduced Pt DENs.[13,15] Briefly, Cu DENs are formed using the previously described two-step process, and then Pt salts (like $PtCl_4^{2-}$) are added to initiate galvanic exchange. That is, Pt has a more positive reduction potential compared to Cu, and therefore Cu DENs are oxidized to form Cu^{2+} and Pt salts are reduced to zero-valent Pt.

DENs offer multiple advantages over other methods of preparing NPs, including: (1) size of the encapsulated NPs can be closely controlled by the dendrimer template: metal ion ratio and by the generation of the dendrimer;[11,13] (2) fairly monodisperse NPs containing an average of 147 atoms can be synthesized, making them ideal for modeling by density function theory (DFT);[17,19] (3) the peripheral groups of dendrimers can be used to immobilize DENs onto solid surfaces allowing their use in heterogeneous catalysis and preventing direct contact between the encapsulated NPs and underlying surfaces during such catalytic reactions;[11,20] (4) encapsulated NPs are confined within the dendrimers by steric effects, therefore most of the NP surface is catalytically active and its electronic properties are not affected by the dendrimer.[20,21] Importantly, as DENs are well-defined in size, structure, and composition, they are a good model for establishing structure−function relationships. Finally, due to these advantages, it has been previously

shown that properties of DENs measured experimentally correlate well with first principles theory predictions.[22,23]

ATOMIC LAYER DEPOSITION (ALD)

Atomic layer deposition (ALD) is a chemical vapor deposition (CVD)-based technique that is believed to form pinhole-free, atomically smooth, and ultra-thin films.[24,25] The ability of ALD to evenly coat substrates having complex shapes arises from its self-limiting growth mechanism.[26,27] That is, one cycle of ALD consists of sequential, self-limiting reactions occurring between gas-phase precursors and a solid substrate. The ALD process begins with introduction of a gas-phase metal precursor to a substrate, resulting in a self-limited formation of a monolayer. Unreacted precursor molecules and gaseous-reaction byproducts are then removed in a purge step with N_2. Next, an oxygen source (e.g., H_2O, H_2O_2, O_2, O_3, etc.) is introduced into the ALD chamber to activate the surface for the next introduction of the metal-precursor. Finally, the chamber is purged again with N_2. An ALD cycle can be repeated until desired film thickness is reached.

The composition of deposited materials can be precisely controlled during ALD. This is accomplished by controlling the length of each of the previously discussed four steps that make up one ALD cycle, as well as by the choice of a metal precursor and oxygen source. In this work, we focus on depositing Al_2O_3 and $SnO_{1.7}$ ALD films, therefore metal precursors used for formation of these films were trimethylaluminum (TMA) (Figure 1.1) and tetrakis(dimethylamino)tin(IV) (TDMASn) (Figure 1.2), respectively.

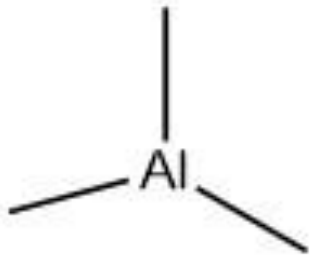

Figure 1.1: Chemical structure of trimethylaluminum (TMA).

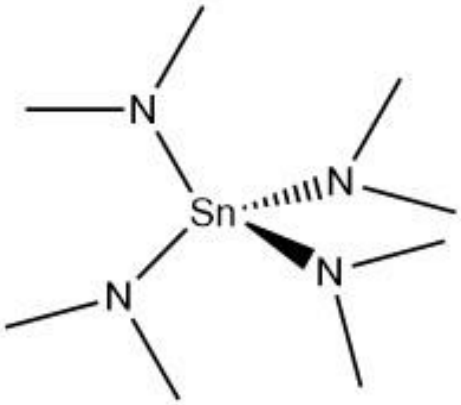

Figure 1.2: Chemical structure of tetrakis(dimethylamino)tin (TDMASn).

As mentioned before, the choice of the oxygen source can play an important role in the composition and stoichiometry of ALD films. Oxygen sources used in this research were O_3 (for deposition of Al_2O_3) and H_2O (for $SnO_{1.7}$). O_3 offers several advantages over H_2O as an ALD precursor. For example, risks of hydrogen and hydroxyl contaminations are reduced when O_3 is used. Moreover, O_3 is highly volatile and a strong oxidizing agent resulting in shorter ADL steps.[26,28] Finally, films formed with O_3 exhibit lower defect density, less problems with delamination, and lower electrochemical leakage

currents.[28] However, even though O_3 offers multiple discussed advantages, production of O_3 at a point of use is more complicated, compared to H_2O, as it requires an O_3-generator.

NP-MEDIATED ELECTRON TRANSFER (ET)

In 1996, Nathan and coworkers reported that a polymerized silane film can completely passivate a platinum electrode so that no appreciable faradaic electrochemistry occurs between the electrode and methyl viologen in solution.[29] Interestingly, however, upon immobilization of gold or silver NPs onto the polymerized silane the previously passivated electron transfer (eT) was fully recovered (Illustration 1.1).

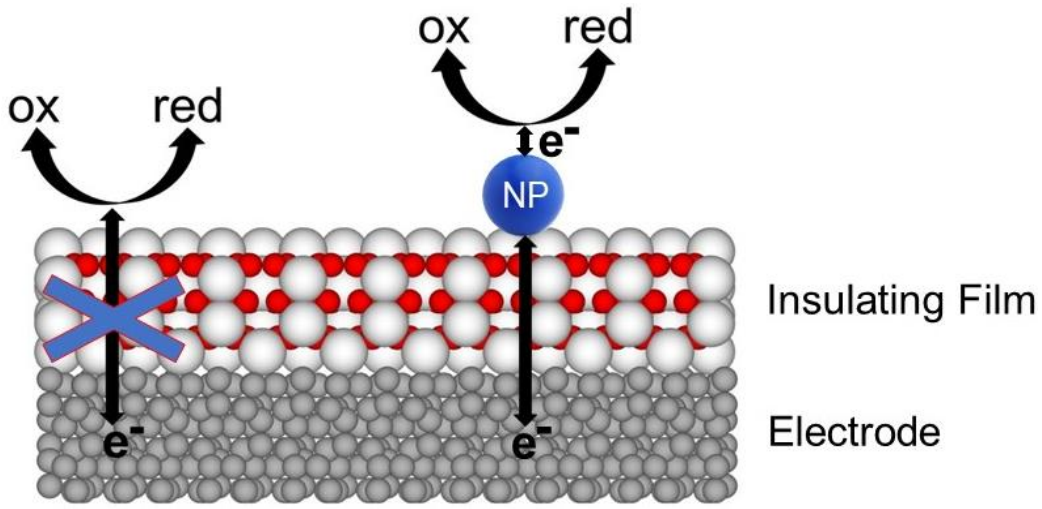

Illustration 1.1: Schematic illustration of eT across an insulating layer in the absence and presence of a NP.

The group further extended their research to show that changes in substrates,

functional groups of the insulating layer, and NP diameter (12-20 nm) do not influence the overall electrochemical behavior of the system. However, interest in this type of electrode/insulator/NP constructs did not peak until 12 years later when the Fermin[30–32] and the Gooding[33,34] groups independently started studying dependence of NP-mediated eT on the thickness of the insulating layer. They showed that in the absence of NPs the expected relationship between current and insulating film thickness still holds (Equation 1.1)[35]:

$$i \propto \exp^{-\beta d} \tag{1.1}$$

where β is electron tunneling constant and d is thickness of the insulating film. However, what attracted considerable research interest were the reports from both, the Fermin and the Gooding, groups claiming that an eT between a supporting metal electrode and an adsorbed NP is distance independent across ultra-thin self-assembled monolayers (SAMs). The Fermin group further showed that a few % NP coverage is enough to efficiently promote eT recovery.

What followed in the next few years, was worldwide experimental efforts aiming to explain the observed phenomenon. An explanation was finally provided in 2010 by Chazalviel's and Allongue's theoretical publication.[35] The key point of this publication was that an eT between two metallic phases, under an applied potential difference, is much easier than eT between a metal and a dilute redox species in solution. Chazalviel and Allongue proved this point by calculating potential/current density relations for a metal modified with a SAM layer in the absence and presence of a metal overlayer (metal/SAM and metal/SAM/metal, respectively).

In the case of a metal/SAM interface, the potential/current density relation can be represented as Equation 1.2.[35]

$$V = \frac{2k_BT}{q}\sinh^{-1}\left(\frac{J}{2J_0 exp^{-\beta d}}\right) \quad (1.2)$$

In this equation, V is overpotential, k_B is Boltzmann's constant, T is the absolute temperature, q is the elementary charge, J is the current density, J_0 is the current density at metal/SAM, β is an attenuation factor, and d is the thickness of the organic layer. For the alkyl chains used for these calculations, β ~1Å^{-1}.[35] Furthermore, assuming that the SAM is composed of an alkyl chain having 10 carbons, d is on the order of 10^{-6}, meaning that the exchange current density is on the order of 10-100 nA/cm^2.[35] Therefore, obtaining current densities larger than just a few μA/cm^2 would require large overpotentials. This explains the experimentally observed flattening of current once SAMs are deposited atop a metal electrode.

On the other hand, in case of a metal/SAM/metal construct there are going to be two contributors to the potential, the electrochemical interface and the potential drop across the insulating layer (Equation 1.3):[35]

$$V = \frac{k_BT}{q}\left[2\sinh^{-1}\left(\frac{J}{2J_0}\right) + \frac{J}{J_1 exp^{-\beta d}}\right] \quad (1.3)$$

where, J_1 is the current density across metal/SAM/metal construct. J_1 is usually ~10^{10} A/cm^2,[35] meaning that $J_1 exp^{-\beta d}$ is much larger than J and that value of the second term (the potential drop across the insulating layer) in Equation 1.3 is very small. Therefore, any potential applied to a metal/SAM/metal electrode appears almost completely at the top of the construct; that is, at the NP surface. So, distance-independent eT is observed until conditions of Equation 1.3 fail. These conditions will fail with very thick insulating layers or very small NPs (~1 nm). However, the NP requirements holds only for very monodisperse NPs, and just a few NPs with diameter above 1 nm would be enough to keep the NP-condition of the Equation 1.3 from failing.[35]

OXYGEN REDUCTION REACTION (ORR)

The oxygen reduction reaction (ORR)[36–38] is of central importance in energy conversion systems such as fuel cells. The focus of this research is on the ORR in aqueous solutions where the ORR occurs via one of the two main pathways: the 4-electron transfer to directly produce H_2O (Equation 1.4)[37]:

$$O_2 + 4e^- + 4H^+ \leftrightarrow 2H_2O \qquad E^0 = 1.23 \text{ vs SHE} \qquad (1.4)$$

or the 2-electron transfer to produce H_2O_2 (Equation 1.5)[37]:

$$O_2 + 2e^- + 2H^+ \leftrightarrow H_2O_2 \qquad E^0 = 0.70 \text{ vs SHE} \qquad (1.5)$$

However, the H_2O_2 resulting from Equation 1.5 may be further reduced to H_2O via an additional 2-electron transfer (Equation 1.6)[37]:

$$H_2O_2 + 2e^- + 2H^+ \leftrightarrow 2H_2O \qquad E^0 = 1.77 \text{ vs SHE} \qquad (1.6)$$

The ORR usually proceeds as a combination of the 4-electron and the 2-electron processes. Hence, there is always some H_2O_2 produced and the number of electrons exchanged during the ORR (n_{eff}) is usually less than 4.

The ORR is an electrochemical reaction occurring at the cathode of proton exchange membrane (PEM) fuel cells. However, this reaction is very sluggish on its own and it requires a catalyst. At the current stage of technology, Pt-based catalysts are still the best option available.[36] However, even when an all-Pt catalyst is used H_2O_2 still makes ~2% of the overall products[36] (n_{eff} ~3.9) and the onset potential is ~0.3 – 0.4 V below the reversible thermodynamic potential (1.23 V vs SHE).[7] Therefore, high loadings of this very expensive and scarce metal are usually required to reach practical current densities.[39] Correspondingly, there has been a lot of research focusing on development of alternative catalysts, either by incorporating non-precious metals into Pt nanostructures or by reducing the diameter of PtNPs to achieve high surface areas.

STRONG METAL SUPPORT INTERACTIONS (SMSI)

Although as early as in 1930s G.M. Schwab used the term "electronic factor" to explain experimentally observed catalytic behavior of supported catalysts,[4] strong metal support interactions (SMSI)[2,4,40,41] are usually dated back to S. J. Tauster in 1978 when he introduced the term to describe changes in catalytic behavior of group 8 metals supported on reducible metal-oxides.[42] Today, the definition of the SMSI is extended to include any effects that a support exerts on a metal catalyst during synthesis, heating, or a catalytic reaction.

Extensive experimental efforts have been applied in heterogeneous gas-phase catalysis toward understanding SMSI. However, the amount of research geared toward understanding the importance of these types of interactions in electrocatalysis has been significantly lower. Studying the role of SMSI in electrocatalytic reactions is more complicated for two main reasons: (i) it is very difficult to synthesize and efficiently characterize catalytic systems that exhibit SMSIs at the electrochemical interface; (ii) first-principle theory modeling of catalytic constructs and interpretation of catalytic results is far more challenging in condensed phase.

However, even from the limited studies that have been done on this topic, it is clear that supports may strongly influence intrinsic activity and selectivity of a supported catalyst. Although, SMSI are complex and still not well understood, reducible supports often affect the overlaying metal NPs a few main ways: (i) charge can be exchanged between a support and the overlying NPs affecting the catalyst electronic properties, (ii) supports can cause changes in the shape and structure of the NPs, (iii) support can

participate in a catalytic reaction by providing additional reaction sites or by stabilizing reaction intermediates. Although these are the most important factors governing SMSIs, they by no means entail the whole range of SMSIs. It is still not clear which support effects are most important and the effects of a reducible support on a metal NPs still cannot be accurately predicted. Therefore, further studies are necessary to understand how to efficiently utilize SMSI in electrocatalysis. That is the objective of this dissertation.

Chapter 2: Experimental

CHEMICALS

All chemicals were used as received. These include 1,1'-ferrocenedimethanol ($Fc(MeOH)_2$, 98%, Acros Organics, NY), 1-decanethiol (96%, Alfa Aesar), $HClO_4$ (+70%, ultrapure grade, J. T. Baker), NaOH (Fischer Scientific), and $NaBH_4$ (99.99% trace metals basis, Sigma Aldrich). The following were obtained from Sigma-Aldrich: $AgNO_3$ (99%), CH_2Cl_2, $CuSO_4$, $NaBH_4$, H_2SO_4 (+98%, trace metal grade), and K_2PtCl_4.

Trimethylaluminum (TMA) for ALD was obtained in sealed stainless-steel canisters from Sigma-Aldrich, while the tetrakis(dimethylamino) tin(IV) (99%, (99.99%-Sn)) (TDMASn) for ALD was obtained in a sealed stainless-steel canister from STREM Chemicals. High-purity (99.9999%) N_2 for ALD, high-purity (99.9999%) O_2 for ALD and UV/O_3 system, and a mixed 5% H_2/95% N_2 gas for pyrolysis of photoresists were purchased from Praxair (Austin, TX).

Quartz slides were purchased from Technical Glass Products (Painesville Twp, OH). AZ 1518 photoresist and AZ 400K developer (pre-diluted 1:4) were purchased from Integrated Micro Materials (Argyle, TX). Acrylic sheets and silicone gaskets were purchased from McMaster Carr (Atlanta, GA). NanoPorts and fluidic connections were purchased from Idex Health and Science (Oak Harbor, WA).

G6-OH and G6-NH_2 dendrimers were purchased as a 10-25% methanol solution from Dendritech, Inc. (Midland, MI). Prior to use, the methanol was removed under vacuum. National Exposure Research Laboratory (NERL) reagent-grade water from Thermo Scientific was used for the synthesis of DENs and all other aqueous solutions.

FABRICATION OF PYROLYZED PHOTORESIST FILM (PPF) ELECTRODES

Prior to photoresist deposition, quartz slides were cleaned sequentially in acetone, ethanol, and DI water for 10 min each. Next, the slides were rinsed under running DI water for 1 min and then heated at 200 °C for 15 min. After cooling to room temperature (24 ± 1 °C), positive-tone AZ 1518 photoresist was spin-coated onto the slides for 10 s at 500 rpm, 45 s at 3500 rpm, and for 5 s at 500 rpm. Finally, the slides were soft baked for 1 min at 100 °C and left to cool to room temperature. The last two steps were repeated a second time.

The photoresist-coated quartz slides were patterned by exposure to UV light through a photomask. Next, AZ 400 K developer, diluted to 25% (v/v) with DI water, was used to develop the exposed photoresist. Finally, the photoresist was pyrolyzed in a quartz tube furnace under a constant flow (100 sccm) of forming gas (5% H_2/95% N_2). The furnace temperature was increased from 25 °C to 1000 °C at 5 °C/min, held at 1000 °C for 1 h, and then cooled to 25 °C. The resulting PPF slide was then diced into individual electrodes using a diamond-tipped pen. The individual PPF electrodes were gently rinsed with NERL water and dried under flowing N_2.

DEPOSITION OF Al_2O_3, $SnO_{1.7}$, AND $SnO_{2.0}$ FILMS ONTO PPF ELECTRODES

Al_2O_3. Atomic layer deposition (ALD) was performed using a Savannah S100 Cambridge NanoTech ALD system (Ultratech, San Jose, CA). TMA was used as the Al source and O_3 as the oxygen source (neither reagent was heated). The ALD system was evacuated to <1 mmHg, and the patterned PPF substrates were heated to 150 °C for 4 min under a constant flow (20 sccm) of high-purity N_2. Next, the substrates were exposed to 10 cycles of O_3, each 15 ms long. Finally, each ALD cycle was carried out as follows: (1) a single 15 ms pulse of TMA, (2) a 20 s purge of N_2, (3) a 15 ms pulse of O_3, and (4) a 15

s purge of N_2. These four steps were repeated until the desired number of cycles had been achieved.

SnO_x (x = 1.7 or 2.0). TDMASn, heated to 60°C, used as the Sn source and H_2O as the oxygen source. The ALD system was evacuated to <1 mmHg, and a patterned PPF substrate was heated to 150 °C for 20 min under a constant flow (20 sccm) of high-purity N_2. Each ALD cycle was carried out as follows: (1) a single 0.015 s pulse of H_2O, (2) a 30 s purge of N_2, (3) a 0.5 s pulse of TDMASn, and (4) a 30 s purge of N_2. These four steps were repeated until the desired number of cycles had been achieved. This ALD procedure results in formation of $SnO_{1.7}$ films. The $SnO_{2.0}$ films were achieved by heating the $SnO_{1.7}$ films at 150°C for 60 min under a constant flow of oxygen (150 sccm).

SYNTHESIS OF PT DENS

Pt DENs were synthesized using a previously published procedure[18] based upon galvanic exchange. Specifically, 1.0 mL of 100.0 μM sixth-generation, hydroxyl-terminated (G6-OH) poly(amidoamine) (PAMAM) dendrimers was diluted in 8.68 mL of DI water. Next, 55 equiv of 20.0 mM $CuSO_4$ were pipetted into the G6-OH solution. The solution was sealed and stirred under N_2 for 15 min. Next, a 5-fold molar excess of an aqueous 1.0 M $NaBH_4$ solution was added dropwise under N_2 to reduce intradendrimer Cu_2^+ to CuNPs. The reduction was carried for 45 min, and then the pH of the resulting G6-OH(Cu_{55}) DENs was adjusted to 3.0 using 1.0 M $HClO_4$. Finally, sufficient aqueous 10.0 mM $PtCl_4^{2-}$ (Pt^{2+}:Cu = 1:1) was added dropwise (under N_2) to initiate galvanic exchange. The solution was sealed and left to stir for 60 min under N_2. The Pt DENs were immobilized atop PPF/Al_2O_3 electrodes by immersing the latter in the Pt DENs solution (pH 3.0) for 30 min. After 30 min, the electrodes were rinsed under a gentle flow

of NERL reagent-grade water and dried under low-pressure N_2. The newly formed PPF/Al_2O_3/G6-OH(Pt_{55}) electrodes were left to dry for at least 90 min prior to use.

CHARACTERIZATION OF AU AND PT DENS

Transmission Electron Microscopy (TEM) and Scanning Transmission Electron Microscopy (STEM) images were obtained using a JEOL-2010F transmission electron microscope having a point-to-point resolution of 0.19 nm. 2.0 μL of the G6-OH(Pt_{55}) or G6-NH_2(Au_{147}) solution was pipetted onto a lacey-carbon-over-Ni TEM grid (Electron Microscopy Sciences, Hatfield, PA). The samples were allowed to air-dry on the grid overnight prior to analysis.

Chapter 3: Electron Transfer Facilitated by Dendrimer-Encapsulated Pt Nanoparticles Across Ultrathin, Insulating Oxide Films[1]

INTRODUCTION

In this chapter we report that fully passivating, ultrathin (2.5 nm thick) Al_2O_3 layers can be deposited onto carbon electrodes via atomic layer deposition (ALD). More importantly, however, subsequent adsorption of Pt dendrimer-encapsulated nanoparticles (DENs)[11,17,43,44] onto the oxide surface leads to an electrocatalytically active interface (Illustration 3.1). These results are important, because they provide a general approach for studying electrocatalytic reactions on nonconductive oxide surfaces.

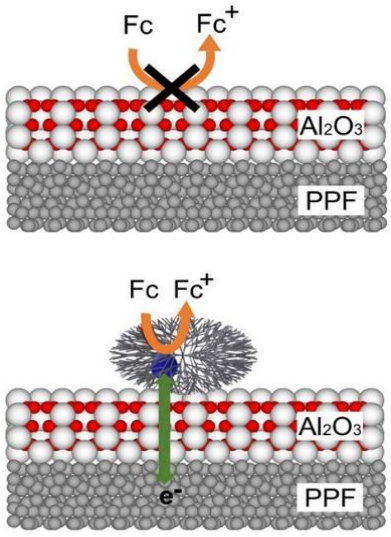

[1] Ostojic, N.; Thorpe, J. H.; Crooks, R. M. Electron Transfer Facilitated by Dendrimer-Encapsulated Pt Nanoparticles Across Ultrathin, Insulating Oxide Films. *JACS* **2016**, *138*, 6829–6837.
I was the primary author on this publication. J. H. Thorpe helped with data collection. Dr. R. M. Crooks was the project supervisor.

Illustration 3.1: Schematic illustration of eT across PPF/Al_2O_3 (top) and PPF/Al_2O_3/G6-OH(Pt_{55}) (bottom) electrodes.

The dendrimer-templating method was first introduced by our group in 1998,[19] and since then it has been extensively used for synthesizing a broad range of nanoparticles (NPs).[11,19,20,43] DENs are prepared by combining dendrimers and metal ions in fixed stoichiometric ratios, and then adding a reducing reagent to convert the metal ions to atoms. The atoms agglomerate within the dendrimer leading to particles in the size range of ∼0.5−2.2 nm. This is the important size range over which the catalytic properties of metals change quickly and in interesting ways.[2,45] Indeed, DENs are especially useful for understanding electrocatalytic reactions because they are well-defined in size, structure, and composition, and this in turn provides a means to establish structure−function relationships.[17,43,46–50] For the present study, the dendrimer host also provides important functions: stabilizing the DENs against aggregation and immobilizing them on the electrode surface via specific interactions with the oxide.

Although structurally not as well-defined as DENs, metal oxides deposited via ALD are the best option available for our planned electrocatalysis studies. Because it is electrically insulating and has a low dielectric constant, we[51] and others[52–54] have used Al_2O_3 for the purposes of hindering charge-transfer between an electrode and redox molecules in solution.[51] For example, we reported that Al_2O_3 films thicker than ~3.5 nm fully passivate electron transfer (eT) between underlying pyrolyzed polymer film (PPF) electrodes[55,56] and solution-phase ferrocenemethanol (FcMeOH).[51] Subsequently, Rose and coworkers reported that ALD-deposited Al_2O_3 films ~5 nm thick can electrochemically passivate an underlying Si(111) electrode.[52]

The other important precedents for our findings relate to NP-mediated eT across insulating layers. Although first reported by Natan and coworkers[29,57] and then more thoroughly studied by Schiffrin and coworkers,[58–60] the interest in NP-mediated eT across ultra-thin organic insulating layers picked up momentum in 2008 and 2009 when Fermin[30–32,61,62] and Gooding[33,63] independently reported that this type of eT is independent of insulating film thickness.[34] In these early publications, both groups used adsorbed AuNPs to switch on faradaic eT reactions following passivation of an electrode with self-assembled monolayers.[64] Over the past several years these results have been reproduced using different types of NPs (e.g., metals,[7,52,65–67] graphene,[68,69] nanotubes,[70,71] and quantum dots[32,72]) and electrodes (e.g., Au,[30–33] Pt,[60] carbon,[63] TiO_2,[65] and Si).[34]

The foregoing experimental observations raised questions about the underlying cause of this emergent phenomenon, and in 2010, Chazalviel and Allongue developed a theoretical model that described the principles of NP-mediated eT. They proposed that the potential across an electrode modified with an insulating layer decreases exponentially as a function of the insulating layer thickness.[35] Once NPs are deposited atop ultra-thin insulating layers, however, the applied potential develops primarily at the interface between the metal NPs and electrolyte.[32,35,52,65,73] As a result, distance-independent eT recovery is observed as long as the exchange current density across the insulating layer in the metal/insulator/metal NP system is much higher than the current density at a metal/insulating layer system.[31,32,35] This means that charging of NPs by a redox molecule, rather than eT between an electrode and NPs, is the rate limiting step in such processes.[35]

Our principle interest in this type of system is in understanding how reactions electrocatalyzed by metal NPs are affected by the presence of oxide surfaces. Due to the insulating nature of most oxides, there have only been a few reports of electrocatalysis on these types of surfaces. For example, Swider-Lyons and coworkers showed that PtNPs supported on metal oxides or metal phosphates lead to enhanced electrocatalytic activity for the ORR.[6,74] Although the mechanism of this reaction is unknown, the authors hypothesized that oxides can affect the electronic states of the Pt which in turn can lead to preferential adsorption of OH on the oxide (relative to the Pt surface).[6] Similarly, Ramaker and coworkers reported that if PtNPs are supported on tantalum oxide or tantalum oxyphosphate on Vulcan carbon, the presence of phosphates and oxides can lead to a higher proton concentration on PtNPs. This in turn results in improved electrocatalytic activity of Pt for the ORR.[75]

Interestingly, increased electroactivity can also be achieved by inverting metal/insulator/metal structures. For example, Adzic and coworkers reported that deposition of SnO_2 NPs onto polycrystalline Pt electrodes (SnO_2/pc-Pt) resulted in up to a 40-fold enhancement in current for the methanol oxidation reaction (MOR) compared to naked Pt electrodes.[76] Additionally, the MOR activity was found to be strongly dependent on the number of available SnO_2/Pt contact sites and to decrease as the size of the SnO_2 NPs increased. They interpreted these results in terms of a co-catalytic mechanism in which the reaction occurs at the contact line between Pt and the SnO_2 NPs. Moreover, the relationship between NP size and activity was thought to be a consequence of the formation of reduced Sn(II)O and the structural flexibility of the smaller SnO_2 NPs that resulted in correspondingly weaker binding of OH species.[76] The same group also observed that deposition of SnO_2 nanoislands onto Pt(111) resulted in enhanced

electrochemical activity for the ethanol oxidation reaction (EOR).[67] This is because of strong interactions between SnO_2 and H_2O, which lead to spontaneous cleavage of O-H bonds. The authors also reported that the EOR activity strongly depended on the surface SnO_2 concentration, thereby confirming the co-catalytic effect at the oxide-metal interface.

In the remainder of this chapter we will show that pinhole-free, electrochemically passivating Al_2O_3 films can be deposited onto PPF electrodes. When DENs containing an average of only 55 atoms each, are deposited onto ~15% of the Al_2O_3 surface, eT between the underlying PPF electrode and solution-phase ferrocenedimethanol ($Fc(MeOH)_2$) is recovered. This facilitated eT is insensitive to the thickness of the ALD oxide layers up to ~3.5 nm, but partial current recovery is still observed for films up to 5.7 nm thick. Even more interestingly, DENs containing an average of 55 Pt atoms confined to Al_2O_3 thin films ($PPF/Al_2O_3/G6\text{-}OH(Pt_{55})$), where G6-OH represents sixth-generation, hydroxyl-terminated poly(amidoamine) (PAMAM) dendrimers), are electrocatalytically active for the ORR. Finally, the $PPF/Al_2O_3/G6\text{-}OH(Pt_{55})$ constructs are robust, surviving up to at least 40 consecutive voltammetric scans and 10 min of sonication in 0.50 M H_2SO_4 without significant change in electrochemical activity.

EXPERIMENTAL

Activation of PPF Electrodes

Prior to ALD, PPFs were plasma activated using an Oxford Instruments Plasma Lab 80+ PECVD and Etching system. Individual PPFs were exposed to the plasma (O_2, 22% and N_2, 78%) for 30 s using the following conditions: flow rate, 50 sccm; pressure, 0.03 mmHg; power, 11 W; and temperature, 50 °C. After the plasma treatment, PPFs

were loaded into the ALD chamber within 10 min.

Surface Characterization

X-ray photoelectron spectroscopy (XPS) was carried out using a Kratos Axis Ultra spectrometer (Chestnut Ridge, NY) with an Al Kα source. Samples were grounded using Cu tape. XPS spectra were collected using a 0.10 eV step size and a band pass energy of 20 eV. An electron flood gun was used to neutralize charge on all samples. Binding energies were calibrated against the C 1s line of PPF (284.5 eV). CasaXPS (version 2.3.15, Casa Software, Teignmouth, UK) was used for peak fitting and analysis. A mixed Gaussian/Lorentzian model was used for symmetric line-shapes, while an asymmetric Lorentzian model was applied for asymmetric line-shapes.

Ellipsometric measurements were performed using a J. A. Woollam M-2000D spectroscopic ellipsometer (Lincoln, NE). Data were collected using five different angles (between 44° and 66°) for each measurement. A three-part model was used for data analysis. The first part was a 1.0 mm-thick layer of SiO_2 (optical constants provided by the manufacturer). The second slab was a 500 nm-thick layer of carbon (optical constants obtained experimentally using a plasma-activated PPF thin film). The third part was Al_2O_3 and the optical constants of this slab were provided by the manufacturer. Thickness of this layer was allowed to vary.

The surface roughnesses of the PPF and PPF/Al_2O_3 thin films were obtained using a Wyko NT9100 optical profilometer having a white light source and yielding 0.1 nm vertical resolution. The micro-Raman spectroscopy data were collected using a Witec Micro-Raman Alpha 300 spectrometer. Finally, SEM images were collected using an EI Quanta 650 microscope and using an accelerating voltage of 15 kV.

Electrochemical characterization

Electrochemical measurements were performed using CH Instruments model CHI700D Electrochemical Analyzer (Austin, TX). For all electrochemical experiments, a Hg/Hg_2SO_4 reference electrode (MSE, CH Instruments) and a Pt wire counter electrode were used. Electrochemical experiments were conducted in an electrochemical cell fabricated from Teflon with a Viton O-ring to define the area of the working electrode (12.4 mm^2). To avoid poisoning the working electrode with Hg while working with the Taflon electrochemical cell, the reference electrode was separated from the rest of the cell by a glass frit. Prior to the ORR experiments, the PtNPs were electrochemically cleaned by reversibly scanning the electrodes 10 times between −0.65 and 0.63 V (vs Hg/Hg_2SO_4) in N_2-purged 0.10 M $HClO_4$ solution. Electrochemical measurements were performed in aqueous solutions containing 1.0 mM $Fc(MeOH)_2$ and 0.10 M KNO_3 or 0.10 M $HClO_4$ purged with either N_2 or O_2.

Ag electrodeposition was performed in an aqueous solution containing 0.50 mM $AgNO_3$ and 0.10 M KNO_3. The potential was stepped sufficiently negative for 50.0 s to reduce Ag^+ (−0.25 V vs Hg/ Hg_2SO_4).

RESULTS AND DISCUSSION

Characterization of PPF Electrodes

The preparation and plasma-activation procedures used for the PPF electrodes were described in the Experimental Section, and therefore we focus here primarily on their characterization, properties, and use for electrochemical experiments.

After fabrication, the PPF electrodes were stored in the laboratory ambient for 15 days, which resulted in gradual surface oxidation, and then used for ALD within 24

h.[55,56,77] This step was included to enhance the number of active sites (C-O bonds) for Al_2O_3 nucleation. The number of C-O functionalities on the PPF surfaces was further increased by subjecting the substrates to a plasma (O_2:N_2 = 22:78) immediately prior to ALD. Through extensive optimization studies, we found that a high density of surface oxygen groups is critical to the formation of ultrathin, pinhole-free Al_2O_3 ALD layers.

XPS analysis was used to confirm oxygenation of the PPF electrode surfaces (Figure 3.1). The results show that immediately after fabrication the O 1s and C 1s peaks are present at 532 eV and 284.4 eV, respectively. After 15 days in the laboratory atmosphere, the amount of surface O increases ~1.7 times. Following 30 s of O_2/N_2 plasma treatment, the surface oxygen signal increases by another factor of two. The additional oxygenated functionalities are observed at 286.2 eV and 288.6 eV, and we assign these peaks to phenolic and carboxylic carbon, respectively.[78,79]

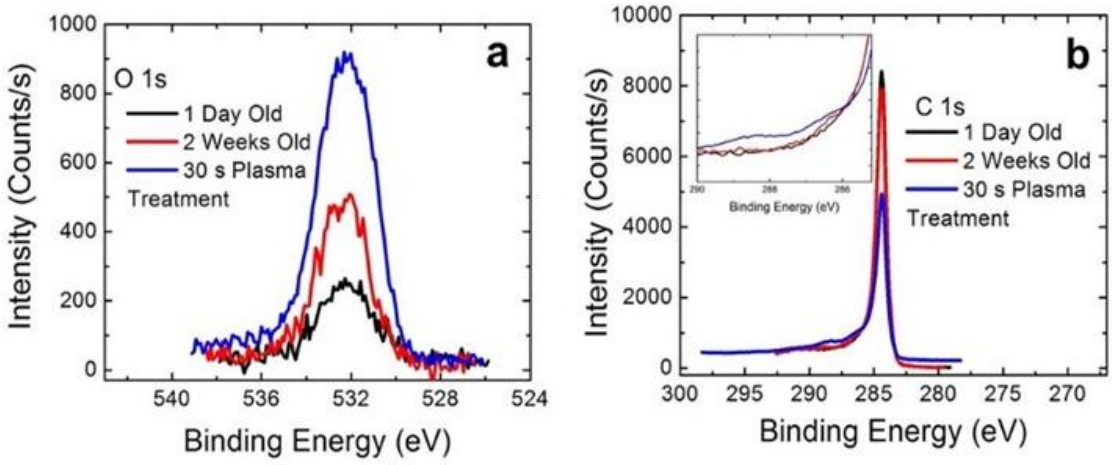

Figure 3.1 High-resolution XPS spectra of PPF electrodes in the (a) O 1s and (b) C 1s regions. The inset in (b) shows an expanded view of the C 1s shoulder.

The PPFs were also characterized using optical profilometry. At the lateral and vertical resolutions of the instrument (0.1 µm and 0.1 nm, respectively), the data reveal smooth, uniform surfaces that are free of cracks. The root-mean-square (rms) roughness, averaged over an area of 48 µm x 64 µm for eight different PPF electrodes was ~0.64 nm (Figure 3.2). This value is comparable to rms roughness values reported in the literature, which range from 0.2 and 0.7 nm, but these values were measured over much smaller areas (e.g., 0.5 µm x 0.5 µm).[80–82]

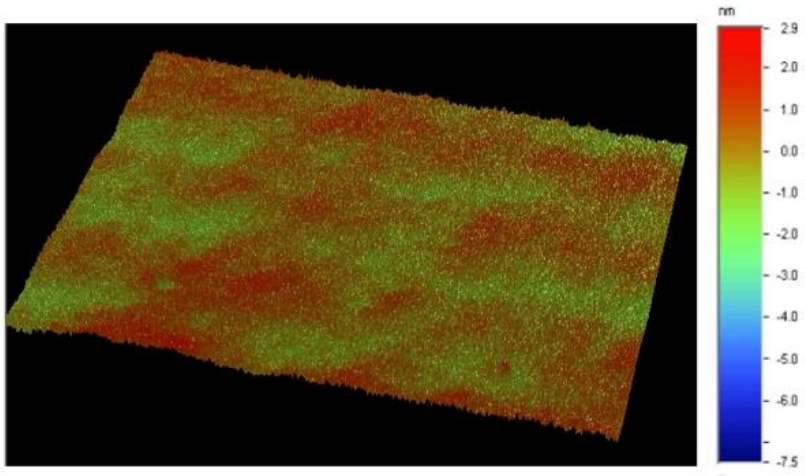

Figure 3.2: Topography of a plasma-activated PPF electrode obtained using optical profilometry.

Finally, micro-Raman spectroscopy was used to study the near-surface structure of the PPFs (Figure 3.3). The analysis revealed two Raman-active peaks.[82] A peak at 1600 cm^{-1} arises from the E_{2g} mode at the **Γ**-point commonly observed for glassy carbon and other sp^2 carbon systems.[83,84] The A_{1g} peak at ~1360 cm^{-1} is associated with loss of symmetry at the boundaries of graphite sheets.[82] Taken together, these results suggest that the PPF electrodes are uniform and structurally similar to glassy carbon.[84]

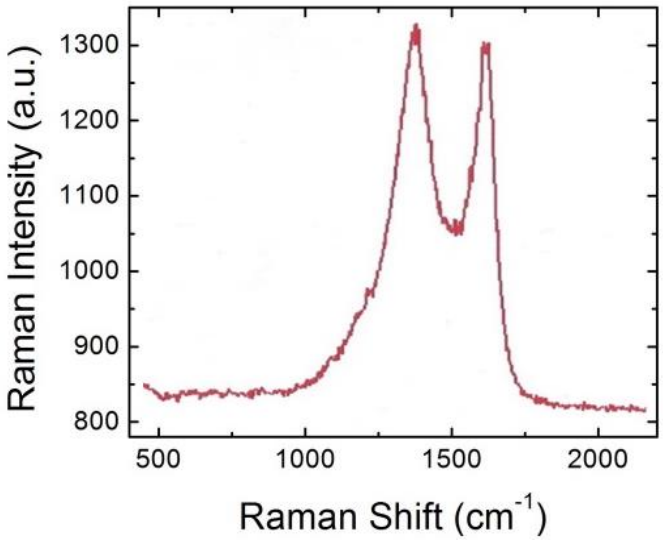

Figure 3.3: Micro-Raman spectrum of a PPF electrode fabricated using AZ 1518 photoresist.

Properties and Stability of Al_2O_3 ALD Films

The procedure used to prepare the Al_2O_3 ALD films is provided in the Experimental Section. For the purposes of our experiments, their critical characteristics are that they have well-defined thicknesses, that they be uniform over macroscopic dimensions, and that they be pinhole free.

The thicknesses of the Al_2O_3 films were measured using spectroscopic ellipsometry. The data revealed linear growth of the Al_2O_3 films with a growth rate of 0.086 ± 0.005 nm/cycle (Figure 3.4). This value is consistent with the growth rate provided by the ALD system manufacturer for the deposition of Al_2O_3 onto Si(100) at 150 °C (0.087 nm/cycle).[85]

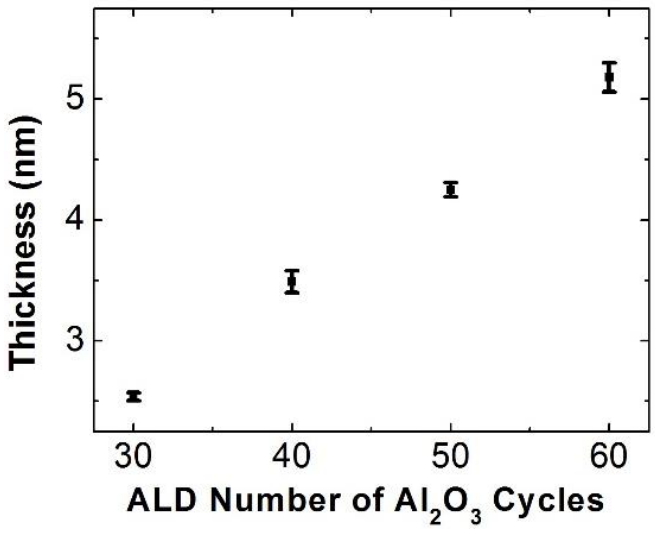

Figure 3.4 Ellipsometric measurements of the thicknesses of Al_2O_3 films as a function of the number of ALD cycles.

Optical profilometry revealed that the Al_2O_3 films are uniform and free of cracks. The value for the average rms roughness, determined using eight independently prepared PPF electrodes coated with 2.5 nm-thick Al_2O_3 films, was ~0.60 nm over an area of 48 µm x 64 µm (Figure 3.5). This value is almost the same as the corresponding rms value for the underlying PPF electrodes prior to ALD (~0.64 nm) discussed in the previous section.

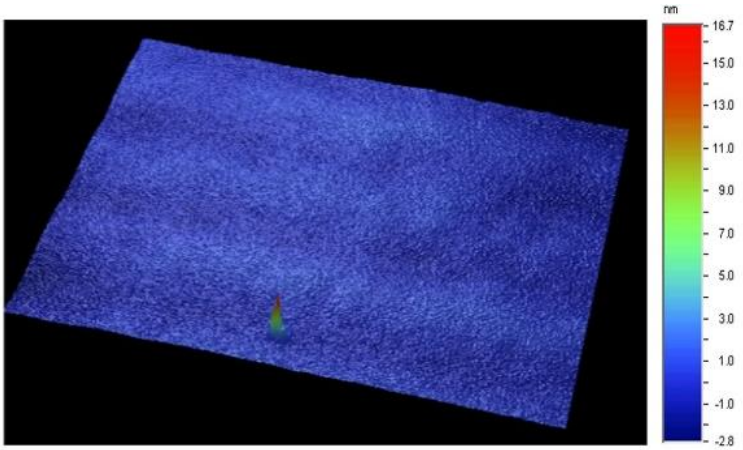

Figure 3.5: Optical profilometry of a plasma-activated (30 s) PPF electrode coated with Al_2O_3 using 30 ALD cycles.

Defects in the Al_2O_3 films were visualized by combining electrodeposition and SEM.[86] This analysis was carried out as follows. First, Al_2O_3-modified PPF electrodes were immersed in a solution containing 0.50 mM $AgNO_3$ and 0.10 M KNO_3, and then the potential was stepped to -0.25 V for 50 s.[51] Under these conditions, Ag electrodeposits into pinholes that might be present in the ALD film. Even subnanometer defects are revealed using this approach, because the presence of the pinhole, though smaller than the resolution of SEM, is magnified by the electrodeposited Ag islands. It is important to point out, however, that while this method is useful for approximating the number and location of defects in ALD films, it does not reflect their true size.[51]

Figure 3.6 shows the result of this experiment. Figure 3.6a is an SEM micrograph obtained after Ag electrodeposition onto a PPF electrode coated with 30 ALD cycles of Al_2O_3 (henceforth, PPF/Al_2O_3(30)), but without the 30 s plasma treatment prior to ALD. In contrast, when the exact same fabrication steps are used to prepare the Al_2O_3 film, except using a 30 s plasma pretreatment prior to ALD, pinhole-free films result over macroscopic lateral dimensions (e.g., 1.0 cm x 1.2 cm, Figure 1b). Clearly, the plasma-

induced oxygenation of the PPF surface is critical for the formation of ultrathin, pinhole-free electrodes.

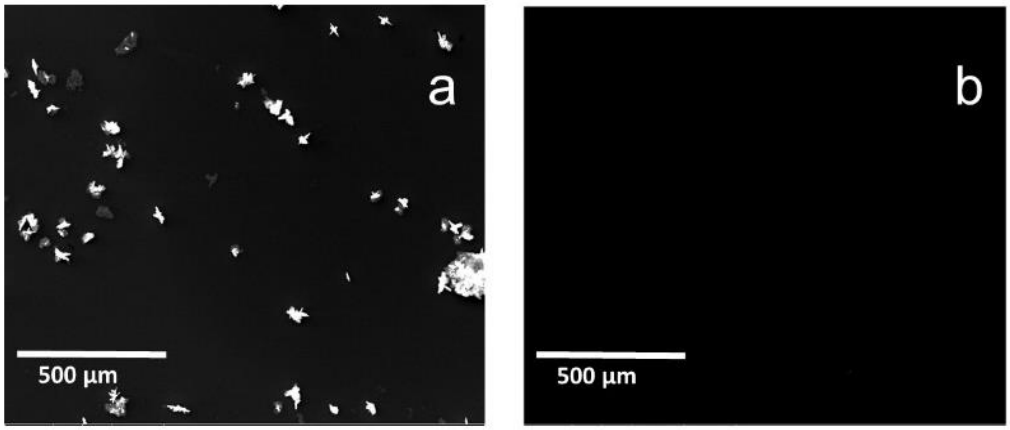

Figure 3.6: SEM micrographs of Ag electrodeposited onto PPF/Al_2O_3(30) electrodes (a) without and (b) with plasma reactivation of the carbon surface for 30 s. The Ag was electrodeposited by holding the potential at −0.25 V (vs an Hg/Hg_2SO_4 reference electrode) for 50 s in a solution containing 0.50 mM $AgNO_3$ and 0.10 M KNO_3.

The ALD films used in this study are stable in the electrochemical environment. For example, Figure 3.7a shows the first and fortieth cyclic voltammograms (CVs) obtained using a solution containing 1.0 mM $Fc(MeOH)_2$ plus 0.1 M KNO_3 and a PPF/Al_20_3(30) electrode. These data were recorded at neutral pH, but the stability of Al_2O_3 under acidic conditions is also crucial, because, as discussed later, immobilization of G6-OH(Pt_{55}) DENs is carried out at pH 3.0. To test the stability of the films in acid, a PPF/Al_20_3(30) electrode was immersed in a pH 3.0 $HClO_4$ solution for 30 min. Figure 3.7b shows CVs of $Fc(MeOH)_2$ before and after this acid treatment. Clearly changes to the ALD film are minimal under the conditions required for Pt DEN immobilization.

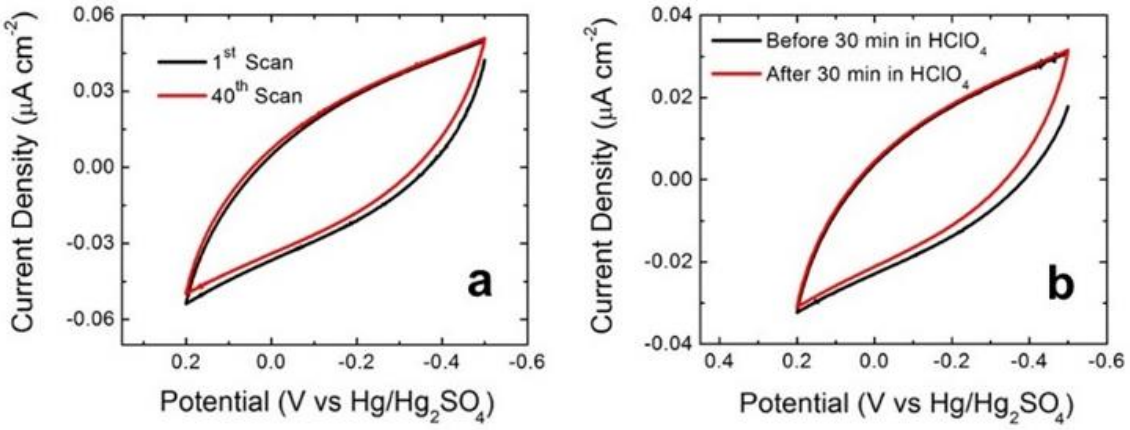

Figure 3.7: (a) First (black) and 40th (red) CVs for a PPF/Al_2O_3(30) electrode. (b) CVs for a PPF/Al_2O_3(30) electrode before (black) and after (red) a 30 min exposure of the electrode to a pH 3.0 $HClO_4$ solution. The CVs were obtained in an aqueous solutions containing 1.0 mM $Fc(MeOH)_2$ and 0.10 M KNO_3. The scan rate was 10 mVs^{-1}.

Immobilization and Characterization of Pt DENs atop Al_2O_3-Modified PPF Electrodes

Prior to immobilization atop Al_2O_3-modified PPF electrodes, the free G6-OH(Pt_{55}) DENs were characterized using UV-vis spectroscopy and STEM (Figures 3.8 and 3.9, respectively). Focusing on the UV-vis spectroscopy first, formation of the G6-OH(Cu^{2+})$_{55}$ precursor is confirmed by the presence of a well-defined ligand-to-metal charge transfer (LMCT) band at λ_{max} = 300 nm (top). The disappearance of this band following the addition of BH_4^- confirms the formation of G6-OH(Cu_{55}) DENs. After the addition of $PtCl_4^{2-}$ to the G6-OH(Cu_{55}) solution at pH 3.0, the LMCT band is still absent, because interior tertiary amines of the dendrimer are protonated and unable to interact with Cu^{2+} (bottom).[87] Galvanic exchange is confirmed by changing the pH of the solution to 7.5. In this case, the LMCT band reappears because the pH of the DEN solution is sufficiently high for the interior tertiary amines of the dendrimer to complex with Cu^{2+}.

Furthermore, the STEM results are fully consistent with prior reports,[13,15] and they indicate the presence of Pt_{55} DENs having a size of 1.3 ± 0.2 nm (Figure 3.9).

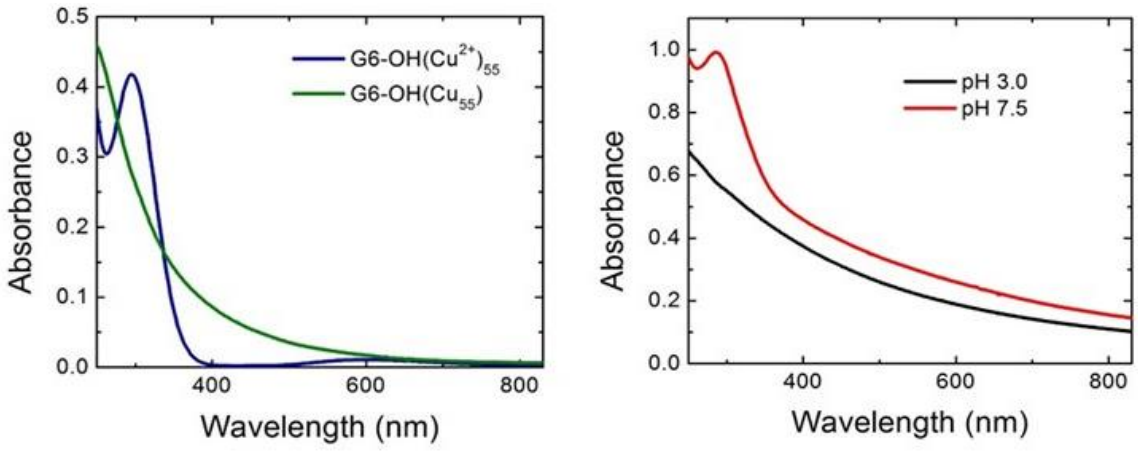

Figure 3.8: Absorption spectra of freshly prepared G6-OH(Cu^{2+})$_{55}$ and G6-OH(Cu_{55}) DEN solutions (top spectra), and G6-OH(Pt_{55}) DEN solutions at pH 3.0 and 7.5 (bottom spectra). A 1.0 mm cuvette was used to obtain measurements. All solutions were 10 µM in G6-OH and a 10.0 µM G6-OH solution was used for reference.

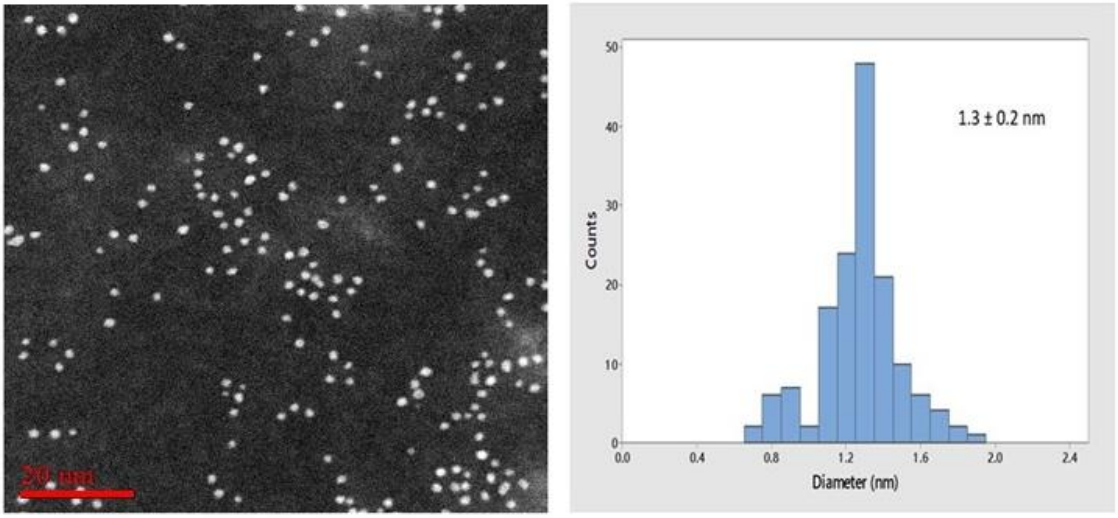

Figure 3.9: STEM micrograph and particle-size distribution histogram for G6-OH(Pt_{55}) DENs. The particle-size distribution is based on 150 randomly selected particles.

The procedure for preparing the PPF/Al_2O_3/G6-OH(Pt_{55}) layered structure was discussed in the Experimental Section. To confirm the presence of both the dendrimers and Pt on the Al_2O_3 surface, we carried out XPS measurements (Figure 3.10a). The N(1s) peak at 400.4 eV confirms the presence of the PAMAM dendrimers, while the Pt($4d_{3/2}$), Pt($4d_{5/2}$), Pt(4f) and Pt(4p) peaks at 332.1 eV, 315.4 eV, ~72.2 eV and 519.4 eV, respectively, confirm the presence of Pt. The location of the Pt(4f) peak at a little higher binding energy than that of bulk Pt (71.1 eV)[88] is consistent with previously reported XPS measurements for Pt DENs and is likely a consequence of their small size and the presence of the dendrimers.[13] The Al (2p) peak is also observed, indicating that Al_2O_3 is still present on the surface after immobilization of the Pt DENs.

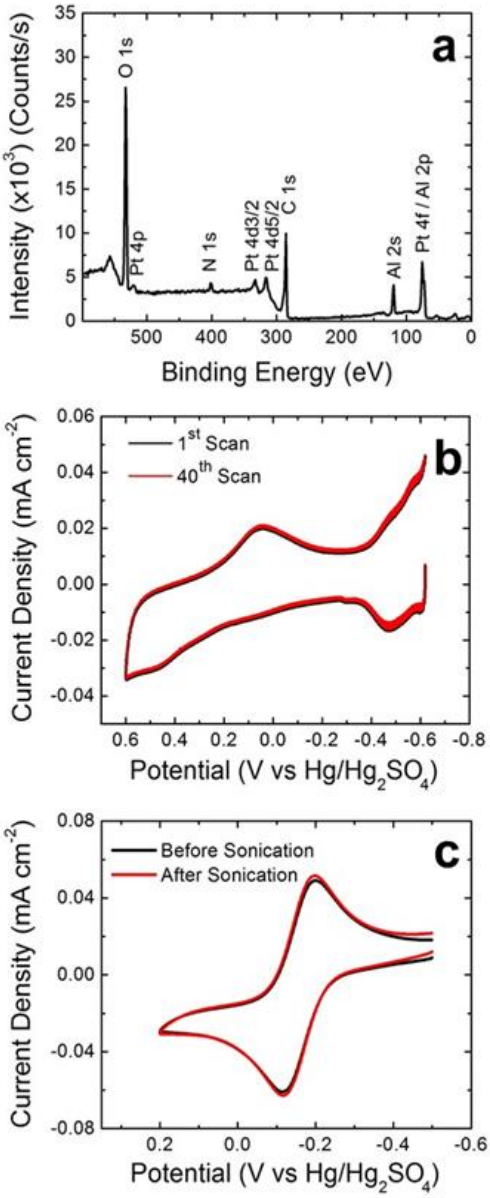

Figure 3.10 (a) XPS spectrum of a PPF/Al_2O_3(30)/G6-OH(Pt_{55}) electrode. (b) CVs of the first (black) and fortieth (red) scans of a PPF/Al_2O_3(30)/G6-OH(Pt_{55}) electrode in an Ar-purged aqueous 0.10 M $HClO_4$ solution. The scan started at −0.62 V and proceeded initially in the positive direction. The scan rate was 100 mV/s. (c) CVs of a PPF/Al_2O_3(30)/G6-OH(Pt_{55}) electrode before (black) and after (red) sonication in an aqueous 0.50 M H_2SO_4 solution for 10 min. These CVs were obtained in an aqueous solutions containing 1.0 mM $Fc(MeOH)_2$ and 0.10 M KNO_3. The scan rate was 10 mVs^{-1}.

The presence of Pt on the electrode surface was also confirmed electrochemically by obtaining CVs of a PPF/Al_2O_3(30)/G6-OH(Pt_{55}) electrode in a 0.1 M aqueous $HClO_4$ solution. Figure 3.10b shows both the first and the fortieth CVs. The nearly identical appearance of these two scans demonstrates the stability of the DENs on the Al_2O_3 surface. In both scans, the Pt oxidation region is observed starting at ~0.2 V, and the corresponding oxide reduction peak is at ~0.07 V. The characteristic hydride peaks at potentials <-0.4 V are also present. All of these characteristics are consistent with previous reports for G6-OH(Pt_{55}) DENs immobilized directly on carbon electrodes.[13,19,89,90] Integration of the hydride oxidation peaks, coupled with a calculation we have used previously to determine DEN coverage,[91,92] indicate that ~15% of the Al_2O_3 surface is covered by DENs.

To further demonstrate the structural stability of PPF/Al_2O_3(30)/G6-OH(Pt_{55}) electrodes, CVs of $Fc(MeOH)_2$ were obtained before and after sonication in 0.50 M H_2SO_4 for 10 min. The results (Figure 3.10c) indicate very little change arising from this accelerated form of stability testing. On the basis of the data shown in Figure 3.10, we conclude that the interaction between the dendrimer host and the Al_2O_3 surface is quite robust.

Pt DEN-Mediated eT

Through extensive testing, we found that Al_2O_3 films thicker than 2.5 nm (30 ALD cycles) are necessary to completely passivate eT between the underlying PPF electrode and solution-phase $Fc(MeOH)_2$. For example, Figure 3.11a compares the CV response of a bare PPF electrode and a PPF/Al_2O_3(30) electrode. The inset in Figure 3.11, which shows the potential region around E^o for $Fc(MeOH)_2$, clearly indicates complete

electrode passivation. These results can be compared to the CVs shown in Figure 3.11b, which compare a PPF/Al_2O_3(30)/G6-OH(Pt_{55}) electrode with that of a PPF/Al_2O_3(30)/G6-OH (no Pt_{55} DENs) electrode. The obvious result is that electroactivity is completely reactivated in the presence of Pt DENs. Indeed, the shape of two black CVs in Figure 3.11 are nearly identical. These results demonstrate that the observed current recovery of $Fc(MeOH)_2$ is facilitated solely by the Pt DENs and that it is not influenced by the PAMAM dendrimer host, the electrolyte solution, or electrochemical cycling.

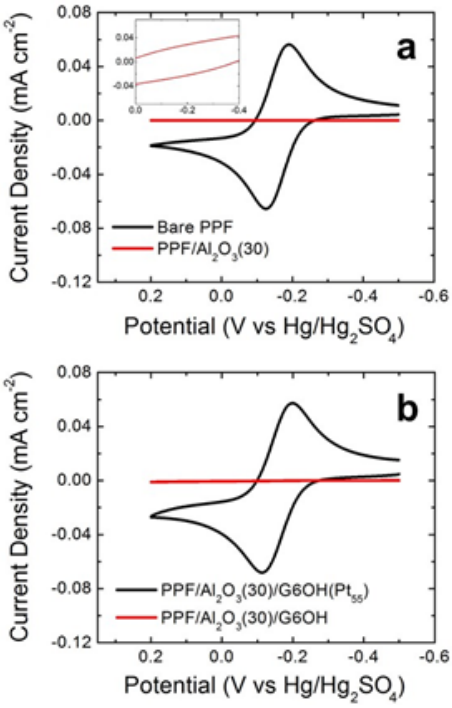

Figure 3.11 (a) CVs obtained at a bare PPF electrode (black) and a PPF/Al_2O_3(30) electrode (red). The inset is an expanded view of the potential region around E° for $Fc(MeOH)_2$. (b) CVs obtained at a PPF/Al_2O_3(30)/G6-OH electrode (red) and a PPF/Al_2O_3(30)/G6-OH(Pt_{55}) electrode (black). The solutions contained aqueous 1.0 mM $Fc(MeOH)_2$ and 0.10 M KNO_3. The scan rate was 10 mVs^{-1}.

Location of Pt DENs

We have previously shown that Pt DENs prepared by galvanic exchange are confined within their dendrimer hosts.[15,90] It is important, however, to demonstrate that they remain confined following immobilization onto the Al_2O_3 surfaces used in this study. In other words, that the presence of Al_2O_3 does not somehow extract the Pt DENs. This point was addressed by performing a Pt DENs poisoning experiment that we have reported previously.[90]

The poisoning experiment was carried out as follows. First, a PPF/Al_2O_3(30)/G6-OH(Pt_{55}) electrode was immersed in ethanol. Second, sufficient 1-decanethiol was added to make the solution 3.0 mM in ethanol. Third, after 20 min, the electrode was rinsed in ethanol and NERL reagent-grade water. Finally, a CV was obtained in an aqueous solution containing 1.0 mM $Fc(MeOH)_2$ and 0.1 M KNO_3. The resulting low current (red CV in Figure 3.12) indicates that the Pt DENs are nearly fully passivated by surface-confined 1-decanethiol. In contrast, when the same experiment is carried out using a CH_2Cl_2 in place of ethanol the black CV obtains.

We interpret these results as follows. Ethanol is a good solvent for PAMAM dendrimers, and therefore their branches are solvated allowing 1-decanethiol to pass to the surface of the encapsulated Pt DENs. This in turn passivates the surface of the DENs with 1-decanethiol and so little faradaic current due to $Fc(MeOH)_2$ is observed. In contrast, CH_2Cl_2 is a very poor solvent for PAMAM dendrimers, and therefore their branches collapse onto the surface of the Pt DENs rendering them inaccessible to the thiol and hence not poisoned. Accordingly, when the electrode is rinsed and placed back in the electrolyte solution, the original (unhindered) voltammetry is observed (black CV in Figure 3.12). If the DENs were not confined within the dendrimers, both CVs (not just

the red one) in Figure 3.12 would exhibit little current. Accordingly, these results confirm that the Pt DENs are present within the dendrimers and that current recovery on the Al_2O_3 surface is mediated by PtNPs encapsulated within the dendrimers and not by bare PtNPs.

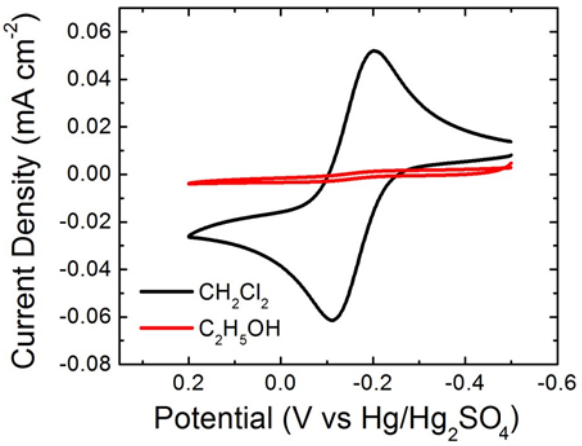

Figure 3.12: CVs obtained after exposure of PPF/Al_2O_3(30)/G6-OH(Pt_{55}) electrodes to 1-decanethiol in either CH_2Cl_2 (black) or ethanol (red) for 20 min. The aqueous electrolyte solution contained 1.0 mM $Fc(MeOH)_2$ and 0.10 M KNO_3. The scan rate was 10 mVs^{-1}.

Effect of Al_2O_3 Thickness on Pt DEN-Mediated eT

Figure 3.13a presents CVs obtained using PPF/Al_2O_3(*n*)/G6-OH(Pt_{55}) electrodes, where *n* represents the number of ALD cycles used to prepare the Al_2O_3 layer. As discussed in the context of Figure 3.13, the CV of $Fc(MeOH)_2$ corresponding to the PPF/Al_2O_3(30)/G6-OH(Pt_{55}) electrode is nearly identical to that obtained using a bare PPF electrode. As the number of ALD cycles increase from 30 to 65, however, the faradaic current decreases slowly at first and proceeds to full passivation at $n = 65$.

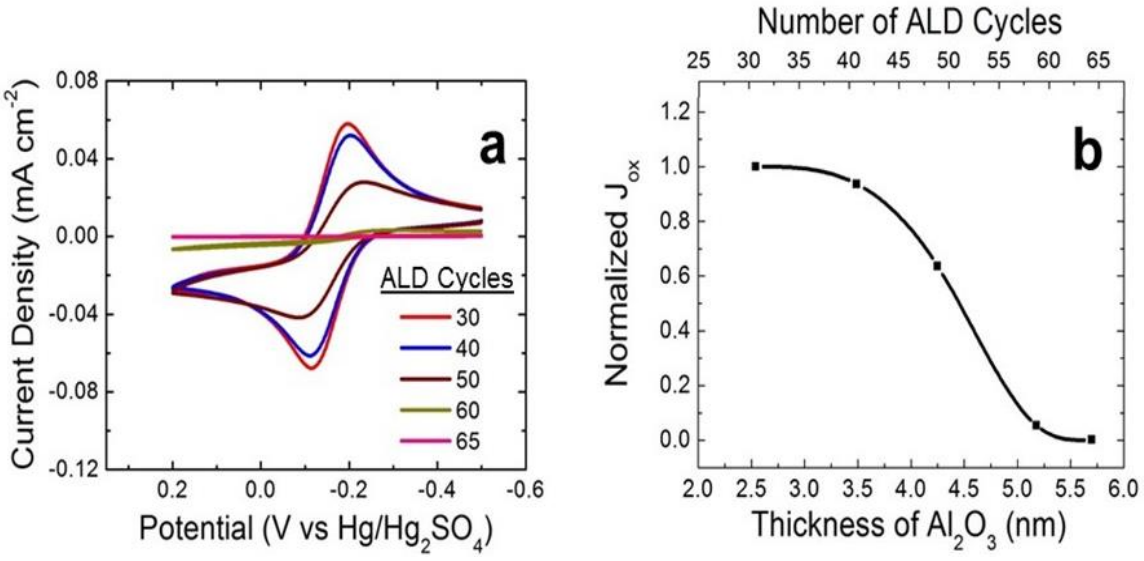

Figure 3.13: (a) CVs of PPF/Al_2O_3(n)/G6-OH(Pt_{55}) electrodes (n is the number of ALD cycles, as indicated in the legend). The aqueous electrolyte solution contained 1.0 mM $Fc(MeOH)_2$ and 0.10 M KNO_3. The scan rate was 10 mVs^{-1}. (b) Normalized maximum current density (J_{ox}), obtained from the CVs in (a), as a function of the number of ALD cycles and the thickness of the Al_2O_3 ALD layers on the PPF electrodes. The value of J_{ox} for a bare PPF electrode was used to normalize the currents.

The plot shown in Figure 3.13b is a quantitative representation of the normalized current density (J_{ox}), obtained from the peaks of the $Fc(MeOH)_2$ oxidation waves shown in Figure 3.13a, as a function of the Al_2O_3 thickness and number of ALD cycles. This plot, along with the observation of an increase in splitting between the oxidation and reduction waves as *n* increases, suggests that a small but detectable decrease in eT rate occurs for an Al_2O_3 thickness of 3.5 nm (40 ALD cycles). Much larger decreases are observed for thicknesses ≥4.3 nm (≥50 ALD cycles). In other words, for thicknesses of Al_2O_3 <3.5 nm, eT between $Fc(MeOH)_2$ and the G6-OH(Pt_{55}) DENs is the rate limiting step.[34,35,63] For thicknesses >3.5 nm the eT kinetics change from thickness independent to

thickness dependent, suggesting that eT from the PPF electrode to G6-OH(Pt_{55}) DENs becomes the limiting source of charge transfer.

As discussed in the introduction, Chazalviel and Allongue reported a theoretical framework for understanding the distance dependence of eT across metal/insulator/metal-NP systems.[35] This model suggests that 55-atom DENs, which are have a diameter of ~1.3 nm, should exhibit distance independent eT up to insulator thicknesses of ~1.6 nm. The distance we observe for this transition is ~3.5 nm. At present we do not understand the origin of this discrepancy.

It is possible to extract the effective standard heterogeneous eT rate constant from the brown-colored CV shown in Figure 3.13a, which corresponds to the PPF/Al_2O_3(50)/G6-OH(Pt_{55}) construct, using the Nicholson and Shain model[24] and a value for the diffusion coefficient of oxidized ferrocenedimethanol of 6.7 x 10^{-6} cm^2/s.[93,94] The Al_2O_3 layer in this film is 4.3 nm thick, and we estimate standard eT rate constant to be 1.43 x 10^{-3} cm/s. This value is just a little higher than previously reported values for NP-reactivated eT across organic layers having thicknesses close to 4.3 nm.[32,33,63,95,96]

The ORR at a Reactivated Al_2O_3 Thin Film Electrode

Our long-term interest is in developing a better understanding of electrocatalytic reactions in which an oxide surface participates. As a first step toward that goal, we examined the voltammetry of three different types of electrodes in a 0.10 M $HClO_4$ solution saturated with O_2 (Figure 3.14).

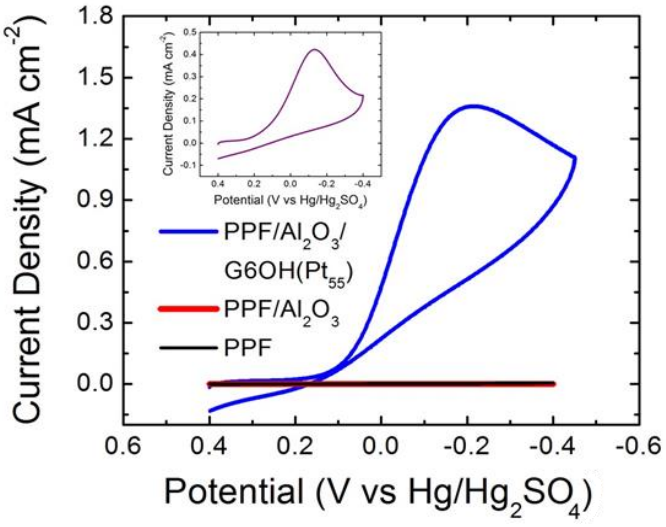

Figure 3.14: CVs obtained in an aqueous O_2-saturated 0.10 M $HClO_4$ solution at a bare PPF electrode (black), a PPF/Al_2O_3(30) electrode (red), and a PPF/Al_2O_3(30)/G6-OH(Pt_{55}) electrode (blue). For comparison, the inset is a CV obtained at a macroscopic Pt electrode. The scan rate was 50 mV/s in all cases.

Over the potential range examined (± 0.40 V), the bare PPF electrode is catalytically inactive for the ORR. Likewise, a PPF/Al_2O_3(30) electrode is also inactive. In contrast, the PPF/Al_2O_3(30)/G6-OH(Pt_{55}) is highly active. In fact, although the peak current density of PPF/Al_2O_3(30)/G6-OH(Pt_{55}) electrode is higher compared to a bulk Pt electrode, their onset potentials are nearly the same (Figure 3.14, inset). A control experiment was also carried out in which a PPF/Al_2O_3(30)/G6-OH(Pt_{55}) electrode was scanned in an O_2-free 0.10 M $HClO_4$ solution. The result displayed only a small background current (Figure 3.15), confirming that the peak shown in Figure 3.14 corresponds to the ORR.

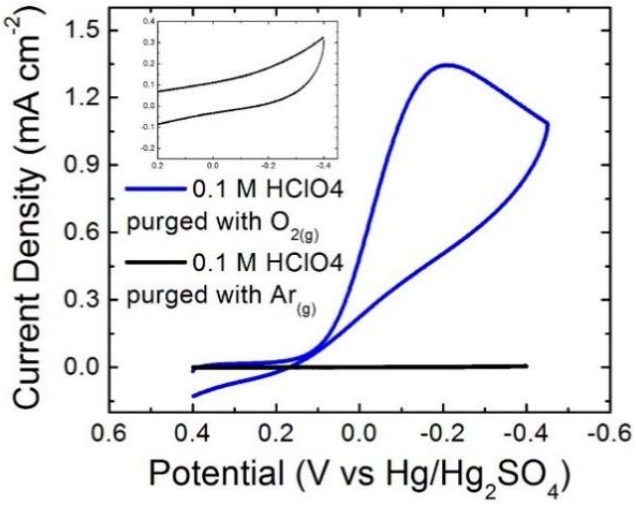

Figure 3.15: CVs obtained at PPF/Al_2O_3(30)/G6-OH(Pt_{55}) electrode in aqueous solutions saturated with either O_2 (blue) or Ar (black). The aqueous solution contained 0.10 M $HClO_4$, and the scan rate was 50 mV/s. The geometric areas of the electrodes were 12.4 mm^2.

SUMMARY AND CONCLUSIONS

Here we have shown that eT between a PPF electrode and $Fc(MeOH)_2$ can be completely passivated by Al_2O_3 films as thin as 2.5 nm if the PPF electrode is plasma-activated before ALD. One of the key findings is that deposition of 1.3 nm G6-OH(Pt_{55}) DENs atop these insulating films leads to complete recovery of faradaic eT. Most importantly, however, the PPF/Al_2O_3/G6-OH(Pt_{55}) electrodes are stable and active for electrocatalytic reactions, in this case the ORR.

The PPF/Al_2O_3/G6-OH(Pt_{55}) system is unique, because it permits the study of electrocatalytic reactions in the presence and absence of NP/support interactions. That is, the DENs in this model system are not in a direct contact with the Al_2O_3 support. Therefore, support effects do not manifest themselves when DENs are used for studying

electrocatalytic reactions. If, however, the dendrimers can be cleanly removed without passivating or aggregating the encapsulated PtNPs, then it will be possible to directly examine the effect of the PtNP/oxide-support interaction on electrocatalytic reactions. Ongoing studies suggest that it is indeed possible to remove the dendrimer, and the results of these experiments, as well as the outcome of more complex electrocatalytic reactions, will be reported in due course.

Chapter 4: Electrocatalytic Reduction of Oxygen on Platinum Nanoparticles in the Presence and Absence of Interactions with the Electrode Surface[2]

INTRODUCTION

In this chapter, we report a method for cleanly removing dendrimers from surface-confined dendrimer-encapsulated Pt nanoparticles (Pt DENs)[11,17,19,43,44,46,97–99] without measurably changing their size or shape (Illustration 4.1). The results of this study are important for two reasons. First, they lead to a general means for preparing highly monodisperse, stabilizer-free mono- and bimetallic nanoparticles (NP) in the 0.5-3.0 nm size range. Second, and more specifically, we are now in a position to begin answering fundamental questions about how the presence of a dendrimer affects the catalytic properties of DENs.[100] Accordingly, we begin this set of studies by discussing how the dendrimer affects the oxygen reduction reaction (ORR) electrocatalyzed by PtNPs in the presence and absence of dendrimers.

[2] Ostojic, N.; Crooks, R. M. Electrocatalytic Reduction of Oxygen on Platinum Nanoparticles in the Presence and Absence of Interactions with the Electrode Surface. *Langmuir* **2016**, *32*, 9727–9735.
I was the primary author on this publication working under the supervision of Dr. R. M. Crooks.

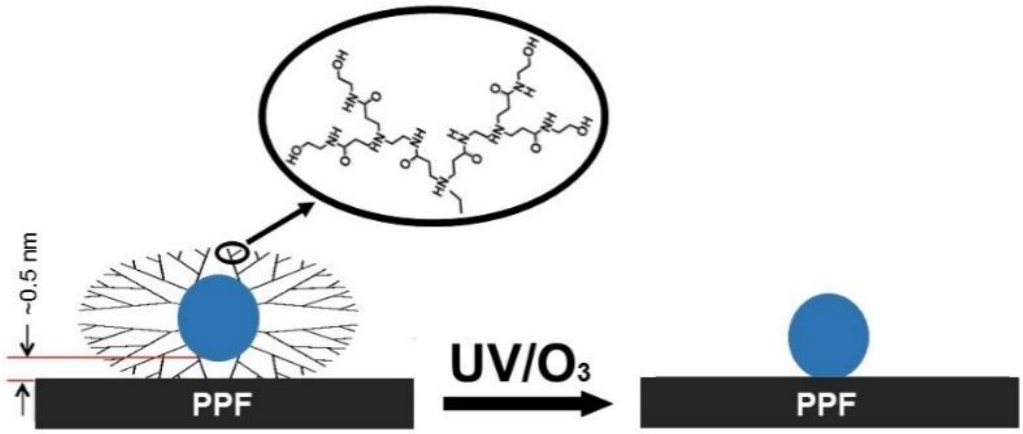

Illustration 4.1: Schematic representation of G6-OH dendrimer removal from G6-OH(Pt_{55}) immobilized atop a PPF/Al_2O_3 electrode.

First synthesized by Vogtle and coworkers in 1978,[101] dendrimers are branched, spherical macromolecules widely used to encapsulate objects ranging from NPs to drugs.[10,102–105] Poly(amidoamine) (PAMAM) dendrimers are a dendrimer subclass that consists of an alkyl-diamine core, amidoamine branches, and a vast range of peripheral functionalities (Scheme 1).[10] The size of PAMAM dendrimers depends on the number of reaction cycles carried out during the synthesis.[10] For example, seven iterations of Michael addition followed by amidation yields a sixth-generation (G6) dendrimer having a calculated diameter of ~6.7 nm.[12,106] DENs are usually prepared in PAMAM dendrimers in two steps. First, the dendrimers are mixed with metal ions, which partition into the dendrimer interior. The stoichiometric ratio between the dendrimer and the metal ions determines the final size of the encapsulated NP. Second, a strong reducing agent, such as BH_4^-, is added to the solution. This results in reduction of the ions and subsequent intradendrimer agglomeration of the resulting metal atoms.[11,15]

DENs usually have diameters between ~0.5-2.2 nm,[19] but they can be smaller[107,108] or larger. In addition to acting as templates, dendrimers are also stabilizers

that prevent aggregation of DENs in solution. Unlike most stabilizers, however, dendrimers do not passivate the surface of their encapsulated NPs. This means that DENs are good models for studying homogeneous and heterogeneous catalytic reactions in a broad range of solvents.[109–111] However, in the absence of a good solvent, like water or methanol, or in the gas phase, dendrimers collapse around the NPs rendering them inactive.[19,90,112–116] Under these conditions, therefore, the presence of the dendrimer renders the templated NPs catalytically inactive. Another consequence of the presence of the dendrimer is that immobilized DENs are not in direct contact with the support material (Scheme 1a), for example an electrode. For fundamental NP catalysis studies in which experimental results are compared to first-principles calculations this is good, because it removes the complexity of NP-support interactions from the theoretical description of the system.[8,9,46,87,98,117–120] Now, however, we are ready to begin including this additional level of complexity into our research, and therefore it has become necessary to find a way to remove the dendrimers from the DENs so that the metal is in direct contact with the substrate (Scheme 4.1b).

As will be discussed in more detail later, we have found that UV/O_3 is effective for cleanly eliminating dendrimers from DENs. Before settling on UV/O_3, we also considered plasmas and heat treatments. Previous studies suggested, however, that these methods generally lead to irreversible changes in NP size, shape, and distribution.[44,121–123] In contrast, UV/O_3 has previously been used to decompose solution-phase dendrimers and other organic capping agents with and without encapsulated NPs.[121,124,125] For example, Rosal and coworkers recently reported that G3 amine-terminated PAMAM dendrimers are completely decomposed by O_3 within 1 min.[124] The authors explained that decomposition arises from oxidation of dendritic amines, which

results in highly oxidized fragments. Similarly, Somorjai and coworkers studied the decomposition of G4 hydroxyl-terminated PAMAM dendrimers (G4-OH) with and without encapsulated Pt and Rh NPs. This study showed that after 6 h of the UV/O_3 exposure, ~60% of the overall dendrimer structure was destroyed.[125] The same group also used the UV/O_3 technique for removal of poly(vinylpyrrolidone) and tetradecyl tributylammonium bromide capping agents from PtNPs.[121] In this study, the TEM data indicated that after 2 h of the UV/O_3 treatment the PtNPs retained their original size and shape.

As mentioned earlier, we are interested in studying how supports cooperate with metal nanoparticles to catalyze electrochemical reactions like the ORR. There have been a few key studies in this regard that predate our own interest. For example, it has been shown that direct interactions between metal NPs and metal-oxide or metal-phosphate supports enhance electrocatalytic activity for the ORR.[6,7,74,75,126] Specifically, Alonso-Vante and co-workers showed that PtNPs supported on a titanium dioxide (TiO_2)-modified carbon support ($C/TiO_2/Pt$) exhibit higher electrocatalytic activity for the ORR compared to the same PtNPs deposited directly onto a carbon support (C/Pt).[126] The XPS analysis of the two electrocatalysts revealed that the effect of TiO_2 on PtNPs is the result of a superposition of charge transfer and lattice strain. Adzic and co-workers demonstrated that Pt supported on a NbO_2-modified C support ($C/NbO_2/Pt$) experiences suppressed oxidation compared to Pt supported on carbon support (C/Pt) due to lateral repulsion between PtOH and oxide species from NbO_2.[7] They showed that this in turn results in three times higher Pt mass activity for the ORR compared to the commercial C/Pt electrocalayst. The Adzic group has also studied metal NP/support interactions for

electrooxidation of alcohols, and these reactions are also accelerated by the presence of appropriate supports.[67,76,127–129]

In the remainder of this chapter we will show that UV/O_3 treatment can be used to remove G6-OH immobilized on pyrolyzed photoresist film (PPF) supports (electrodes) in the presence of DENs. Importantly, the original size and shape of Pt DENs are conserved after dendrimer removal. The UV/O_3 treatment oxidizes ~10% of the surface of encapsulated PtNPs, but it is possible to remove this oxide electrochemically. More interestingly, we find that the Pt DEN-modified PPF electrodes are slightly more active for the ORR in the absence of the dendrimer.

EXPERIMENTAL SECTION

UV/O_3 Treatment

Individual PPF/G6-OH(Pt_{55}) electrodes were placed in the middle of the UV/O_3 chamber (PSD-UV4 withOES1000D, Novascan Technologies, Ames, IA) and treated for 2.25 h using the following protocol, which we found to be critical for maximum dendrimer decomposition and minimal PtNP surface oxidation. First, the vacuum was turned on and an external supply of O_2 was introduced into the chamber at 517.1 mmHg for 10 min. Second, the O_2 flow was stopped and the UV lamp was turned on for 5 min. After turning off the UV lamp, the chamber was purged with O_2 for 3 min. This step was repeated two additional times. Third, the O_2 flow was stopped and the UV lamp was turned on for 15 min. The UV lamp was then turned off, and the chamber was purged with O_2 for 2 min. Fourth, the O_2 flow was stopped and the UV lamp was turned on for 30 min. After 30 min, the UV lamp was turned off and the chamber was purged with O_2 for 2 min. This step was repeated twice, and then the O_2 flow was stopped and the UV

lamp was turned on for an additional 45 min. At this point the substrate was removed from the UV/O_3 chamber and used within 30 min.

X-ray Photoelectron Spectroscopy (XPS)

XPS samples were prepared by immobilizing Pt DENs atop PPF electrodes as previously described in Chapter 2. XPS was carried out using a Kratos Axis Ultra spectrometer (Chestnut Ridge, NY) having an Al Kα source. Samples were grounded using metal holders. Careful placement of the PPF/G6-OH(Pt_{55}) electrode made it possible to characterize the same location before and after UV/O_3 treatment. This was necessary because the G6-OH(Pt_{55}) sample did not dry uniformly after dropping onto the PPF support. XPS spectra were collected using a 0.10 eV step size and a bandpass energy of 20 eV. An electron flood gun was used to neutralize charge on the samples. Binding energies were calibrated against the C 1s line of PPF (285.0 eV).[88] CasaXPS (version 2.3.15, Casa Software, Teignmouth, UK) was used for peak fitting and analysis. A mixed Gaussian/Lorentzian model was used for symmetric line-shapes, while an asymmetric Lorentzian model was applied for asymmetric line shapes.

RESULTS AND DISCUSSION

Effect of UV/O_3 on PPF Substrates

The UV source used for the UV/O_3 treatment emits at 184.9 nm and 253.7 nm.[121] Oxygen absorbs at 184.9 nm to yield O_3. Subsequently, O_3 absorbs at 253.7 nm and decomposes to form atomic oxygen.[130] Atomic oxygen is a strong oxidant, which reacts with organics to yield volatile substances including CO_2, N_2, and H_2O.[121,130,131]

In the present study, we used XPS extensively to study the effect of UV/O_3 on

dendrimer decomposition. Reliable conclusions, however, require careful control experiments so this investigation began with a study of the effects of UV/O_3 on naked PPF electrodes. The fabrication of the PPF electrodes and the protocol for UV/O_3 treatment are provided in the Experimental Section, but it amounts to a 2.25 h exposure.

Prior to UV/O_3 (Figure 4.1a), the C 1s region of the XPS spectrum of a naked PPF electrode consists of a single peak at 285.0 eV. This corresponds to the C-C bonds of the PPF substrate.[51,112] Following UV/O_3 exposure, however, the intensity of this peak decreases and two new oxidation products, corresponding to phenolic and carboxylic carbon,[51,112,132] are observed at 287.0 and 289.2 eV, respectively (Figure 4.1b). High-resolution analysis of the O 1s region confirms oxidation of the PPF surface, with the intensity of the surface oxygen peak increasing by a factor of 3 (Figure 4.2). No nitrogen was observed on the PPF surface before or after UV/O_3 exposure.

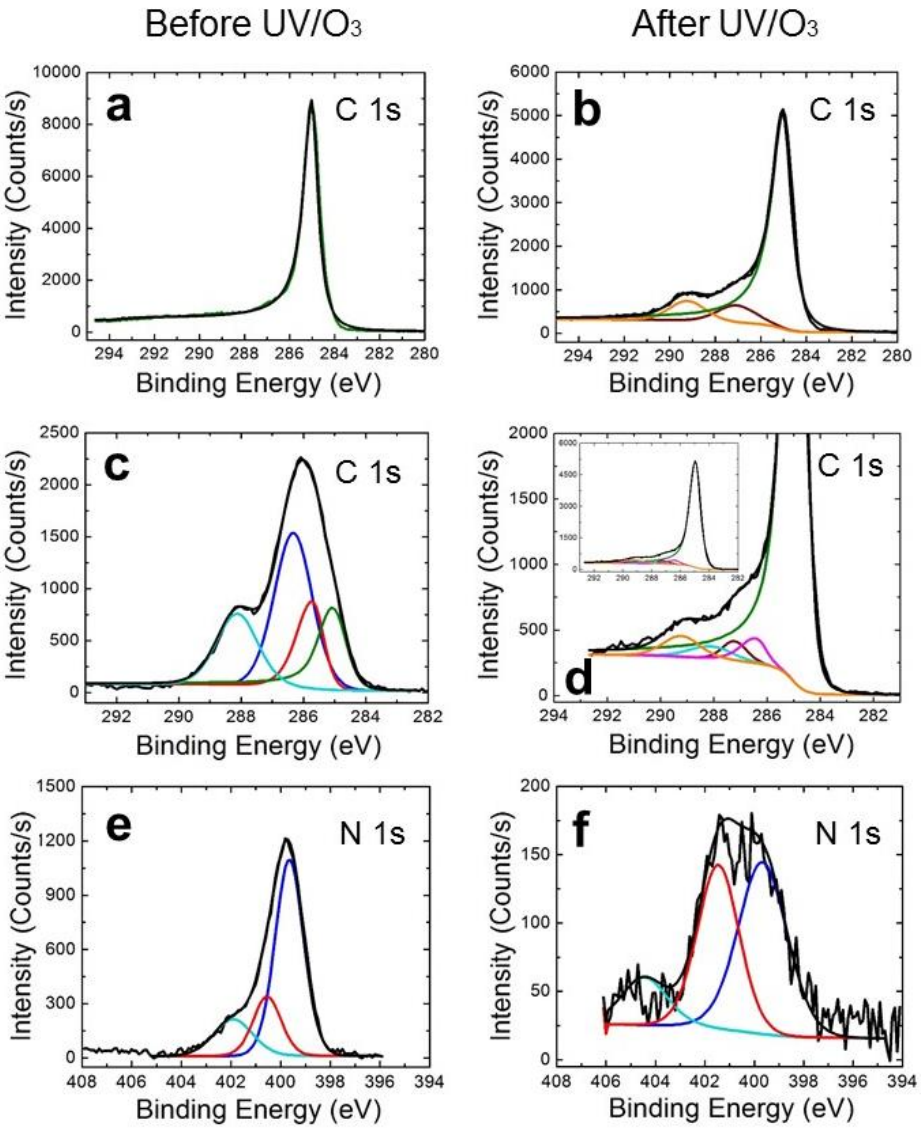

Figure 4.1: High-resolution XPS spectra in the C 1s region for a PPF electrode before (a) and after (b) UV/O_3 treatment. High-resolution XPS C 1s region of a PPF/G6-OH(Pt_{55}) electrode before (c) and after (d) UV/O_3 treatment. High-resolution XPS N 1s region of a PPF/G6-OH(Pt_{55}) electrode before (e) and after (f) UV/O_3 treatment.

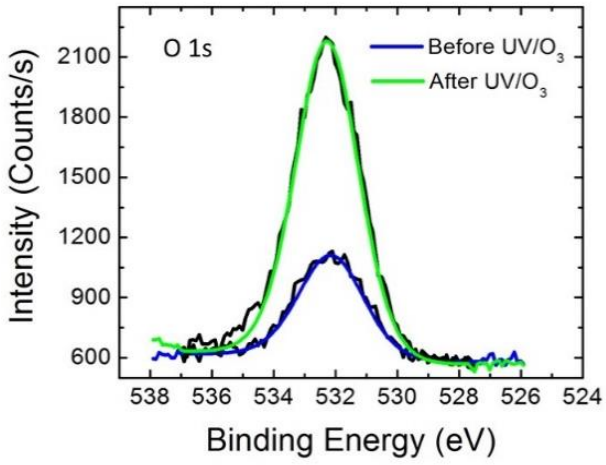

Figure 4.2: High-resolution XPS O 1s spectra of a PPF/G6-OH(Pt_{55}) electrode before (blue) and after (green) UV/O_3 treatment.

In addition to the XPS analysis, the effect of UV/O_3 treatment on the PPF electrodes was also examined by SEM (Figure 4.3). Prior to UV/O_3 treatment, the surface of PPF electrodes is remarkably smooth and uniform.[51,112] Importantly, there are no discernible changes to the morphology of the PPF surface after exposure.

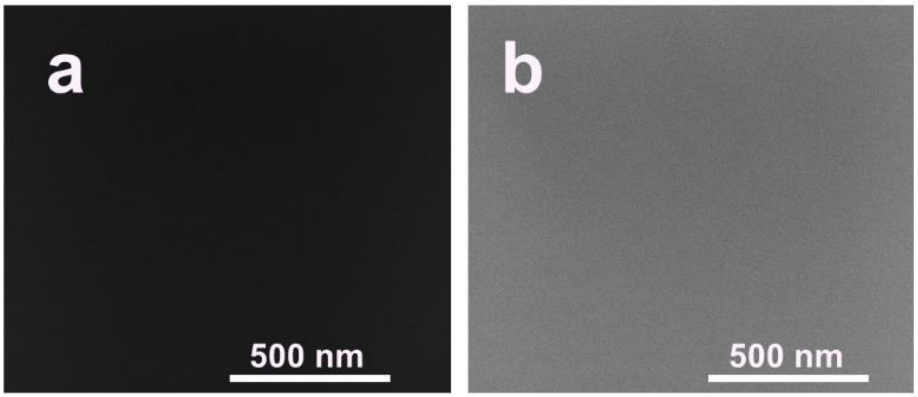

Figure 4.3: SEM micrographs of a PPF electrode (a) before and (b) after UV/O_3 treatment. Dust particles on the surface were used to focus the microscope.

Effect of UV/O_3 on G6-OH Dendrimers

We also used XPS to examine the effect of UV/O_3 on Pt DEN-modified PPF surfaces (PPF/G6-OH(Pt_{55})). Before exposure, the C 1s spectrum can be deconvoluted into four peaks (Figure 4.1c). The green colored peak at the lowest binding energy (BE) (285.0 eV) arises from the underlying PPF support, indicating that the PPF electrode is not completely covered by the Pt DENs.[133] The red peak at 285.6 eV corresponds to aliphatic carbons of the dendrimer, and the blue peak at 286.3 eV is due to the C−OH, C−N(amine), and C−N(amide) functionalities of the dendrimer. The final peak (turquoise) at the highest BE (288.0 eV) can be fit to the carbonyl carbons of the dendrimer.[122]

After the UV/O_3 treatment, changes in all four carbon regions are observed. Specifically, the green peak at 285.0 eV, corresponding to the underlying PPF electrode, becomes dominant after the dendrimers are removed from the PPF surface. The red and blue peaks that were previously observed separately coalesce in a single peak (purple) at 286.4 eV. The dark red peak at 287.2 eV and the orange peak at 289.2 eV can be assigned to phenolic and carboxylic carbon, respectively. As discussed earlier, these peaks arise from the oxidation of the underlying PPF support. Finally, the turquoise carbonyl peak of the dendrimer is still observed at ∼288.0 eV, but at a much lower intensity than before UV/O_3 exposure. Comparison of the intensities of dendrimer C 1s peaks before and after UV/O_3 treatment, indicates that only ∼8% of the overall dendrimer C signal remains after UV/O_3 (Tables 4.1 and 4.2).

Element	Assignment	Position (eV)	Area	Percent Concentration
C 1s	C-C bonds (PPF substrate)	285.0	1662.6	16.9
C 1s	Aliphatic	285.6	1366.0	14
C 1s	Hydroxyl, Amine, and Amide	286.3	3261.8	33
C 1s	Carbonyl	288.0	1633.1	17
N 1s	Amines	399.7	2180.1	12
N 1s	Amides	400.6	646.8	3.6
N 1s	Protonated Amines	401.9	556.7	3.1
Pt 4f	Metallic ($Pt\ 4f_{7/2}$)	72.0	401.9	0.26
Pt 4f	Metallic ($Pt\ 4f_{5/2}$)	75.2	192.5	0.13

Table 4.1: Summary of XPS Peak Assignments, Positions, Areas, and Concentrations for a PPF/G6-OH(Pt_{55}) Electrode before UV/O_3 Treatment.

Element	Assignement	Position (eV)	Area	Percent Concentration
C 1s	C-C (PPF substrate)	285.0	9304.5	84
C 1s	Aliphatic, Hydroxyl, Amine, and Amide	286.4	336.1	3.0
C 1s	Phenolic	287.2	242.2	2.1
C 1s	Carbonyl	288.0	264.3	2.3
C 1s	Carboxylic	289.2	389.6	3.5
N 1s	Amines	399.7	242.2	2.1
N 1s	Amides	401.5	352.3	1.7
N 1s	Protonated Amines	404.3	112.1	0.50
Pt 4f	Metallic ($Pt\ 4f_{7/2}$)	72.2	839.4	0.48
Pt 4f	Hydroxide	72.9	92.6	0.050
Pt 4f	Metallic ($Pt\ 4f_{5/2}$)	75.4	403.3	0.23
Pt 4f	Hydroxide	76.2	50.6	0.030
Pt 4f	Oxide	79.0	19.0	0.010

Table 4.2: Summary of XPS Peak Assignments, Positions, Areas, and Concentrations for a PPF/G6-OH(Pt_{55}) Electrode after UV/O_3 Treatment.

The N 1s spectrum of the PPF/G6-OH(Pt_{55}) electrode (Figure 4.1e) consists of

three peaks. The highest one (blue) is at 399.7 eV and is assigned to amine nitrogens, while the red peak (400.6 eV) corresponds to amide nitrogens.[122] The final peak, observed at 401.9 eV (turquoise), arises from protonated amines.[15] Recall that the DEN-modified substrates were prepared at pH 3.0, so it is reasonable to find this species present. Nevertheless, the identity of this peak was confirmed by immobilizing G6-OH dendrimers at four different pH values (9.0, 7.5, 5.0, 3.0) on PPF electrodes, and then analyzing the resulting samples using XPS (Figure 4.4). The spectra reveal that at pH values of 9.0 and 7.5 only two nitrogen peaks are observed, corresponding to amine and amide groups. As the pH value is lowered to 5.0, however, a new peak slowly emerges at higher BE. It becomes pronounced at pH 3.0, and hence our assignment to protonated amines.[15] The experimentally determined amide:amine nitrogen ratio is 1:3.3, which is not consistent with the ratio of 2:1 calculated based on the dendrimer structure. This lower ratio has been observed before, however, and it may be a consequence of the amide signal being screened compared to the amine signal.[122]

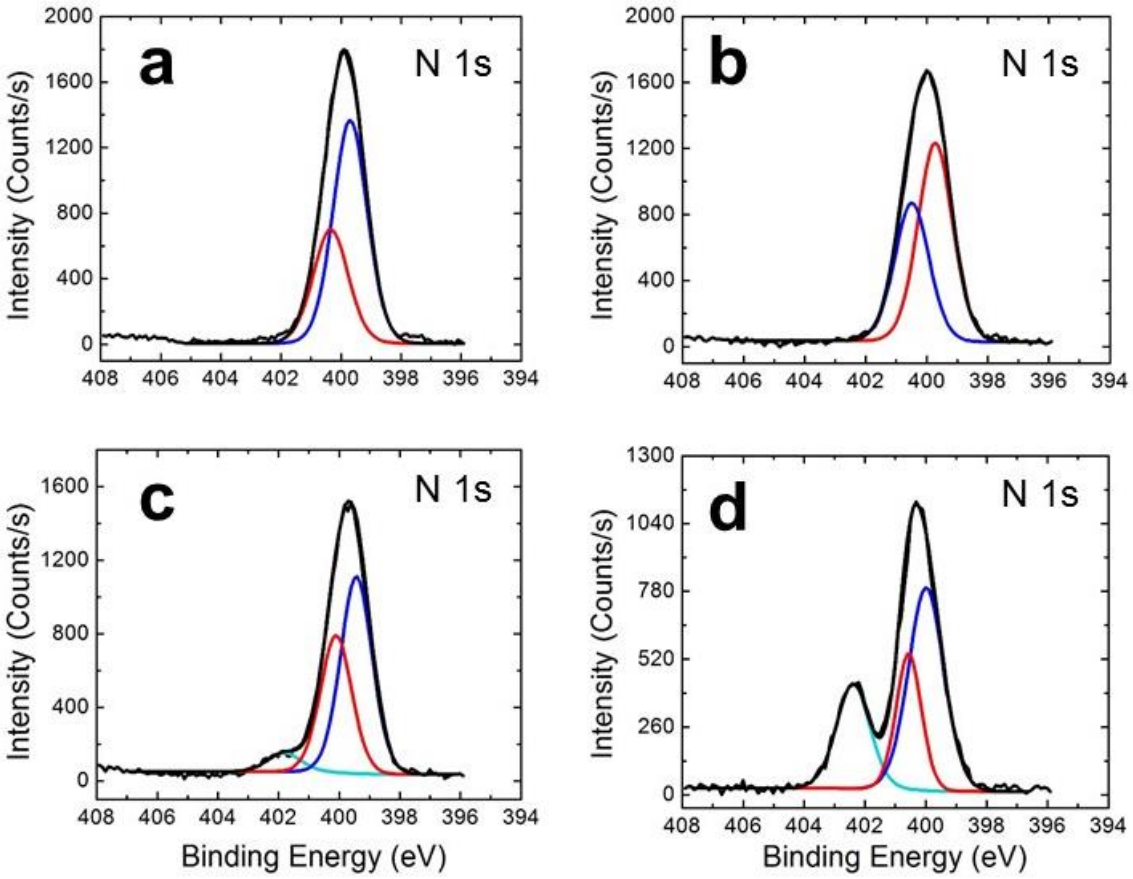

Figure 4.4: High-resolution XPS N 1s spectra for PPF/G6-OH electrodes, where the pH of G6-OH is (a) 9.0, (b) 7.5, (c) 5.0, (d) 3.0.

After the UV/O_3 treatment, the same nitrogen regions are observed in the N 1s spectrum, but at much lower intensities and with increased spacing between the peaks (Figure 4.1f). The relative intensities of the N 1s peaks before and after UV/O_3 treatment suggest that only ~23% of the original N signal is retained (Tables 4.1 and 4.2).

Effect of UV/O_3 on Pt DENs

Thus, far we have focused exclusively on the effect of UV/O_3 treatment on the dendrimer itself, but now we turn our attention to the encapsulated Pt DENs. Prior to

UV/O_3 treatment, XPS indicates that two Pt 4f peaks are present at 72.0 eV (Pt $4f_{7/2}$) and 75.2 eV (Pt $4f_{5/2}$) (Figure 4.5a). Although, these BE values are higher than expected for metallic Pt (71.2 for Pt $4f_{7/2}$)[90], we[13,112] and others[122] have previously observed this situation for DENs. The shift towards higher BE may result from the small size of the PtNPs.[13]

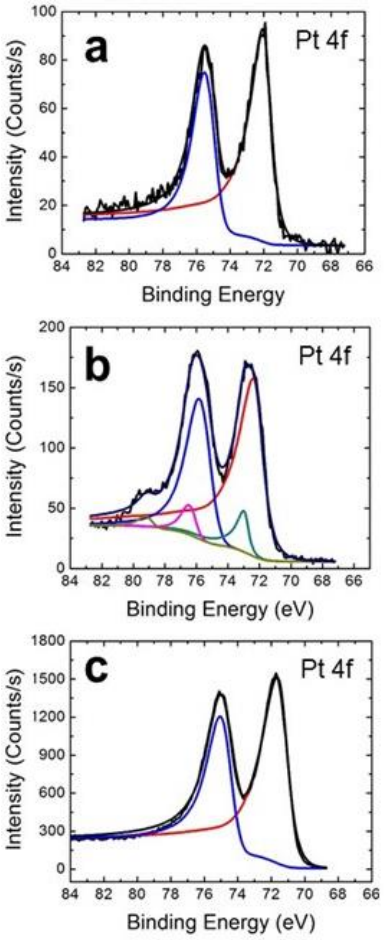

Figure 4.5: High-resolution XPS spectra in the Pt 4f region for a PPF/ G6-OH(Pt_{55}) electrode (a) before and (b) after UV/O_3 treatment. (c) Same as panel b, but after 10 electrochemical scans (scan rate = 50 mV/s) in an Ar-purged, aqueous 0.50 M H_2SO_4 solution to reduce the surface oxide created during the UV/O_3 treatment.

Figure 4.5b presents the Pt XPS spectrum after UV/O_3 treatment. In this case, three new peaks emerge. The peaks at 72.9 and 76.2 eV are assigned to $Pt(OH)_2$, while the peak at 79.0 eV can be fit to PtO. These oxygenated species on the DEN surface are a consequence of the oxidizing power of atomic oxygen. The two original Pt peaks attributable to metallic Pt are also still present in the spectrum, but they are shifted 0.2 eV toward higher BEs. Comparing the percent concentrations of the Pt peaks before and after the treatment, we calculate that ~10% of the original Pt signal arises from oxygenated species after UV/O_3 treatment (Table 4.1 and 4.2).

For studies of electrocatalysis, we prefer to start with unoxidized Pt DENs, and therefore we attempted to reduce the oxygenated fraction of the Pt surface electrochemically. Specifically, after the UV/O_3 treatment, the PPF/G6-OH(Pt_{55}) electrode was scanned 10 times between −0.65 and 0.63 V in Ar-purged, 0.50 M H_2SO_4. As indicated by the XPS spectrum in Figure 4.5c, this electrochemical method was successful: the peaks arising from oxidize Pt (Figure 4.5b) are eliminated, and just the original two peaks, corresponding to metallic Pt, are present at 71.8 and 75.0 eV. Note, however, that these values are ~0.2 eV lower than those of the original Pt DENs (Figure 4.5a).

STEM can be used to image Pt DENs before and after UV/O_3 treatment to determine if there are gross morphological changes. Within the resolution of the microscope (point-to-point resolution of 0.19 nm), Figure 4.6 indicates no UV/O_3 induced changes. Specifically, the Pt DENs appear spherical and have an average diameter of ~1.4 ± 0.3 nm before and after treatment.

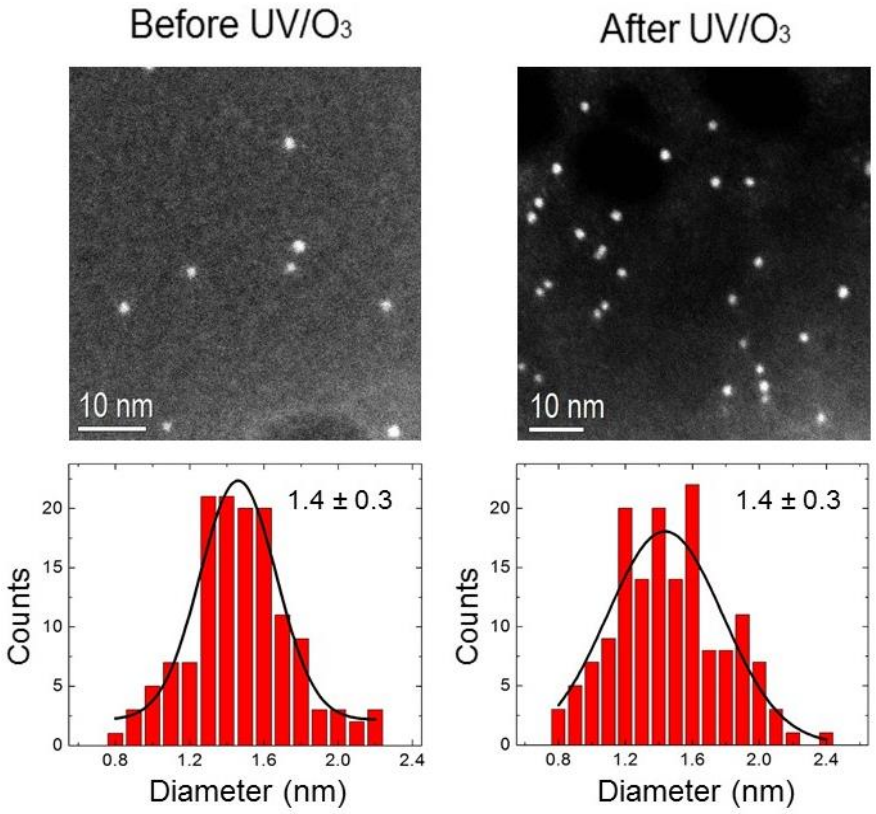

Figure 4.6: STEM micrographs and size-distribution histograms for G6-OH(Pt_{55}) DENs before (left) and after (right) UV/O_3 treatment. The size distribution is based on 200 randomly selected particles.

Location of Pt DENs

As discussed in the context of Figure 4.1, the UV/O_3 treatment presented here can be used to decompose most of the dendrimer templates from Pt DENs immobilized on PPF supports. To confirm removal of the dendrimers after the UV/O_3 treatment, however, we carried out a Pt surface poisoning experiment we have used previously to determine the location of the NPs.[90]

The poisoning experiment was performed on PPF/G6-OH(Pt_{55}) electrodes before and after UV/O_3 exposure using the following approach. First, a PPF/G6-OH(Pt_{55})

electrode that was not exposed to UV/O_3 was immersed in ethanol for 3 min, and then sufficient 1-decanethiol was added to the ethanol to make the solution 3.0 mM in the thiol. The electrode was left in this solution for 20 min. Second, the electrode was removed from the thiol solution and rinsed with ethanol and then with DI water. Finally, the potential of the electrode was scanned in an O_2-saturated, 0.50 M H_2SO_4 solution. The resulting cyclic voltammogram (CV), shown in red in Figure 4.7a, reveals a featureless shape characteristic of a passivated Pt surface. This result is interpreted as follows. Because ethanol is a good solvent for PAMAM dendrimers, the 1-decanethiol is able to diffuse through the dendrimer branches and adsorb to the PtNP surface. This inhibits the inner-sphere oxygen reduction reactions (ORR).

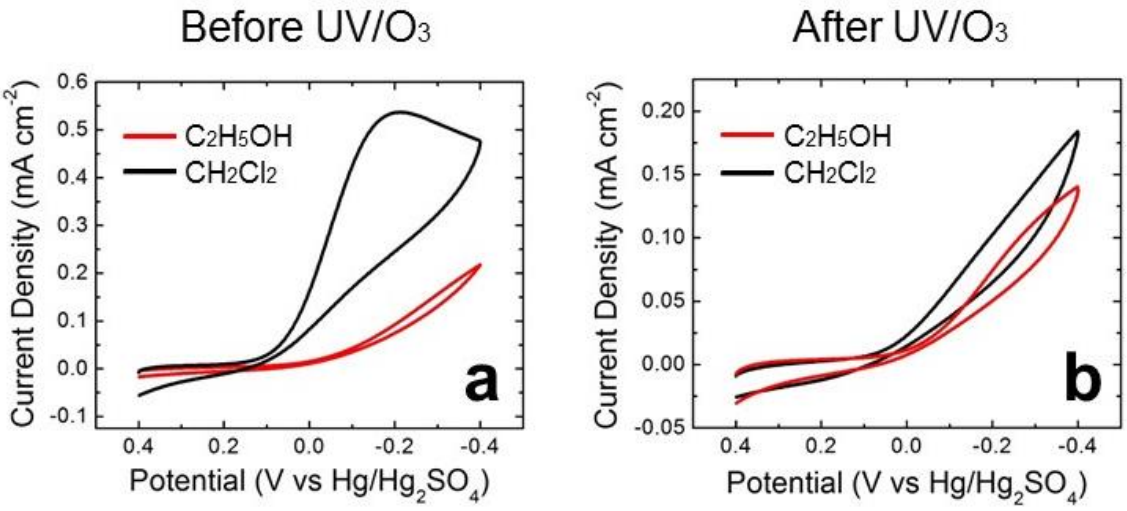

Figure 4.7: CVs obtained using PPF/G6-OH(Pt_{55}) electrodes (a) before and (b) after UV/O_3 treatment. In all cases the electrodes were exposed to 1-decanethiol in either CH_2Cl_2 (black) or ethanol (red) for 20 min. The aqueous 0.5 M H_2SO_4 solution was saturated with O_2. The scan rate was 50 mV/s.

Next, this same experiment was repeated, but now using CH_2Cl_2 instead of

ethanol. CH_2Cl_2 is a poor solvent for PAMAM dendrimers, and in its presence the dendrimers collapse around the encapsulated NPs and protect them from being poisoned with 1-decanethiol. The resulting well-defined ORR peak (black CV in Figure 4.7a) obtained after this experiment confirms that the Pt DENs were encapsulated within the dendrimers during exposure to the thiol/CH_2Cl_2 solution. The two experiments described previously were now carried out using PPF/G6-OH(Pt_{55}) electrodes following UV/O_3 exposure. The results of these experiments are summarized by Figure 4.7b. Now the CVs obtained after the poisoning experiments, using either ethanol (red CV) or CH_2Cl_2 (black CV), exhibit very low currents (note the difference in the current scales for Figures 4.7a,b). These observations are consistent with PtNPs being present on the PPF support as naked NPs without dendrimers present to shield them from 1-decanethiol. We conclude that these electrochemical experiments confirm the XPS results: nearly all of the dendrimer is removed by the UV/O_3 treatment, and so the Pt surface is fully exposed to the solution.

The ORR in the Presence and Absence of PtNP-PPF Support Interactions

The discussion up to this point demonstrates that UV/O_3 removes most of the dendrimer from the Pt DENs, and thus converts PPF/G6-OH(Pt_{55}) electrodes to PPF/Pt_{55} electrodes. Our ultimate objective in the series of studies that will follow this first report is to better understand how underlying supports affect electrocatalytic reactions. As a first step in that direction, we examined the ORR at PPF/G6-OH(Pt_{55}) and PPF/Pt_{55} electrodes.

Before obtaining CVs for the ORR, the PtNPs were electrochemically cleaned in an Ar-saturated, 0.50 M H_2SO_4 solution. Immediately thereafter, the electrodes were

immersed in an O_2-saturated 0.50 M H_2SO_4 solution, and then the potential was scanned between 0.40 V and −0.40 V (vs Hg/ Hg_2SO_4). Figure 4.8 compares CVs obtained for the ORR before and after UV/O_3 exposure. The results indicate that both electrodes are electrochemically active for the ORR and yield similar CVs. On the basis of four independent experiments, however, there are slight differences. For example, the peak current potential shifts from −84 ± 6 mV before UV/O_3 treatment to −62 ± 6 mV after removal of the dendrimer, indicating a slight improvement in reaction kinetics. The value of the peak current density, however, does not change within the error of the measurement (0.44 ± 0.02 mA/cm^2 vs 0.49 ± 0.04 mA/cm^2 before and after UV/O_3 treatment, respectively). We cannot be sure of the reason for the slight favorable shift in the ORR peak position in the absence of the dendrimer, but it might be due to the appearance of a few additional catalytic sites on each PtNP when the dendrimer is removed. As previously stated, however, the potential shift is very small and consistent with our previous claims that the presence of the dendrimer has little influence on the catalytic transformation of small molecules, like O_2, at the encapsulated DENs.[17,19] The results also indicate that the PPF electrode support has little effect on the ORR, which is also not surprising.

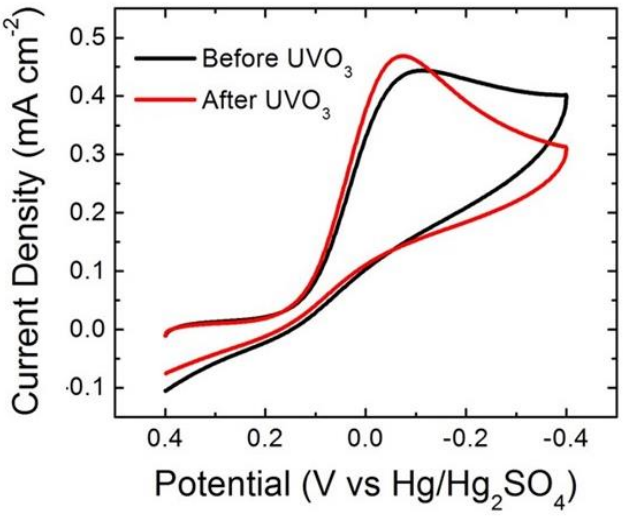

Figure 4.8: CVs obtained using PPF/G6-OH(Pt_{55}) electrodes and an aqueous 0.50 M H_2SO_4 solution saturated with O_2 before (black) and after (red) UV/O_3 treatment. The current density is based on the surface area of Pt determined by H-adsorption. The scan rate was 50 mV/s.

We also carried out chronoamperometric ORR experiments of the PPF/G6-OH(Pt_{55}) electrodes before and after UV/O_3 treatment (Figure 4.9). These data were obtained using an O_2-saturated, 0.50 M H_2SO_4 electrolyte solution and holding the electrode potential at −0.24 V (vs Hg/Hg_2SO_4) for 900 s. The results indicate that before UV/O_3 treatment the current density decreases most significantly during the first 60 s of the experiment (black). Between 60 and 900 s, the current density continues to decrease, but at a much lower rate. The shape of the chromoaperometric curve for the UV/O_3-treated electrode (red) is similar. The highest current density decrease is still during the first 60 s of the experiment, but the decrease at longer times is significantly larger. The monotonic decrease in both cases is due to O_2 exhaustion at the working electrode, because the solution was pre-saturated with O_2 but not stirred or continuously refreshed with O_2 during the experiment. The larger decrease in current after UV/O_3 treatment is

consistent with Figure 5 in the main text: better kinetics of the ORR in the absence of the dendrimer, and a correspondingly higher rate of O_2 exhaustion near the working electrode. The results are consistent with the CVs shown in Figure 4.9: slightly faster turnover of O_2 after removal of the dendrimer.

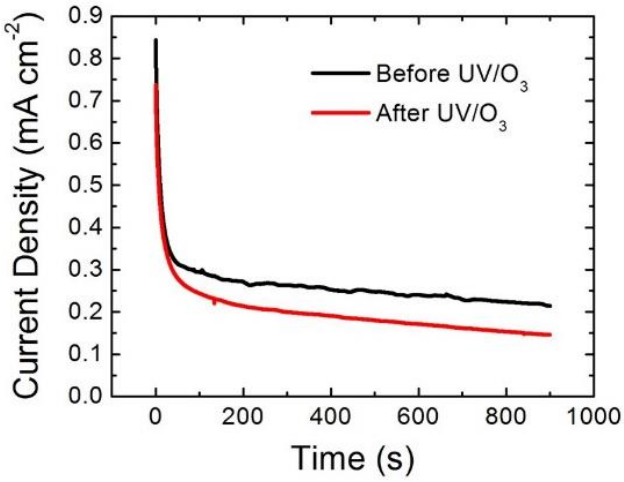

Figure 4.9: Chronoamperograms of PPF/G6-OH(Pt_{55}) electrodes before and after the UV/O_3 treatment obatined by holding the electrode potential at -0.24 V (vs. Hg/Hg_2SO_4) in an O_2 saturated, 0.5 M H_2SO_4 solution for 900 s.

SUMMARY AND CONCLUSIONS

Here we have shown that UV/O_3 can be used to almost entirely remove G6-OH PAMAM dendrimers from surface-confined Pt DENs without changing their size, shape, or electrocatalytic properties. These points are important for two reasons. First, they suggest that the dendrimer itself has very little influence on the electrocatalytic properties of the encapsulated NPs. This is important because it means that results obtained using DENs reliably extrapolate to the electrocatalytic properties of other types of naked NPs. Second, the fact that the dendrimer can be cleanly removed without significantly

changing the DENs makes it possible to study electrocatalytic reactions in the presence and absence of support interactions (Illustration 4.1). In other words, this is a near-perfect system for studying support effects, because the exact same electrode can be examined with support effects turned on or off simply by removing the dendrimer by UV/O_3.

One last point. Fermin,[31,32,61,62] Gooding,[33,63] and others[52,57–60,64,134,135] have shown that electron transfer across thin insulating layers is not inhibited if NPs are present on the solution side of the insulator. We recently confirmed their findings using DENs as the NPs and ultrathin layers of Al_2O_3, deposited by atomic layer deposition, as the insulator.[112] Those findings, taken together with the results reported in this chapter, mean that it will now be possible for us to examine electrocatalytic reactions on essentially any oxide or nitride support using any type of catalytic DEN. These experiments are currently underway in our lab, and the results will be reported in due course.

Chapter 5: Microelectrochemical Flow Cell for Studying Electrocatalytic Reactions on Oxide-Coated Electrodes[3]

INTRODUCTION

In the field of gas-phase heterogeneous catalysis, it is well-known that support materials, such as oxides and nitrides, can dramatically affect the catalytic performance of metal nanoparticles (NPs).[2,9,136,137] Recently, we wondered if such strong metal−support interactions (SMSIs) influence electrocatalytic reactions in the same way. There are only a few reports in the literature of such systems for the very obvious reason that one normally does not think of carrying out electrochemical reactions on insulating surfaces.

The first reports of the effect of SMSIs on electrocatalytic reactions were from the Adzic group.[7,129,138–142] They used a very clever experimental model, called inverse catalysts, for studying these types of systems. For example, Adzic and co-workers deposited SnO_x nanoislands on Pt(111) and examined the effect of this modification on the electrochemical activity of the ethanol oxidation reaction (EOR).[139] Chronoamperometry (CA) and current−potential polarization studies revealed that the activity of Pt(111) for the EOR is enhanced by the presence of SnO_x. The Adzic group also utilized cyclic voltammetry (CV) and CA to study the effect of SnO_x NPs on the electrochemical activity of polycrystalline Pt (pc-Pt) for the methanol oxidation reaction (MOR).[141] The resulting pc-Pt/SnO_x electrode exhibited up to a 40-fold enhancement in current for the MOR compared to a naked pc-Pt electrode. Even more interestingly, the

[3] Anderson, M. J.; Ostojic, N.; Crooks, R. M. Microelectrochemical Flow Cell for Studying Electrocatalytic Reactions on Oxide-Coated Electrodes. *Anal. Chem.* **2017**, *89* (20), 11027–11035 I was first coauthor on this publication working together with M. J. Anderson. Dr. R. M. Crooks supervised the project.

degree of enhancement was found to depend on the size of the SnO_x NPs. In both of these studies, X-ray photoelectron spectroscopy (XPS) provided evidence that the presence of SnO_x aids in the removal of chemisorbed CO on Pt, reducing the level of poisoning and, thereby, enhancing catalyst performance.

Recently, we have been focusing on the design of very well-defined models for studying the effect of SMSIs on electrocatalysis. The approach we have taken relies on NP-mediated electron transfer (eT) across thin insulating layers, which is a phenomenon that has been discussed at length by Fermin,[30,32,143] Gooding,[33,34] and others.[35,60,65,68,72,127,144,145] Moreover, we recently confirmed these findings for a model system consisting of an ultrathin insulating metal oxide (Al_2O_3) and PtNPs having sizes on the order of ∼2 nm.[112] In that report, the oxide was deposited onto a carbon electrode by atomic layer deposition (ALD) and had a thickness of 2.4−3.5 nm. Pt dendrimer-encapsulated nanoparticles (Pt DENs)[11,19,43] served as the metal catalysts. We also showed that the dendrimer scaffold around the PtNPs could be cleanly removed, without changing the size of the NPs, using a UV/O_3 process developed in our lab.[146] This places the NPs in direct contact with the electrode surface. Accordingly, at this point in our studies we have confirmed the existence of a well-defined model system (Illustration 5.1) that is appropriate for studying SMSIs for a variety of insulating thin films and metallic NPs having sizes in the interesting ∼2 nm size range.[2,45] We are now ready to begin quantitative study of electrocatalytic reactions on these model electrode surfaces.

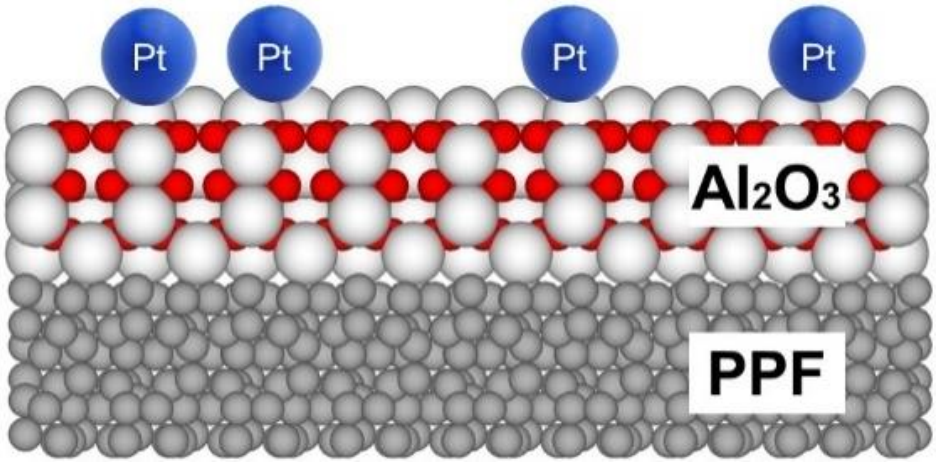

Illustration 5.1: Schematic representation of a PPF/Al_2O_3/PtNPs electrode after the removal of the dendrimers.

The primary tool used for studying the kinetics and products of interfacial electrochemical reactions is the rotating ring-disk electrode (RRDE).[147–149] RRDEs consist of a disk generator electrode (GE) surrounded by a concentric ring collector electrode (CE). In RRDE voltammetry an electrode is rotated to increase the rate of mass transfer of solution-phase reactants to an electrode surface. This often makes it possible to determine whether reactions are limited by mass transfer or kinetics. Moreover, if the products of the reaction are electrochemically active, they can be analyzed at the ring electrode.

Although in wide usage, RRDEs are not well-suited for studying reactions at electrode surfaces modified by ALD or other common techniques that have been optimized for Si wafers or glass slides. This is primarily a consequence of the form factor of RRDEs, which are cylinders having macroscopic dimensions. Accordingly, we have recently been investigating the use of electrochemical flow cells as an alternative to the RRDE for making kinetic measurements and determining product distributions using the

SMSI model. These types of devices, which were developed by the Compton,[150–155] Unwin,[156–160] and Macpherson,[157,161,162] groups, as well as by us,[92,163,164] consist of colinear GEs and CEs confined within a rectangular channel. In analogy to the RRDE, a reaction is driven at the upstream GE and the products are carried by laminar flow to the downstream CE where they can be analyzed (if they are electroactive). In their current form, however, these types of flow cells suffer from one of the same shortcomings as RRDEs. Specifically, the electrodes are difficult to modify and characterize once the cell has been assembled.

To address this latter point, we report here a new kind of microelectrochemical flow system that is well suited for studying modifications, like ALD, that require substrates having a two-dimensional form factor. The design is similar to that of the types of microelectrochemical flow systems that have been previously reported,[92,156,157,161–163,165–168] but it allows for the electrodes to be modified ex situ and then incorporated directly into the flow cell. We have found that this attribute is critical for maintaining the integrity of fragile, ultrathin metal oxide layers. Additionally, this design makes it possible to remove electrodes from the cell between experiments, alter the surface modification, and then reinstall the same electrode into the cell for further analysis.

In the present manuscript we describe this new microelectrochemical flow system (Illustration 5.2) within the context of PtNPs supported on ultrathin metal-oxide (Al_2O_3) films. The results indicate that this design is able to achieve mass-transfer coefficients (k_t) of up to 0.011 cm/s, which is comparable to those attainable by RRDE (typically 0.005 to 0.011 cm/s).[24,169] Importantly, the collection efficiency at the CE (N) of products produced at the GE are in the range of 57 ± 10%, varying with flow rate, compared to ~37% for the RRDE.[170] We tested the flow cell using ALD- and DEN-modified

substrates (Illustration 5.2) and achieved results that are consistent with prior reports.

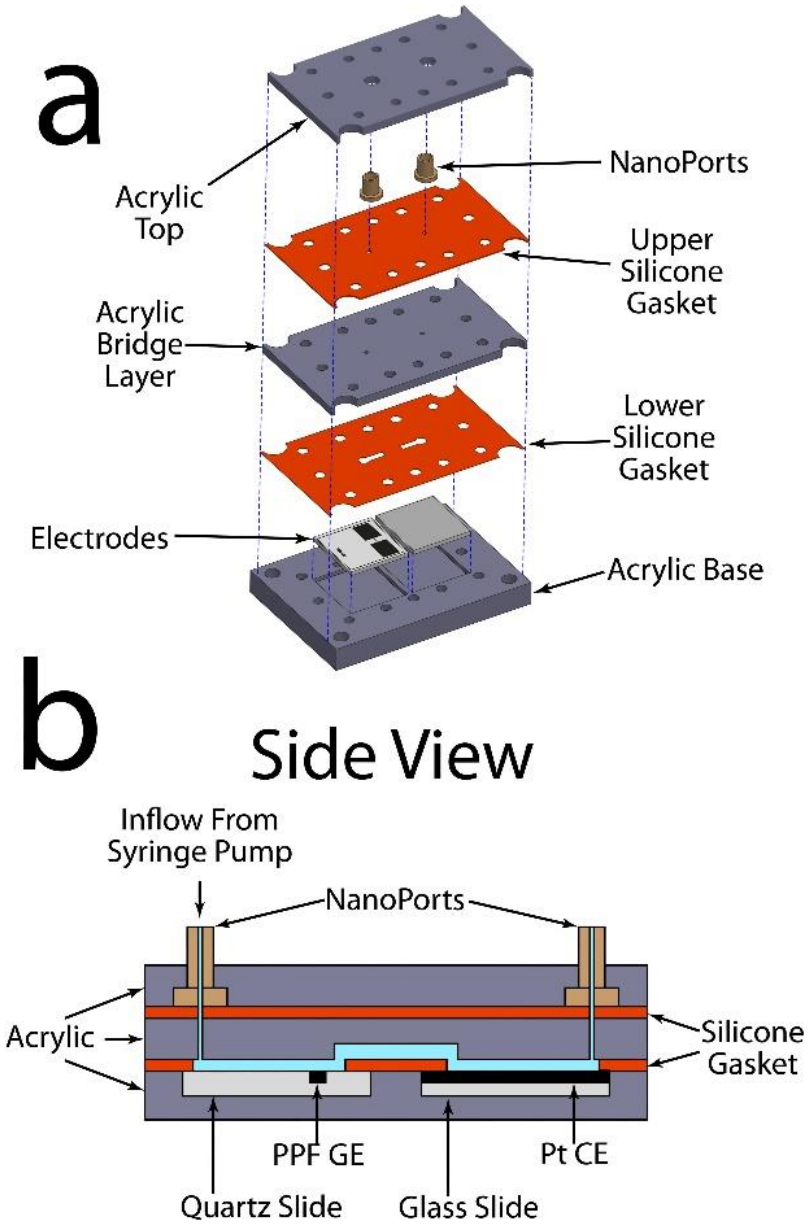

Illustration 5.2: Schematic illustration of (a) individual pieces of the microelectrochemical flow cell and (b) the side view of the flow cell.

EXPERIMENTAL SECTION

Activation of PPF Electrodes

Prior to expositing the resulting PPF slides to ALD, the slides were activated with UV/O_3 using a commercial UV/O_3 system (PSD-UV4 with OES1000D, Novascan Technologies, Ames, IA). Individual PPFs were placed in the center of the chamber ~2 cm from the UV lamp. The vacuum was turned on, and after 3 min an external supply of O_2 was introduced into the chamber at 775.7 mmHg for 5 min. The O_2 flow was then stopped and the UV lamp was turned on for 5 min. The process of exposing the PPF sample to O_2 flow and then to the UV lamp was repeated two more times. After the UV/O_3 treatment, PPFs were placed into the ALD chamber within 2 min.

Synthesis of Pt DENs

Pt DENs were synthesized using a previously published procedure based upon galvanic exchange. Specifically, 1.0 mL of 100.0 μM sixth-generation, hydroxyl-terminated (G6-OH) poly(amidoamine) (PAMAM) dendrimers was diluted in 8.68 mL of DI water. Next, 55 equiv of 20.0 mM $CuSO_4$ were pipetted into the G6-OH solution. The solution was sealed and stirred under N_2 for 15 min. Next, a 5-fold molar excess of an aqueous 1.0 M $NaBH_4$ solution was added dropwise under N_2 to reduce intradendrimer Cu_2^+ to CuNPs. The reduction was carried for 45 min, and then the pH of the resulting G6-OH(Cu_{55}) DENs was adjusted to 3.0 using 1.0 M $HClO_4$. Finally, sufficient aqueous 10.0 mM $PtCl_4^{2-}$ (Pt^{2+}:Cu = 1) was added dropwise (under N_2) to initiate galvanic exchange. The solution was sealed and left to stir for 60 min under N_2. The Pt DENs were immobilized atop PPF/Al_2O_3 electrodes by immersing the latter in the Pt DENs solution (pH 3.0) for 30 min. After 30 min, the electrodes were rinsed under a gentle flow

of NERL reagent-grade water and dried under low-pressure N_2. The newly formed PPF/Al_2O_3/G6-OH(Pt_{55}) electrodes were left to dry for at least 90 min prior to use. The final concentration of the Pt DEN solution was 10.0 μM. Pt DENs appeared spherical and had an average diameter of 1.4 ± 0.2 nm (Figure 5.1).

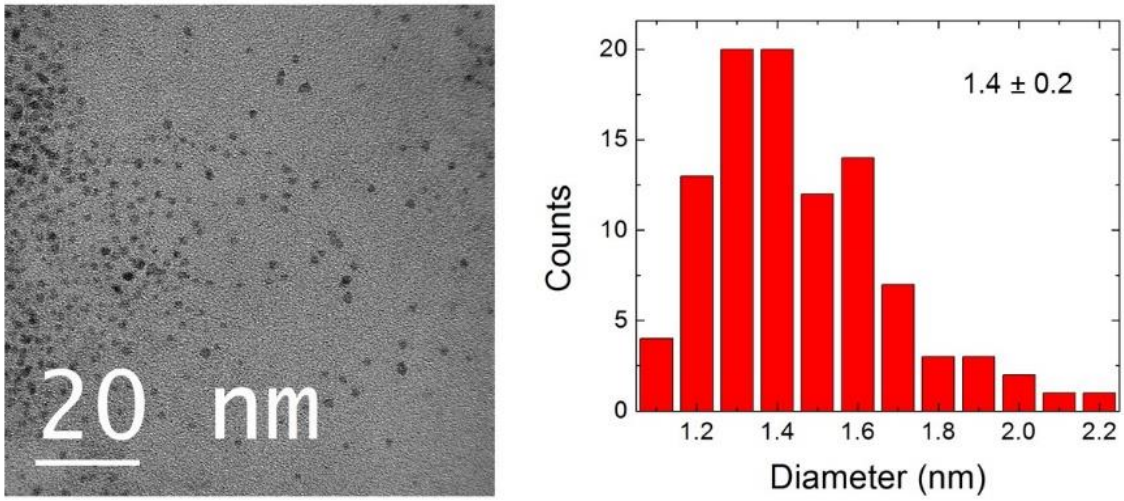

Figure 5.1: (Left) Transmission electron micrograph and (right) size-distribution histogram for the G6-OH(Pt_{55}) DENs used in this work.

UV/O_3 Treatment for Decomposition of G6-OH Dendrimers

The G6-OH dendrimers were removed from the PtNPs using a modified version of the UV/O_3 process we have described previously.[146] Briefly, individual PPF/Al_2O_3/G6OH(Pt_{55}) electrodes were placed in the center of the UV/O_3 chamber and treated using the following protocol, which resulted in maximum dendrimer decomposition and minimal PtNP surface oxidation. First, the vacuum was turned on and an external supply of O_2 was introduced into the chamber at 259 mmHg for 15 min. Second, the O_2 flow was stopped and the UV lamp was turned on for 5 min. After turning off the UV lamp, the chamber was purged with O_2 (259 mmHg) for 10 min. The last two

steps were repeated five times. Next, the O_2 flow was stopped and the UV lamp was turned on for 5 min, following which the chamber was purged with O_2 for 15 min. O_2 was turned off and the UV lamp was turned on for another 15 min. Finally, the UV lamp was turned off and the electrode was left inside the chamber for 15 min.

X-ray photoelectron spectroscopy (XPS). XPS samples were prepared by immobilizing Pt DENs atop Al_2O_3-modified PPF electrodes as previously described. XPS was carried out using a Kratos Axis Ultra spectrometer (Chestnut Ridge, NY) having an Al Kα source. Samples were grounded using metal holders. Careful placement of the PPF/Al_2O_3/G6-OH(Pt_{55}) electrode made it possible to characterize the same location before and after UV/O_3 treatment. This was important because the G6-OH(Pt_{55}) aliquot did not dry uniformly on the Al_2O_3 support. XPS spectra were collected using a 0.10 eV step size and a band pass energy of 20 eV. Binding energies (BEs) were calibrated against the C 1s carbonyl peak of G6-OH dendrimer (288.5 eV).[132] CasaXPS (version 2.3.15, Casa Software, Teignmouth, UK) was used for peak fitting and analysis. A mixed Gaussian/Lorentzian model was used for symmetric line-shapes, while an asymmetric Lorentzian model was applied for asymmetric line shapes.

Flow Cell Design

The flow cell was constructed from layers of 500 μm-thick silicone and 6.3 mm-thick acrylic sheets. The silicone and acrylic pieces were cut using a commercial CO_2 laser cutter (Epilog Zing 16, 30W, Golden, CO). Silicone sheets were cut using 10% power, 100% speed, and 5000 Hz frequency. Acrylic sheets were cut using 100% power, 5% speed, and 5000 Hz frequency.

The individual pieces of the flow cell were prepared as follows, starting from the bottom of Scheme 5.2a. The laser was rastered (3 passes at 40% speed and 80% power) across the acrylic base layer to create two 2.5 cm x 2.5 cm recessions to accommodate the GE and CE (Figure 5.2a). The electrodes were placed in the base acrylic layer and affixed with Cu tape (Figures 5.2b and 5.2c). The lower silicone gasket was cut to create two separate channel segments and seal the edges to prevent leaking where the electrodes and the acrylic base layer meet (Figure 5.2d). This silicone layer resulted in a gap of between 10.1 and 11.5 mm between the two electrodes, constrained the width of the channel to 500 μm, and limited the CE length exposed to the flowing solution to 7.6 mm. The acrylic bridge layer was fabricated by rastering the laser (2 passes at 80% speed and 100% power) across the surface to create a lip around the channel. This layer was further etched (4 passes at 80% speed and 100% power) to create a fluidic pathway for solution to flow between the two silicone channel sections (Figure 5.2e). Holes were cut through this acrylic layer for solution to flow to the channel layer.

The upper silicone gasket was cut to size, and then holes were added for fluid flow (Figure 5.2f). This sheet creates a seal between the bridge acrylic layer and the NanoPorts. The top acrylic layer was etched to accommodate the lip of the NanoPorts, hold them in place, and create a seal between the NanoPort assembly and the upper silicone gasket when the cell is secured (Figure 5.2g).

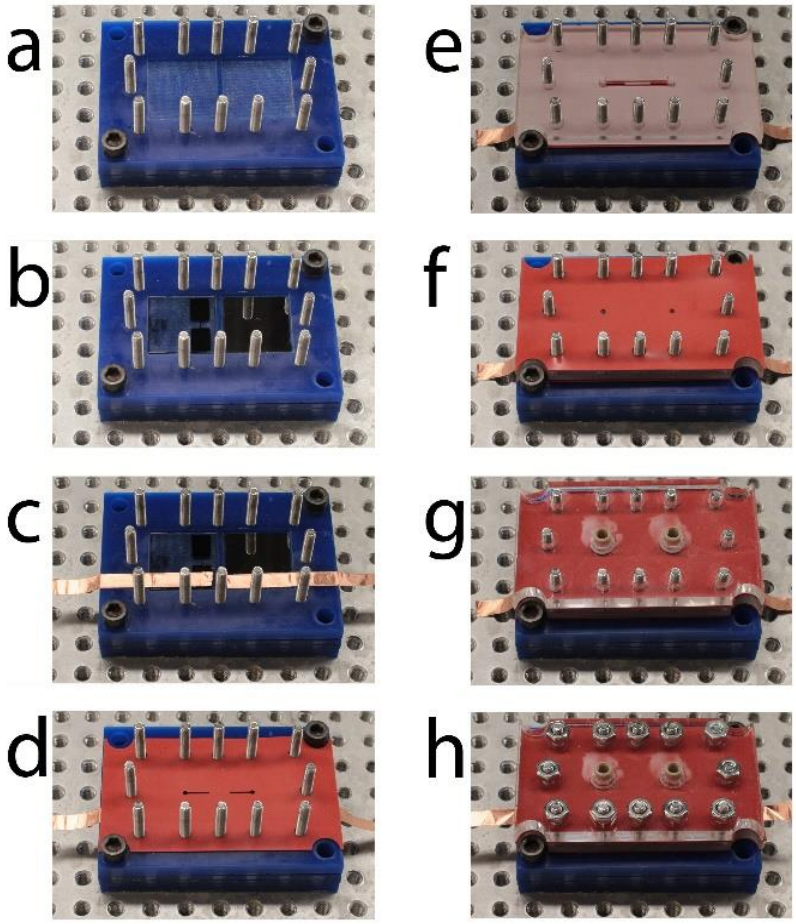

Figure 5.2: Photographs showing the step by step assembly of the flow cell used in this work.

The flow cell was assembled as illustrated in Illustration 5.2a and secured with nuts (Figure 5.2h). The nuts were tightened in a cross pattern to evenly distribute pressure across the electrodes. One of the NanoPorts was connected to a syringe pump (Pico Pump Elite, Harvard Apparatus, Holliston, MA) outfitted with a 10 mL gas-tight syringe (Model 1010, Hamilton, Franklin, MA) and PEEK tubing. The other NanoPort was connected to an outlet reservoir where the reference and counter electrodes were placed. Figure 5.3 is a photograph of the assembled flow cell.

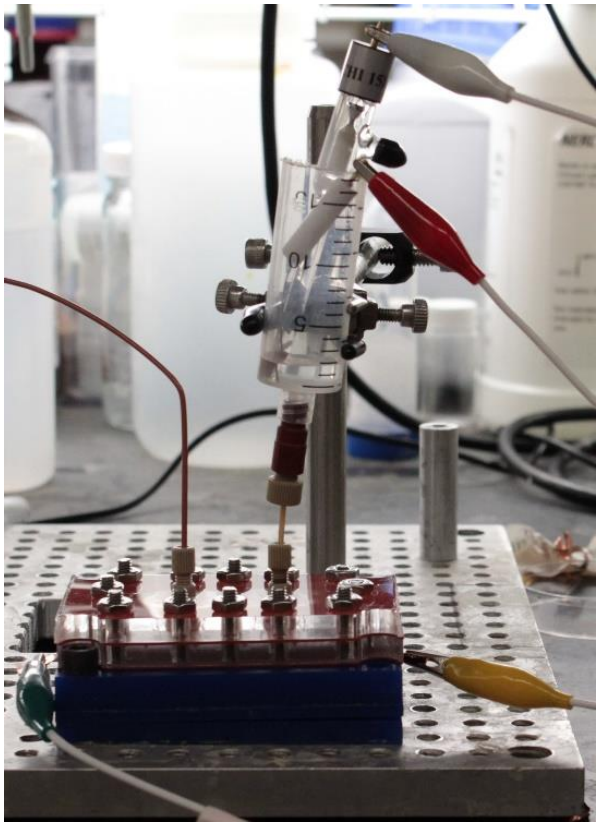

Figure 5.3: A photograph of the assembled flow cell.

Fabrication of Pt Collector Electrodes

Pt collector electrodes were fabricated by physical vapor deposition. Electrodes consisted of a 20 nm Ti adhesion layer and 100 nm Pt deposited onto 2.5 cm x 7.5 cm unpatterned glass slides. Following deposition, the slides were cut into 2.5 cm x 2.5 cm pieces and rinsed with ethanol prior to use.

RESULTS AND DISCUSSION

Flow Cell Design and Characterization

Details regarding the flow cell design and construction are provided in the Supporting Information. Briefly, however, it consists of a flow channel defined by a laser-cut silicone gasket (Illustration 5.2). Within the channel, there are two electrodes: a PPF carbon generator electrode (GE) and a larger, downstream Pt collector electrode (CE). These electrodes are thin films on quartz and glass substrates, respectively, that fit into recessed regions of the acrylic base plate. The flow cell was designed such that the gap between the GE and the CE ranged from 10.1 to 11.5 mm, depending on the length of the quartz substrate on which the GE is patterned, and the channel width was 500 μm. The GE and CE lengths were 100 μm and 7.6 mm, respectively. In operation, the inlet is connected to a syringe pump via a NanoPort, the channel is purged with solution to remove bubbles that might be present, and then the outlet is connected to an external reservoir containing the reference and counter electrodes.

Hydrodynamic cells, like the one described here, exhibit high rates of mass transfer (k_t) compared to nonconvective techniques, and this makes it possible to determine reaction kinetics and mechanisms.[24,147,148,171–174] Generation-collection techniques are used to simultaneously drive an electrochemical reaction and analyze the resulting products.[92,147,149,175,176] A generation-collection experiment is carried out by applying an appropriate potential to an upstream GE sufficient to drive an electrochemical reaction. The products of this reaction are carried by laminar flow to a downstream CE where a second electrochemical reaction occurs (sometimes the reverse of the reaction at the GE).[24,147,149,175] A key parameter in generation-collection experiments is the collection efficiency (N), which is defined by Equation 5.1, where

i_{lim}^{CE} and i_{lim}^{GE} are the mass transfer-limited currents at the CE and GE, respectively.[24,149,177]

$$N = -\frac{i_{lim}^{CE}}{i_{lim}^{GE}} \quad (5.1)$$

Characterization of the flow cell illustrated in Illustration 5.2 was carried out following previously established electrochemical methods, which amount to observing the relationship between i_{lim}^{GE} and the volumetric flow rate, V_F, using a reversible, outer-sphere redox probe such as $Fc(MeOH)_2$.[92] The relationship between i_{lim}^{GE} and V_F under laminar flow conditions can be described by the Levich equation (eq 2).[175,177]

$$i_{lim}^{GE} = 0.925nFCw\left(\frac{D^2x_e^2V_F}{dh^2}\right)^{1/3} \quad (5.2)$$

Here, n is the number of electrons transferred, F is Faraday's constant, C is the concentration of the redox probe, D is the diffusion coefficient of the redox probe, d and h are the width and half-height of the channel, respectively, and w and x_e are the width and length of the electrode, respectively. The important prediction of Equation 5.2 is that there is a linear relationship between i_{lim}^{GE} and $V_F^{1/3}$ under laminar flow conditions (Reynolds number < 2000).[172,177–179]

The cyclic voltammograms (CVs) shown in Figure 5.4a were obtained for $Fc(MeOH)_2$ oxidation in the flow cell (Illustration 5.2). Specifically, a solution containing 1.0 mM $Fc(MeOH)_2$ and 0.10 M KNO_3 was introduced to the cell, and V_F was varied as indicated in the figure. Consider the CV for V_F = 10μL/min first. As the potential of the GE is scanned from −0.50 to 0.20 V, the current becomes more negative, reaches a peak, and then achieves a mass transfer limited, steady-state value. The peak is present because

both diffusion and convection contribute significantly to the shape of the voltammogram at this low flow rate.[177]

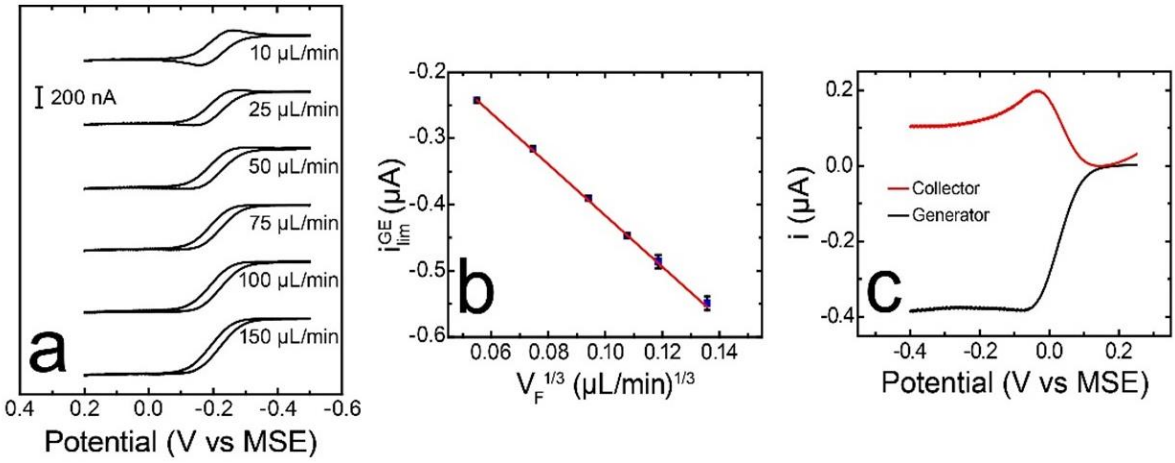

Figure 5.4: (a) CVs obtained at a naked PPF GE for the oxidation of 1.0 mM $Fc(MeOH)_2$ in an aqueous solution containing 0.10 M KNO_3. The flow rates are indicated in the legend. (b) Plot of i_{lim}^{GE} vs $V_F^{1/3}$ constructed from chronoamperometry experiments. The data were obtained by stepping the GE potential from −0.50 to 0.20 V for 20 s to drive the oxidation of 1.0 mM $Fc(MeOH)_2$. The error bars represent the standard deviations for three measurements. The red line is the best linear fit to the data ($R^2 = 1.00$). (c) Representative chronoamperograms for a generation-collection experiment in a flowing solution containing 1.0 mM $Fc(MeOH)_2$ and 0.10 M KNO_3 (V_F = 75µL/min). The GE was stepped from −0.50 to 0.20 V for 20 s and then back to −0.50 V. The CE was held at −0.50 V.

When V_F increases to 25 µL/min the peak remains, but it is less prominent, and the hysteresis between the forward and reverse scans is slightly decreased. These changes are a consequence of the increase in V_F causing the contribution of diffusion, relative to convection, to become less significant. As V_F is further increased the peak disappears altogether, resulting in sigmoidal-shaped CVs characteristic of mass transport-limited

conditions, and the magnitude of the hysteresis decreases further. On the basis of these results, we conclude that the characteristics of the flow cell are interpretable in terms of well-understood mass-transfer phenomena.

The channel height (2h) of the flow cell can be calculated using Equation 5.2. The necessary data were obtained by stepping the potential of the GE from −0.50 to 0.20 V for 20 s in flowing solutions containing 1.0 mM $Fc(MeOH)_2$ and 0.10 M KNO_3. Figure 5.4b is the resulting linear plot of i_{lim}^{GE} vs $V_F^{1/3}$.[172,175,177] Using the slope of this line and Equation 5.2, the channel height is determined to be 457 μm. The average channel height, calculated from four independent experiments using four different electrodes is 448 ± 22 μm.

The mass-transfer coefficient, k_t, can be calculated from i_{lim}^{GE} and Equation 5.3.[24]

$$k_t = \frac{i_{lim}^{GE}}{nFAC} \qquad (5.3)$$

Here, A is the geometric area of the electrode and the other variables have already been defined. In this study, the highest value of i_{lim}^{GE} was 549 ± 10 nA, which corresponds to k_t = 0.011 cm/s. This value is comparable to those attainable by RRDE (k_t = ~0.01 cm/s).[170] Collection efficiency of the flow cell (*N*) was measured by stepping the GE from -0.50 V to 0.20 V while holding the CE at -0.50 V (vs Hg/Hg_2SO_4) in a flowing solution containing 0.10 M KNO_3 and 1.0 mM $Fc(MeOH)_2$. The resulting values of i_{lim}^{GE} and i_{lim}^{CE} were used to calculate N based on Equation 5.1. The error bars represent the standard deviation from the mean for four independent measurements (using a different electrode for each set of measurements) at each flow rate. The measured values of i_{lim}^{GE} and i_{lim}^{CE} obtained from four independent chronoamperometry measurements (an example of one of these is shown in Figure 5.4c) for different values of V_F yield N = 57±

10% (Equation 5.1). Within error, the value of N did not change significantly as a function of V_F, as shown in Figure 5.5. This collection efficiency is higher than values attainable by RRDE (N = 37%)[170] and, hence, results in increased sensitivity for this flow cell method. Note, however, that both k_t and N are lower than values we have previously reported for microelectrochemical flow cells having much smaller channel dimensions (kt = 0.5 cm/s, N > 95%).[92,164]

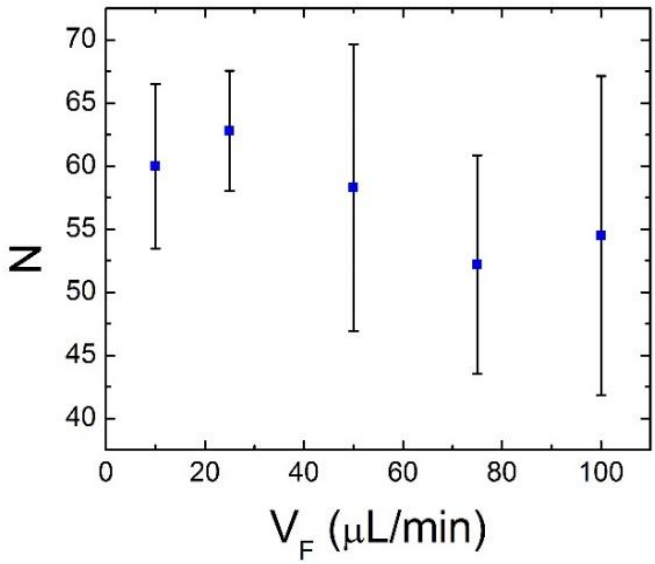

Figure 5.5: Measured collection efficiencies (N) as a function of volumetric flow rate (V_F). The GE was stepped from -0.50 V to 0.20 V while holding the CE at -0.50 V in a flowing solution containing 0.10 M KNO_3 and 1.0 mM $Fc(MeOH)_2$. The error bars represent the standard deviation from the mean for four independent measurements (using a different electrode for each set of measurements) at each flow rate.

Decomposition of G6-OH Dendrimers

Previously, we showed that UV/O_3 can be used to nearly completely remove the dendrimer from G6-OH(Pt_{55}) DENs immobilized onto a naked PPF electrode.[146]

Recalling that PAMAM dendrimers are mostly composed of carbon, nitrogen, and oxygen, XPS showed that the UV/O_3 treatment results in a 92% decrease of the dendrimer C 1s signal and a 78% decrease in the dendrimer N 1s signal. Importantly, this decomposition process does not affect the size or shape of the encapsulated PtNPs.[146]

In the present study, we are also interested in decomposing G6-OH dendrimers, but in this case starting with G6-OH(Pt_{55}) DENs immobilized on Al_2O_3-modifed PPF electrodes rather than naked PPF. Hence, we modified our previously published UV/O_3 procedure[146] in a way that maximizes dendrimer decomposition without damaging the underlying Al_2O_3 layer. Subsequently, XPS was used to evaluate the extent of dendrimer removal from the PPF/Al_2O_3/G6-OH(Pt_{55}) electrode by comparing the surface composition before and after the UV/O_3 treatment. Prior to the UV/O_3 treatment, the XPS peaks were referenced to the known position of the dendrimer carbonyl C 1s peak at 288.5 eV.[122,146] However, after the UV/O_3 treatment the intensity of this peak decreased significantly and so it was no longer a reliable reference. Consequently, after UV/O_3 treatment, the amide N 1s peak was used as a reference by relating its position to the dendrimer carbonyl C 1s peak obtained prior to UV/O_3 treatment. The amide N 1s peak was then used as a reference for all of the other XPS peaks after UV/O_3 treatment.

Prior to the UV/O_3 treatment, the XPS signal in the C 1s region can be deconvoluted into four peaks (Figure 5.6a). The peak at the lowest BE (285.2 eV) corresponds to the underlying PPF support.[51,112,146] The other three peaks arise from the presence of the dendrimer and are assigned to aliphatic carbons (cyan); the C-OH, C-N (amine), and C-N (amide) functionalities of the dendrimer (orange); and the carbonyl carbons of the dendrimer (blue), which is present at the highest BE (288.5 eV).[88,122,146]

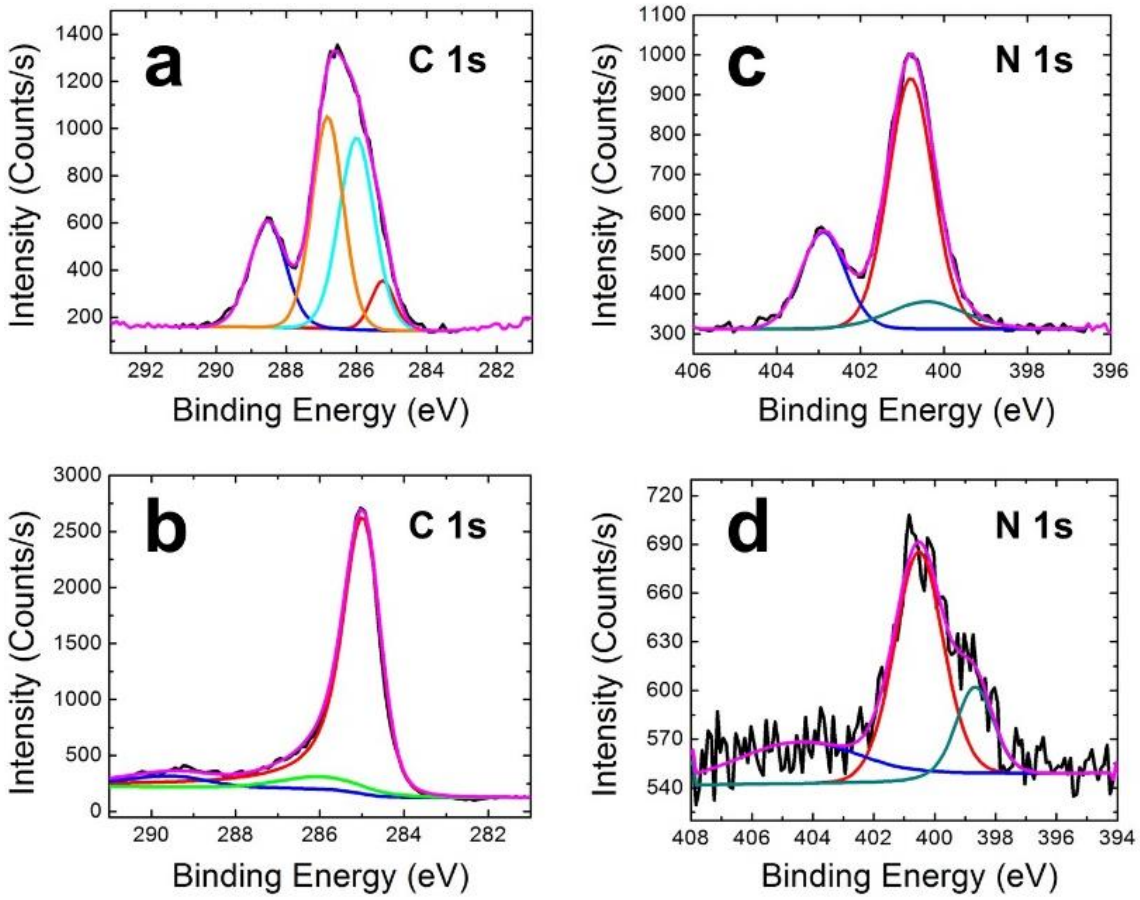

Figure 5.6: High-resolution XPS spectra in the C 1s and N 1s regions for a PPF/Al_2O_3/G6-OH(Pt_{55}) electrode before and after UV/O_3 treatment. The C 1s region (a) before and (b) after UV/O_3 treatment. The N 1s region (c) before and (d) after UV/O_3 treatment.

Following the UV/O_3 treatment (Figure 5.6b), the peak arising from the PPF support (BE = 285.2 eV) becomes dominant as most of the dendrimer is removed. The peak corresponding to the aliphatic carbons and the peak corresponding to the hydroxyl, amine, and amide functionalities associated with the dendrimers, are now all present as a single peak at 286.2 eV. The carbonyl peak is still observed at 289.7 eV, but at a much lower intensity relative to the background. A comparison of the dendrimer C 1s peaks before and after UV/O_3 treatment indicates that 88% of the overall dendrimer C 1s signal

is eliminated after UV/O_3. No peaks corresponding to phenolic or carboxylic carbons are present after UV/O_3. This is important, because in our previous work we showed that in the absence of the ALD layer these functionalities emerge.[146] Their absence here confirms that the Al_2O_3 ALD layer covers the PPF surface and protects it from oxidation during the UV/O_3 treatment.

In addition to C 1s, we also monitored the N 1s region to confirm decomposition of the dendrimer. Before the UV/O_3 treatment, the N 1s region consists of three peaks from lowest to the highest BE: unprotonated amines, amides, and protonated amines, respectively (Figure 5.6c).[88,122,146] After UV/O_3, the same N 1s peaks are observed, but at much lower intensities (Figure 5.6d). A comparison of the N 1s peak intensities before and after treatment reveals that 74% of the N 1s signal is decomposed after UV/O_3.

Effect of UV/O_3 Treatment on Pt DENs and Al_2O_3

In our earlier dendrimer decomposition study we observed that Pt DENs immobilized onto PPF substrates were partially oxidized after the UV/O_3 treatment.[146] It was possible, however, to electrochemically reduce the surface of the oxidized Pt DENs back to zero-valent Pt. Neither UV/O_3-treatment nor electrochemical reduction of PtO_x affected the size or shape of the NPs.[146]

Results similar to those in our previous studies were also observed when oxide-coated electrodes, PPF/Al_2O_3/G6-OH(Pt_{55}), were exposed to UV/O_3. Before UV/O_3, the Pt 4f region (Figure 5.7a) can be deconvoluted into two peaks, present at 72.6 eV and 76.0 eV, and these are assigned as metallic Pt.[15,122] A smaller third peak (red) in this region at 74.1 eV corresponds to Al 2p, and it arises from the presence of the Al_2O_3 support.[88] Following UV/O_3, the Al 2p peak is still present, but partial oxidation of the

PtNPs is now apparent. Specifically, the peaks at 73.1 eV and 76.7 eV correspond to $Pt(OH)_2$, while peak at 79.5 eV can be assigned to PtO_2 (Figure 5.7b).[88] Comparing the percentages of the metallic Pt peak intensities before and after treatment, we conclude that ~24% of the Pt is oxidized by UV/O_3. However, XPS also indicates that PtO_x formed as a consequence of UV/O_3 treatment can be reduced back to metallic Pt by scanning the potential of the $PPF/Al_2O_3/G6\text{-}OH(Pt_{55})$ electrode 50 times between -0.65 V and 0.63 V at a scan rate of 0.060 V/s in a 0.10 M $HClO_4$ solution previously saturated with Ar (Figure 5.7c). This is evidenced by the absence of PtO_x peaks at 73.1 eV, 76.7 eV and 79.5 eV after electrochemical reduction.

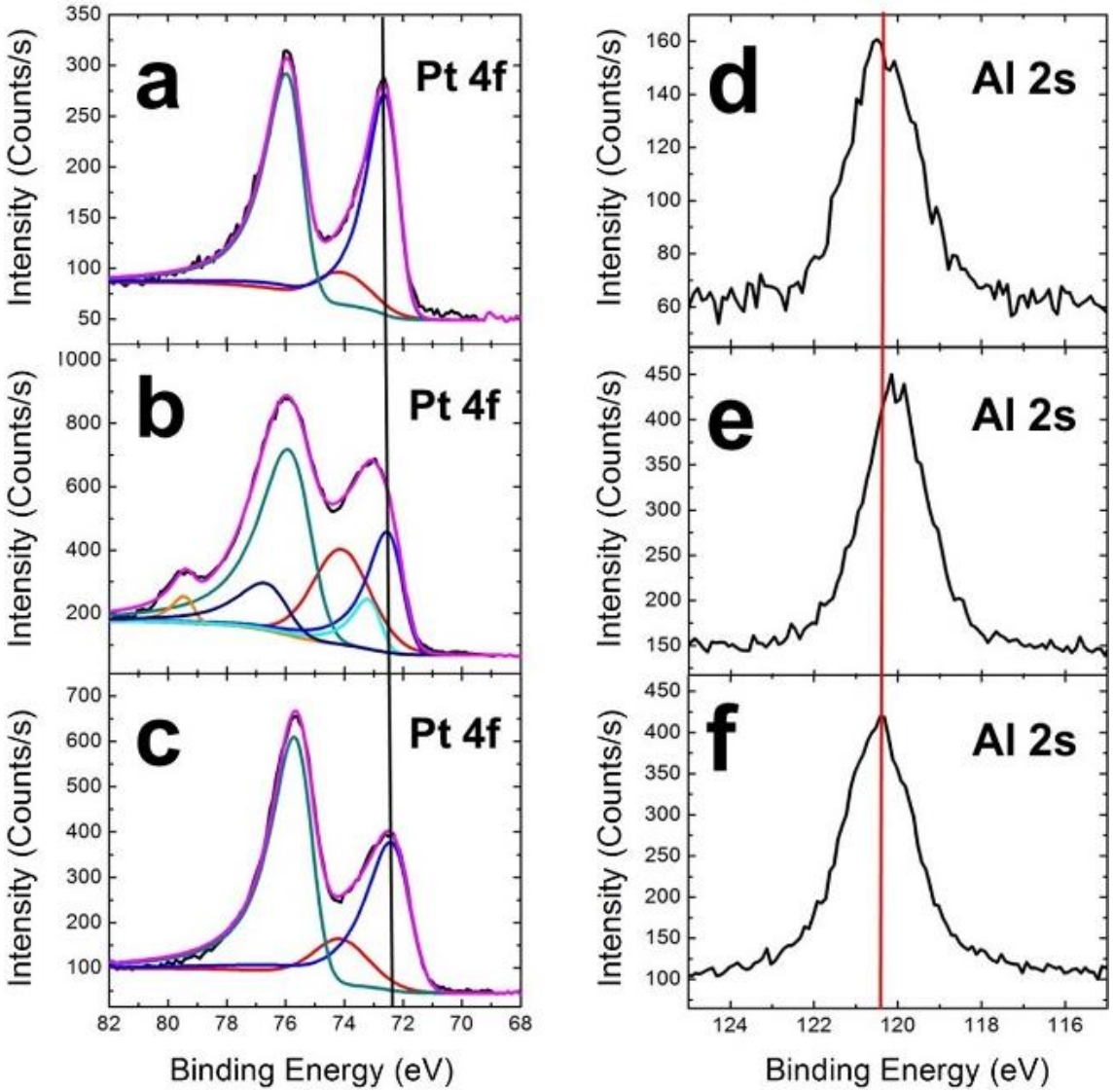

Figure 5.7: High-resolution XPS spectra in the Pt 4f and Al 2s regions for a PPF/Al_2O_3/G6-OH(Pt_{55}) electrode before and after UV/O_3 treatment. The Pt 4f region (a) before UV/O_3, (b) after UV/O_3, and (c) after UV/O_3 and electrochemical reduction of Pt. The Al 2s region (d) before UV/O_3, (e) after UV/O_3, and (f) after UV/O_3 and electrochemical reduction of Pt.

Interactions between Pt_{55} NPs (after the removal of the dendrimer by UV/O_3) and the underlying Al_2O_3 support can be monitored by tracking the positions of the Pt 4f and

Al 2s peaks.[7,126,139,141,180] The calibration method described in the previous section makes it possible to determine that the positions of the zero-valent Pt $4f_{7/2}$ peak before UV/O_3, after UV/O_3, and after subsequent electrochemical reduction, are all at 72.6 eV (vertical black line, Figures 5.7a-c). In a similar way, the positions of the Al 2s peak before and after UV/O_3, and after electrochemical reduction of PtO_x, were found to be at 120.4 eV, 120.1 eV, and 120.4 eV, respectively (Figure 5.7d-e, respectively). Taking into account the very small shift (0.3 eV) in the Al 2s peak position that occurs after UV/O_3 treatment and that is restored back to its original position (120.4 eV) following electrochemical reduction, as well as the fact that there is no change in the metallic Pt peak position, we conclude that there is very little (if any) electronic interaction between the Pt_{55} NPs and the Al_2O_3 support.[181]

As mentioned previously, the XPS data indicate that the Al_2O_3 ALD layer is not damaged by the UV/O_3 treatment (e.g., no indication of oxidation of the underlying PPF electrode), but for the ORR study discussed next it is also important that this be demonstrated in the flow cell under electrochemical conditions. Accordingly, an Al_2O_3-coated PPF electrode (no Pt DENs) was cycled between -0.50 V and 0.20 V at 0.060 V/s in an aqueous solution containing 1.0 mM $Fc(MeOH)_2$ and 0.10 M KNO_3. The observed currents (Figure 5.8) were very small, which is a consequence of the passivating oxide layer, and, more importantly, the differences in the magnitudes of the currents before and after UV/O_3 are likewise very small. On the basis of these electrochemical studies, and the previously discussed XPS results, we conclude that the UV/O_3 treatment is able to remove most of the dendrimer from the G6-OH(Pt_{55}) DENs, but that it leaves the Al_2O_3 layer intact.

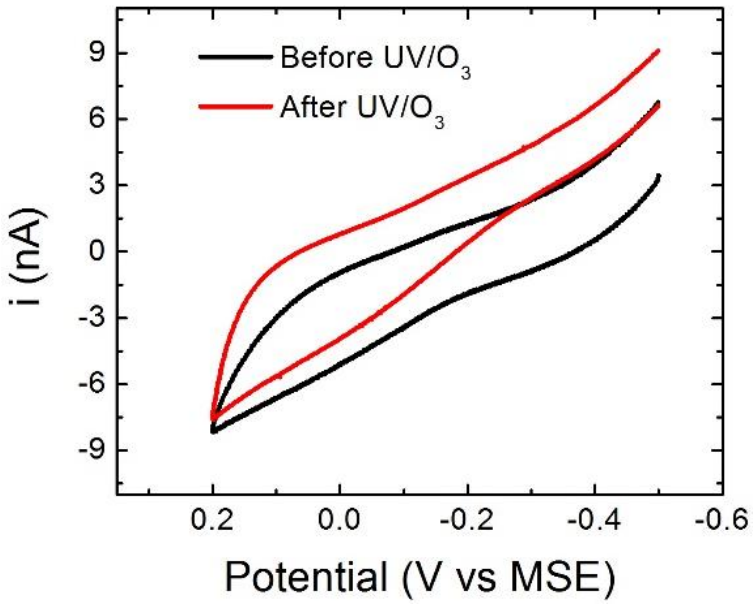

Figure 5.8: Cyclic voltammograms (CVs) of a PPF/Al_2O_3 electrode (a) before and (b) after UV/O_3 treatment. The electrode was scanned once from -0.50 V to 0.20 V and back to -0.50 V (scan rate = 0.060 V/s) in a flowing (50 µL/min) aqueous solution containing 1.0 mM $Fc(MeOH)_2$ and 0.10 M KNO_3.

Evaluation of the ORR Pathway in the Absence and Presence of Contact between PtNPs and the Al_2O_3 Support Using the Levich Equation

In acidic solution, the Pt-catalyzed ORR can occur by a four electron pathway to produce H_2O (Equation 5.4) or by a two electron pathway to produce H_2O_2 (Equation 5.5).[36,163] If the two-electron process occurs (Equation 5.5), the resulting H_2O_2 may undergo an additional two-electron reduction to yield H_2O (Equation 5.6). However, this second step is kinetically slow.[34,36,182] Nevertheless, depending on the experimental conditions, the ORR often follows a combination of these three pathways and, consequently, the effective number of electrons transferred (n_{eff}) is typically less than four.[36]

$$O_2 + 4H^+ + 4e^- \rightarrow 2H_2O \quad (5.4)$$

$$O_2 + 2H^+ + 2e^- \rightarrow H_2O_2 \quad (5.5)$$

$$H_2O_2 + 2H^+ + 2e^- \rightarrow 2H_2O \quad (5.6)$$

Having confirmed that the PPF/G6-OH(Pt_{55}) and PPF/Al_2O_3/G6-OH(Pt_{55}) model systems are both well-defined and robust, even after removal of the dendrimer, we now turn our attention to the electrochemical determination of the ORR pathway at the GE using the flow cell. Prior to experiments the PtNPs were cleaned electrochemically as described in the previous section. The ORR experiments were carried out in an aqueous 0.10 M $HClO_4$ solution that was saturated with O_2 by purging the solution for 1.5 h. The data in Figure 5.8, which is a plot of i_{lim}^{GE} vs $V_F^{1/3}$ for different electrode modifications, were obtained by scanning the GE potential from 0.40 V to -0.65 V at 0.060 V/s and then determining i_{lim}^{GE}. The current for the naked PPF electrodes (orange) is negligible, but currents observed for the four electrodes modified with PtNPs (PPF/G6-OH(Pt_{55}), PPF/Pt_{55}, PPF/Al_2O_3/G6-OH(Pt_{55}), and PPF/Al_2O_3/Pt_{55}) were higher due to the catalytic activity of the PtNPs. Moreover, the values of i_{lim}^{GE} for each of these four electrodes overlap with each other across the entire range of V_F. This result is in agreement with our previous finding that the presence of an ultrathin Al_2O_3 layer does not hinder the ORR kinetics for G6-OH(Pt_{55})-modified electrodes.[112] Likewise, the presence of the dendrimer layer does not affect the ORR kinetics. This observation is expected, because we[112] and others[32–35,143] have previously shown that electron transfer can be very fast between an electrode and metallic nanoparticles separated by up to a few nanometers by an insulator.

Next, we sought to compare the experimentally obtained values of i_{lim}^{GE} to theoretical Levich predictions (Equation 5.2) for the four- and two-electron ORR processes. Using previously reported values for the concentration of O_2 in 0.10 M $HClO_4$

(C = 1.26 mM)[183] and the diffusion coefficient of O_2 (D = 1.93 x 10^{-5} cm^2/s),[36,183] we calculated the currents for the two- and four-electron ORR pathways (Equation 5.2), and these are illustrated by the black and red lines, respectively, in Figure 5.9. The results of this analysis indicate that for all of the PtNP-modified electrodes n_{eff} = 3.3 ± 0.5. The value of n_{eff} observed here is in agreement with previously reported values obtained under similar mass-transport conditions ($k_t \leq 0.01$ cm/s).[163] The key result, however, is that neither the dendrimer nor the ultrathin Al_2O_3 layer affect the ORR pathway.

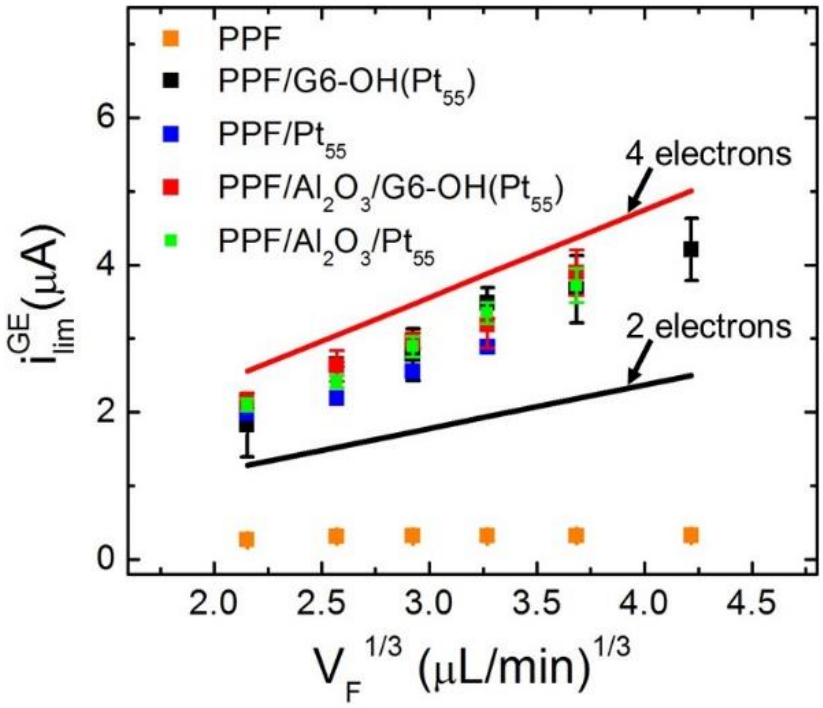

Figure 5.9: Plot of i_{lim}^{GE} vs $V_F^{1/3}$ for the indicated electrodes. The values of i_{lim}^{GE} were acquired by scanning (0.060 V/s) the GE from 0.40 to −0.65 V (vs MSE) in O_2-saturated 0.10 M $HClO_4$. The solid lines were calculated using the Levich equation (eq 2) for 2- and 4-electron pathways.

Evaluation of the ORR in the Absence and Presence of Contact between PtNPs and Al_2O_3 Support Using Generation-Collection

In the previous section, we showed that it is possible to evaluate the catalytic pathway by direct measurements at the GE. However, it has previously been observed that assignment of product distributions based only on the mass transport-limited current at a GE can be misleading.[163,184] Accordingly, we also used generation-collection to evaluate the ORR products. Specifically, the ORR was initiated at the GE, and if H_2O_2 is produced it can be detected via electrochemical oxidation at the CE. To implement this analysis, the values of i_{lim}^{GE} and i_{lim}^{CE} are determined, and then using the previously determined value of N (57 ± 10%), one can calculate n_{eff} using Equation 5.7.[163]

$$n_{eff} = 4 - \frac{2i_{lim}^{CE}}{Ni_{lim}^{GE}} \qquad (5.7)$$

We[163] and others[184,185] have shown that this approach is more accurate than relying solely on a Levich analysis, because only N and the limiting current ratios are required. For example, it is not necessary to possess an accurate value for the O_2 concentration to calculate n_{eff}, and the generation-collection approach is not affected by kinetic limitations that may occur at the GE.[163,184]

Generation-collection experiments were carried out in the flow cell using a solution containing 0.10 M $HClO_4$ and 1.26 mM O_2. The GE potential was scanned from 0.40 V to -0.65 V at 0.060 V/s, while holding the downstream CE at 0.70 V for the duration of the experiment. In agreement with previous reports,[92,163] and our own independent measurements (Figure 5.10), this CE potential is sufficiently positive to oxidize H_2O_2.

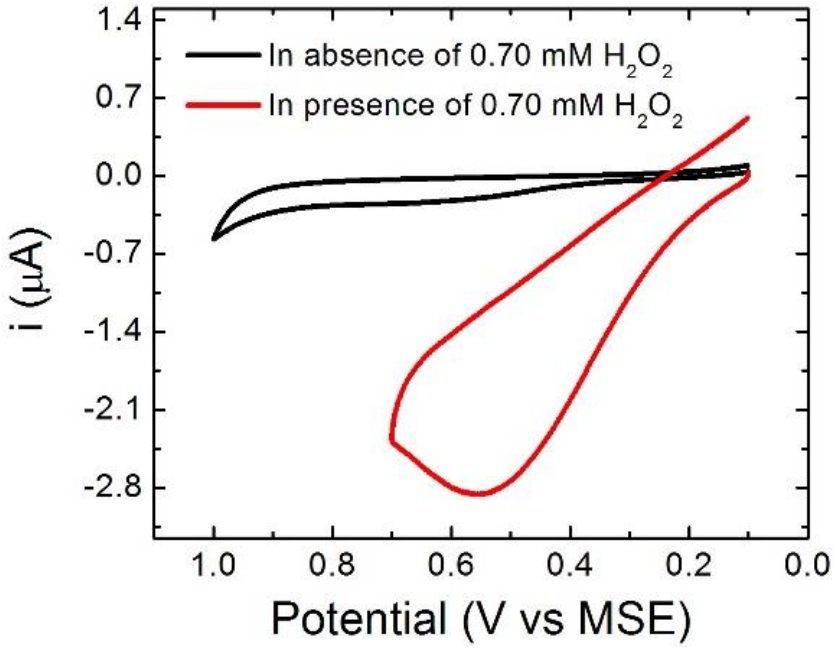

Figure 5.10: Diffusion-controlled oxidation of H_2O_2 at a platinized PPF electrode. CVs of a platinized PPF GE in an aqueous 0.10 M $HClO_4$ solution in absence and presence of 0.70 mM H_2O_2. The flow rate used was 5.0 μL/min and the scan rate was 0.060 V/s. The results show that a potential of 0.70 V is sufficient to oxidize H_2O_2 to O_2 at the mass transfer-limited rate. Accordingly, the CE was set to this potential for the generator-collector experiments described in the main text.

Figure 5.11 shows a representative linear sweep voltammogram (LSV) for the ORR at a PPF/Al_2O_3/Pt_{55} GE and the resulting, baseline-subtracted CE response. As the potential of the GE is scanned in the negative direction, the GE current becomes more positive due to the ORR until it reaches a plateau before decreasing at potentials more negative than -0.60 V. In contrast, the current at the CE, which results from oxidation of H_2O_2 produced at the GE, is lower and becomes more negative. The CE current does not plateau, but rather becomes more positive at negative potentials. This occurs because as the potential of the GE decreases below -0.40 V, some H_2O_2 produced by the two-

electron pathway (Equation 5.5) is reduced to water at the GE (Equation 5.6).[37] Hence, less H_2O_2 is available for oxidation at the CE. The absolute value of i_{lim}^{CE} is less than i_{lim}^{GE} for two reasons. First, because $N = 57 \pm 10\%$, the maximum possible i_{lim}^{CE} can only be ~57% of i_{lim}^{GE}. Second, both H_2O and H_2O_2 are possible products at the GE, but only the H_2O_2 fraction is detected at the CE.

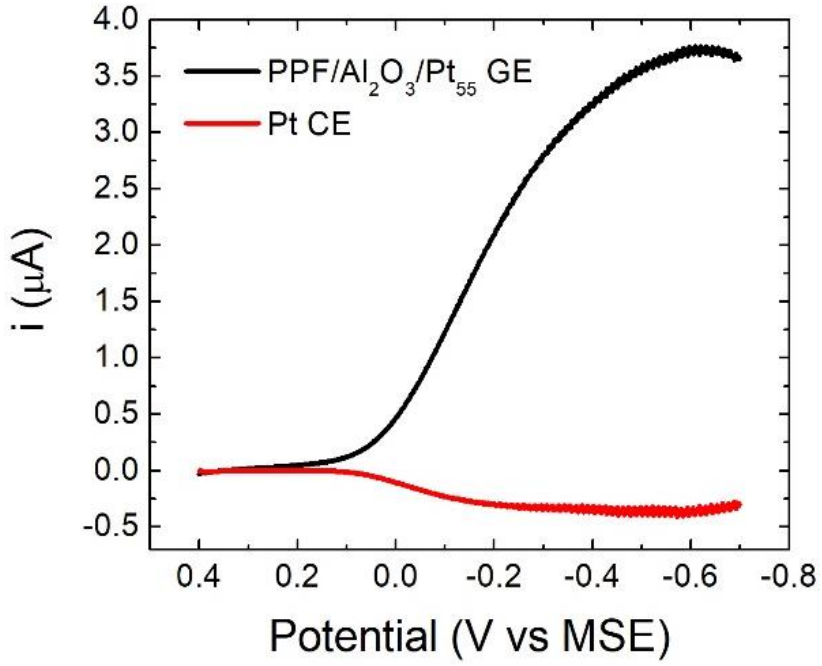

Figure 5.11: LSVs obtained using a PPF/Al_2O_3/Pt_{55} GE and a Pt CE. The GE was scanned from 0.40 to −0.65 V at a scan rate of 0.060 V/s (vs MSE) in O_2-saturated, 0.10 M $HClO_4$ solution. The potential of the CE was held at 0.70 V. The flow rate (V_F) was 50 μL/min.

Using the ratio of the mass transfer-limited currents at the GE and CE, the previously determined value of N, and Equation 5.7, the value of n_{eff} can be determined.[163] Figure 5.12 is a plot correlating the values of n_{eff} to $V_F^{1/3}$ for the four indicated electrode modifications. At all but the lowest value of V_F, where diffusion plays

a significant role in mass transport, n_{eff} is nearly independent of the electrode composition. Specifically, the average n_{eff} for PPF/G6-OH(Pt_{55}) and PPF/Pt_{55} is 3.5 ± 0.1, while the average n_{eff} for PPF/Al_2O_3/G6-OH(Pt_{55}) and PPF/Al_2O_3/Pt_{55} is 3.4 ± 0.1. These results indicate that removal of the dendrimer from the PPF/G6-OH(Pt_{55}) and PPF/Al_2O_3/G6-OH(Pt_{55}) electrodes does not affect the ORR pathway.

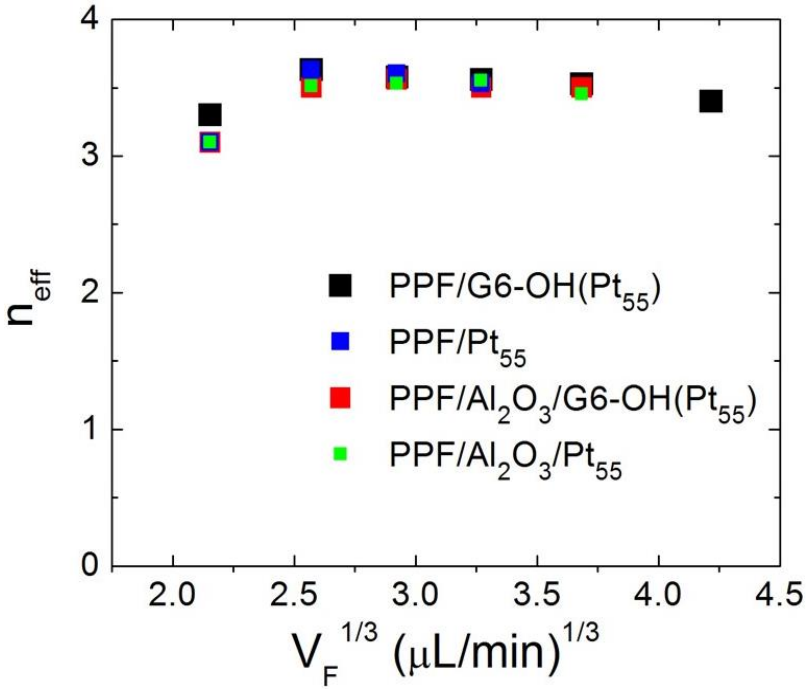

Figure 5.12 Plot showing the relationship between n_{eff} and $V_F^{1/3}$ for the indicated electrode modifications.

The average values of n_{eff} determined by direct electrochemistry at the GE (Levich equation, n_{eff} = 3.3 ± 0.5) and by generation-collection (n_{eff} = 3.45 ± 0.15) are, within experimental error, identical. However, the smaller error for generation-collection experiments indicates that this is a more precise method. In agreement with previous

reports, we conclude that generation-collection experiments are preferable to single-electrode experiments for studies of electrochemical reaction pathways.[92,163,175]

SUMMARY AND CONCLUSIONS

We have introduced a microelectrochemical flow cell that makes it possible to study complex surface modifications under conditions of hydrodynamic flow. The key advance is that the electrodes can be removed from the cell, modified, and then replaced without significantly changing flow characteristics. As shown here, this makes it possible to use electrodes modified by ALD or subjected to UV/O_3 treatment. The cell operating characteristics are well-defined, and both Levich and generation-collection experiments can be carried out.

There are three interesting scientific results that emerge from this study. First, we showed that it is possible to find UV/O_3 processing conditions that remove dendrimers from DENs but leave the encapsulated PtNPs intact. Likewise, this UV/O_3 treatment does not adversely affect the ultrathin Al_2O_3 layer. Second, we found that the reaction pathway for the ORR is not affected by the presence of the dendrimer or the ALD layer: n_{eff} = ~3.4, regardless of the electrode configuration. Third, direct contact between the Al_2O_3 layer and the PtNPs does not affect the reaction pathway for the ORR. Indeed, we anticipated this result and specifically chose the Pt/Al_2O_3 electrocatalyst model as a baseline system for future studies involving more interesting metals and metal oxides. These experiments are currently underway in our laboratory and the results will be reported in due course.

Chapter 6: Electrocatalytic Study of the Oxygen Reduction Reaction at AuNPs in the Absence and Presence of Interactions with SnO_x Supports[4]

INTRODUCTION

Strong metal-support interactions (SMSIs) are well known to strongly influence the catalytic properties of supported catalysts.[2,9,186,187] Since the term SMSI was first introduced in 1978,[42,188] extensive theoretical[189–194] and experimental[7,40,126,195–198] efforts have been directed towards understanding and more efficiently utilizing such interactions. Most experimental studies relating to SMSI have involved gas-phase heterogeneous catalysis, while only a few have been carried out using electrochemical systems. This is because most active supports are insulators (oxides and nitrides), and one does not usually think of using insulating electrodes for electrocatalysis. Nevertheless, there have been a few very clever electrochemical studies in which support effects have been shown to be important.

The Adzic group reported one of the first model catalyst systems designed to better understand the role of the metal/metal-oxide interface in electrocatalysis.[7,196,199,200] For example, they constructed an inverse catalyst by depositing SnO_2 nanoparticles (NPs) onto a Pt electrode and showed that it was more effective for the methanol oxidation reaction (MOR) than Pt alone.[201] More specifically, they showed that the degree of

[4] Ostojic, N.; Duan, Z.; Galyamova, A.; Henkelman, G.; Crooks, R. M. Elecrocatalytic Study of the Oxygen Reduction Reaction in the Absence and Preseence of Interactions with SnO_x Supports. Submitted to *JACS.*
I was first coauthor on this publication. A. Galyamova helped with data collection. Z. Duan performed simulations under the supervision of Dr. G. Henkelman. Dr. R. M. Crooks and Dr. G. Henkelman supervised the project.

effectiveness of the inverse electrocatalyst exhibited a strong dependence on the size of the SnO_2 NPs and hence the area of the Pt-SnO_2 interface. Theory suggested that the Pt-Sn electronic interactions, and the structural flexibility of smaller SnO_2 NPs, result in a weaker adsorption of OH species leading to more efficient oxidation of CO, a MOR intermediate that poisons Pt.

In addition to inverse catalysts, a few other systems have been used to study SMSIs for electrocatalytic reations.[126,195,198] For example, recently the Roziere group examined the beneficial effects of SnO_2 and doped-SnO_2 substrates on PtNP activity for the ORR.[202] In their experiments, Nb and Sb-doped SnO_2 tubes were prepared by electrospinning and subsequently modified with ~4 nm PtNPs. X-ray photoelectron spectroscopy (XPS) analysis indicated that the improvement in the electrocatalytic activity of the PtNPs was due to partial electron transfer from Sn to Pt.

On the basis of these and other studies,[126,195,196] it has been established that appropriate substrates can dramatically affect the properties of electrocatalytic NPs, and that these effects arise primarily from changes to either the electronic properties[126,202] or geometric structure[2,4] of the NPs. However, there is still very little understanding of how these and other effects conspire to improve electrocatalytic reaction rates or specificity.[203] Accordingly, it is, at present, not possible to *a priori* methodically tune the properties of metal NPs using support effects to achieve better electrocatalytic performance.

To address this challenge, we recently reported well-defined experimental models for studying the effects of SMSIs on electrocatalytic reactions (Scheme 1).[112,204] These models are based, in part, on NP-mediated electron transfer (eT) recovery,[32,35,135,205] which permits electrochemical study of interactions between metal NPs and well-defined ultra-thin metal-oxide (MO) films. The metal NPs utilized in our studies are prepared by

a dendrimer encapsulation method we[206] and others have previously reported.[10,11,207,208] These dendrimer-encapsulated NPs (DENs) are small (~2 nm), nearly monodisperse in size, and catalytically active.[110,209] Such small NPs have two advantages. First, they are amenable to first-principles calculations, and, second, they are most likely to exhibit interesting and observable SMSI effects in catalysis.[2]

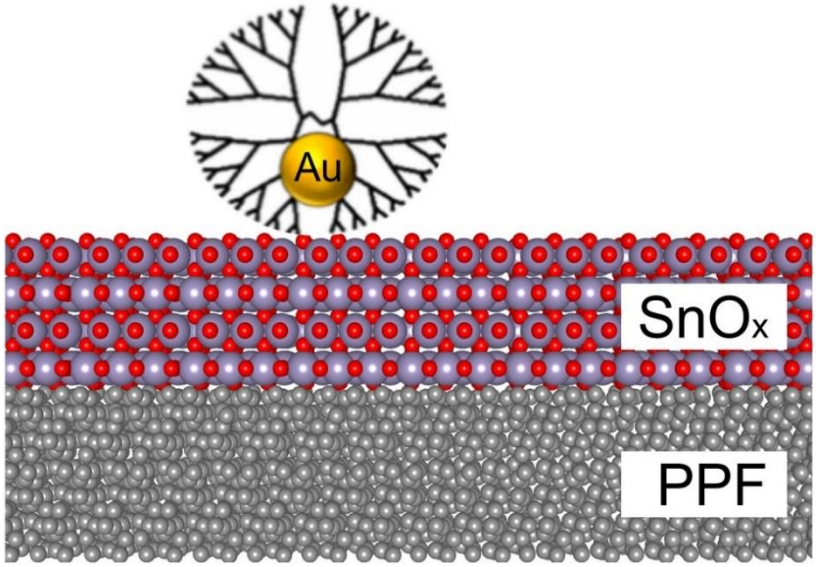

Illustration 6.1: Schematic representation of a PPF/SnO_x/G6-NH_2(Au_{147}) electrode.

We have previously shown that when DENs are immobilized onto MO supports prepared by atomic layer deposition (ALD),[25,27] the dendrimers prevent direct interactions between the encapsulated NPs and the MO supports.[204] However, we developed a UV/O_3-based procedure that removes the dendrimer scaffolds without measurably affecting the size, shape, or composition of the encapsulated NPs.[204] Accordingly, it is possible to study electrocatalysis using exactly the same electrode in

the absence and presence of direct interactions between the metal NPs and the MO supports.

We initially applied this experimental model system to what amounts to a control experiment.[204] Specifically, we examined the oxygen reduction reaction (ORR) at PtNPs in the absence and presence of interactions with an Al_2O_3 support. Alumina is not an active oxide in catalysis, and therefore we did not expect it to influence the ORR. Indeed, this is what was observed. Now we are moving into a new phase of research in which the oxide supports are specifically chosen to exhibit SMSIs and hence influence electrocatalytic reactions. Indeed, we now rely on theory to predict, in advance, combinations of metals and oxides that will yield superior performance. This interplay between theory and experiment is effective because the experimental model is nearly as well-defined as the theoretical constructs. Accordingly, there is a direct correlation between structure and function. This is important, because there are not too many examples in which first principles theory correctly predicts the function of a complex electrocatalyst.

In the present manuscript we consider the effect of two different supports ($SnO_{1.9}$ and $SnO_{2.0}$) and one type of metal NP (Au DENs containing an average of 147 atoms, Au_{147}) on the activity of the ORR. Compared to the case wherein the AuNPs are not in contact with the oxides, calculations predicted an overpotential reduction of ~0.30 V when the Au_{147} NPs directly interact with the SnO_x (x = 1.9 or 2.0) supports. The key finding of this article is that this prediction is borne out nearly quantitatively by companion experiments.

EXPERIMENTAL

Computational Methods

Spin-polarized DFT calculations were performed using the Vienna Ab initio Simulation Package.[210–212] The generalized gradient approximation with the Perdew−Wang (PW91) functional[213] was used to describe the exchange and correlation energy. Electron−ion interactions were treated by the projector augmented wave method.[214] In all calculations, the energy cutoff of the plane-wave basis set was 400 eV. The DFT+U method was applied to 4d orbitals of Sn ($4d^{10}5s^2$) to correct the on-site Coulomb interactions.[215] A value of U_{eff} = 3.5 eV was used to reproduce the electronic structure that has been observed experimentally.[216] Optimized structures were obtained by minimizing the forces on each ion until they fell below 0.05 eV/Å. A Bader analysis was employed to determine the local charge of atoms in the system.[217,218]

The lattice constants calculated in this work are set to a = 4.17 Å, for fcc Au, and a = 4.71 Å, c = 3.17 Å, for rutile SnO_2. AuNPs are modeled as cubo-octahedral Au_{147} and Au_{55}. We considered the SnO_2 (110) surface as it is the most stable surface of rutile SnO_2.[219] The SnO_2 (110) surface was modeled as a 6-layer slab with the top four layers fully relaxed, and the bottom two layers fixed in bulk positions. A vacuum gap of 15 Å was used to separate the slab from its periodic images. Supercells with a periodicity of (2 × 1) were employed to calculate adsorption and electrochemical reactions on the SnO_2 (110) surface. The Brillouin zone was sampled with a 4 × 4 × 1 Monkhorst-Pack k-point mesh.[220] For the hybrid Au/SnO_2 (110) system, we employed a SnO_2 (110) slab of three layers and a periodicity of (8 × 4) with the bottom atomic layer fixed in bulk positions. A hemispherical Au_{70} NP was placed on the surface of the SnO_2 slab. Due to the large

model employed, only the Γ point was used to sample the Brillouin zone. The atomic structures of these models are shown in Figure 6.1.

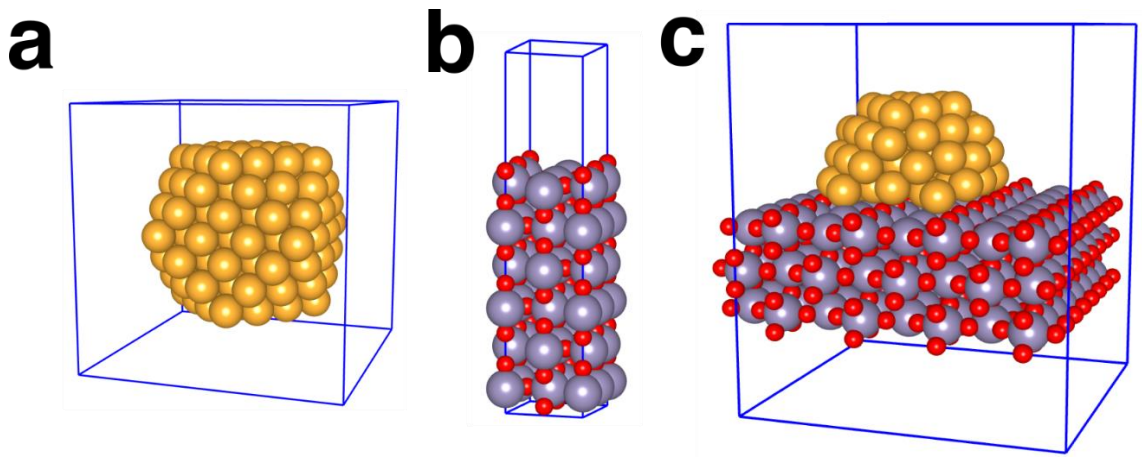

Figure 6.1: Atomic models employed in this work: (a) cubo-octahedral Au_{147} NP, (b) $SnO_2(110)$ slab, and (c) Au_{70} supported on $SnO_2(110)$ slab.

Thermochemistry of the electrochemical ORR was calculated by applying the computational hydrogen electrode method.[221] This method has previously proved successful in predicting ORR activity trends on transition metal surfaces[221] and oxide surfaces[222]. Briefly, the Gibbs free energy change of each electrochemical elementary step of the ORR was calculated with DFT. The ORR reaction mechanism was assumed to follow the four-step associative mechanism represented in Equations 6.1-6.4.

$$O_2(g) + H^+ + e^- + * \leftrightarrow OOH* \quad (6.1)$$

$$OOH* + H^+ + e^- \leftrightarrow O* + H_2O(l) \quad (6.2)$$

$$O* + H^+ + e^- \leftrightarrow OH* \quad (6.3)$$

$$OH* + H^+ + e_- \leftrightarrow H_2O(l) + * \quad (6.4)$$

The free energy change of each elementary steps can be calculated as $\Delta G = \Delta E - T\Delta S + \Delta ZPE$, where ΔZPE is the zero-point energy. The total energy changes (ΔE) of these elementary steps are the energy differences between DFT-calculated energies of reactant and product states. The chemical potential of the solvated proton and electron pair ($H^+ + e^-$) at standard conditions (pH=0, T=298.15 K) is calculated as $1/2G_{H2} + eU_{SHE}$ assuming equilibrium at the standard hydrogen electrode. The changes in ΔZPE and $T\Delta S$ are calculated using previously determined values.[221] Using the same computational hydrogen electrode method, it was also possible to calculate the surface free energies of formation of various SnO_2 (110) surfaces covered with different adsorbates and determine stable surfaces as a function of applied electrode potential at pH = 0 (surface Pourbaix diagram).[223]

Deposition of SnO_x (x = 1.7 or 2.0) Films onto PPF Electrodes

Oxide deposition was carried out using a Savannah S100 Cambridge NanoTech ALD system (Ultratech, San Jose, CA). TDMASn, heated to 60 °C, was used as the Sn source and H_2O was the oxygen source. The ALD system was evacuated to <1 mmHg, and a patterned PPF substrate was heated to 150 °C for 20 min under a constant flow (20 sccm) of high-purity N_2. Each ALD cycle was carried out as follows: (1) a single 0.015 s pulse of H_2O, (2) a 30.0 s purge with N_2, (3) a 0.50 s pulse of TDMASn, and (4) a 30.0 s purge with N_2. These four steps were repeated until the desired number of cycles had been achieved. This ALD procedure results in formation of $SnO_{1.7}$ films. These films were converted into the stoichiometric oxide ($SnO_{2.0}$) by heating to 150°C for 60 min under a constant flow of O_2 (150 sccm).

Surface Characterization

X-ray photoelectron spectroscopy (XPS) was carried out using a Kratos Axis Ultra spectrometer (Chestnut Ridge, NY) having an Al K_α source. Samples were grounded using Cu tape. Spectra were collected using a 0.10 eV step size and a band pass energy of 20 eV. An electron flood gun was used to neutralize charge. Binding energies (BE) were calibrated against the C 1s line of PPF (284.5 eV).[51,88] CasaXPS (version 2.3.15, Casa Software, Teignmouth, UK) was used for peak fitting and analysis. A mixed Gaussian/Lorentzian model was used for symmetric line-shapes, while an asymmetric Lorentzian model was applied for asymmetric line-shapes.

Ellipsometric measurements were performed using a J. A. Woollam M-2000D spectroscopic ellipsometer (Lincoln, NE). Data were collected using five different angles (between 44° and 66°) for each measurement. A three-part model was used for data analysis. The first slab was a 1.0 mm-thick layer of SiO_2 (optical constants provided by the manufacturer). The second slab was a 500 nm-thick layer of carbon (optical constants determined experimentally using a plasma-activated PPF thin film).[51] The third layer was SnO_2, and its optical constants were provided by the manufacturer. The thickness of the oxide layer was allowed to vary.

The surface roughness of the PPF and PPF/SnO_x (x = 1.7 or 2.0) thin films were obtained using a Wyko NT9100 optical profilometer having a white light source and yielding 0.1 nm vertical resolution.

Synthesis of DENs

Au DENs were synthesized using a previously published procedure[16,224]. Specifically, 200 μL of 100 μM G6-NH_2 dendrimer was added to 8.65 mL NERL water with vigorous stirring. Next, 147 μL of a 20.0 mM $HAuCl_4$ stock solution was added

dropwise. Within 2 min of adding the first drop of the $HAuCl_4$ solution, a ~67-fold molar excess of $NaBH_4$ (in 1.0 mL of 0.30 M NaOH) was added. The reaction mixture was stirred overnight to deactivate excess $NaBH_4$. The final concentration of this 10.0 mL Au_{147} DENs solution was 2.0 μM.

Immediately before immobilizing Au DENs onto the PPF/SnO_x electrodes, the pH of the Au_{147} DENs solution was adjusted to ~3.2 using an aqueous $HClO_4$ solution. Scanning transmission electron microscopy (STEM) indicated that Au_{147} DENs prepared in this way appeared spherical and had an average diameter of 1.8 ± 0.3 nm (Figure 6.2).

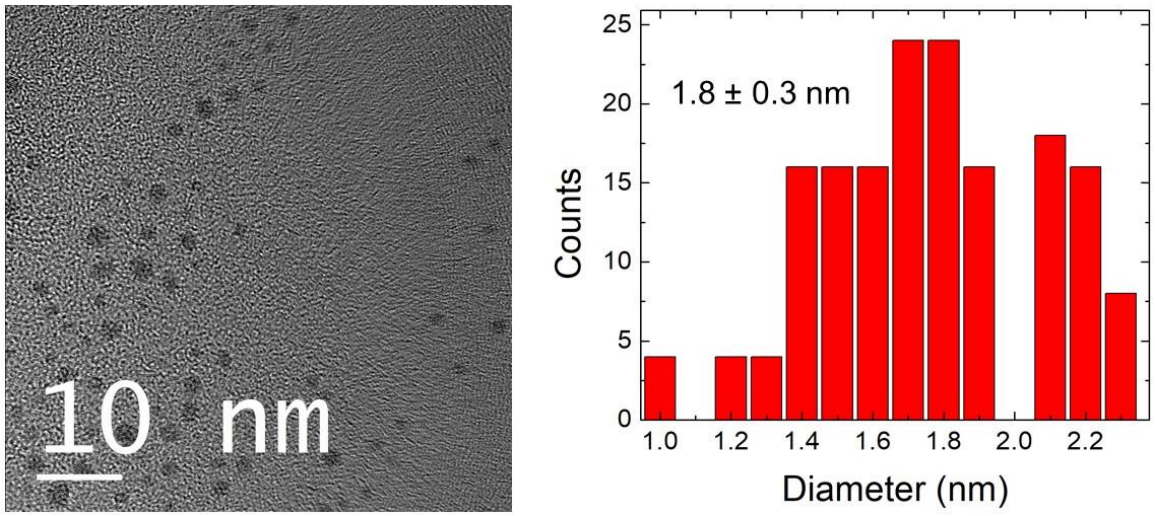

Figure 6.2: TEM micrograph and particle-size distribution histogram for G6-$NH_2(Au_{147})$ DENs prepared at pH ~3.2. The particle-size distribution is based on 150 randomly selected particles. The Au DENs have an average diameter of 1.8 ± 0.3 nm.

Au DENs were immobilized atop SnO_x-modified PPF electrodes by immersing the latter in the Au DENs solution (pH 3.2) for 2 h, after which the electrodes were rinsed under a gentle flow of NERL water and dried under low-pressure Ar. The newly formed

PPF/SnO_x/G6-NH_2(Au_{147})-modified electrodes were left to dry for at least 60 min prior to use.

UV/O_3 Method for Decomposition of G6-NH_2 Dendrimers

After surface modification, the PPF/SnO_x/G6-NH_2(Au_{147}) electrodes were placed in the center of the UV/O_3 chamber, the vacuum was turned on, and an external supply of O_2 was introduced into the chamber at 517.1 mmHg for 15 min. Next, the O_2 flow was stopped and the UV lamp was turned on for 5 min. After turning off the UV lamp, the chamber was purged with O_2 (517.1 mmHg) for 10 min. The last two steps were repeated five times. Next, the O_2 flow was stopped and the UV lamp was turned on for 5 min, and then the chamber was purged with O_2 for 15 min. The O_2 was turned off and the UV lamp was turned on for another 15 min. Finally, the UV lamp was turned off and the electrode was left inside the chamber for an additional 17 min.

Electrochemical Characterization

Electrochemical measurements were performed using a CH Instruments model CHI700D bipotentiostat (Austin, TX). For all electrochemical experiments, a Hg/Hg_2SO_4 reference electrode (MSE, CH Instruments) and a Pt wire counter electrode were used. Throughout this article, however, potentials were converted to the standard hydrogen electrode (SHE) to simplify comparison to the theoretical calculation. For static (non-flow) experiments, the electrochemical cell was fabricated from Teflon and used a Viton O-ring to define the area of the working electrode (12.4 mm^2). Prior to experiments, the Au DENs were electrochemically cleaned by scanning the potential between 0.45 and 1.55 V (vs. SHE) ten times in 0.10 M $HClO_4$ solution. Electrochemical measurements

were performed in aqueous solutions containing 1.0 mM $Fc(MeOH)_2$ and 0.10 M KNO_3 or 0.10 M $HClO_4$ purged with either Ar or O_2.

Some electrochemical experiments were carried out using a flow cell having a previously reported design and characteristics.[204] Measurements in the flow cell were carried out at several different flow rates. Between experiments at different flow rates 5 min was allotted for the system to stabilize.

RESULTS AND DISCUSSION

Characterization Surface Pourbaix Diagram of SnO_2(110)

Thermodynamically stable surface structures of SnO_2(110), as a function of applied potential, were found by calculating the relative stability of different adsorbate structures on the SnO_2(110) surface. The calculated free energies for many possible surface adsorbate structures on SnO_2(110) are plotted vs. potential at pH = 0 in Figure 6.3. Figure 6.3 shows that the most stable surface structure within the potential window of -0.25 V to 1.5 V is the water-dissociated SnO_2(110) surface that consists of adsorbed OH^- species atop Sn_{5c} ($Sn_{5c}OH^-$) and hydrogenated lattice bridging oxygen ($O_{bri}H^+$). The strong electrostatic interaction between $Sn_{5c}OH^-$ and $O_{bri}H^+$ makes the water-dissociated surface stable over a wide potential window. When the applied potential is lower than -0.25 V, the most stable surface is the hydrogenated SnO_2(110) surface.

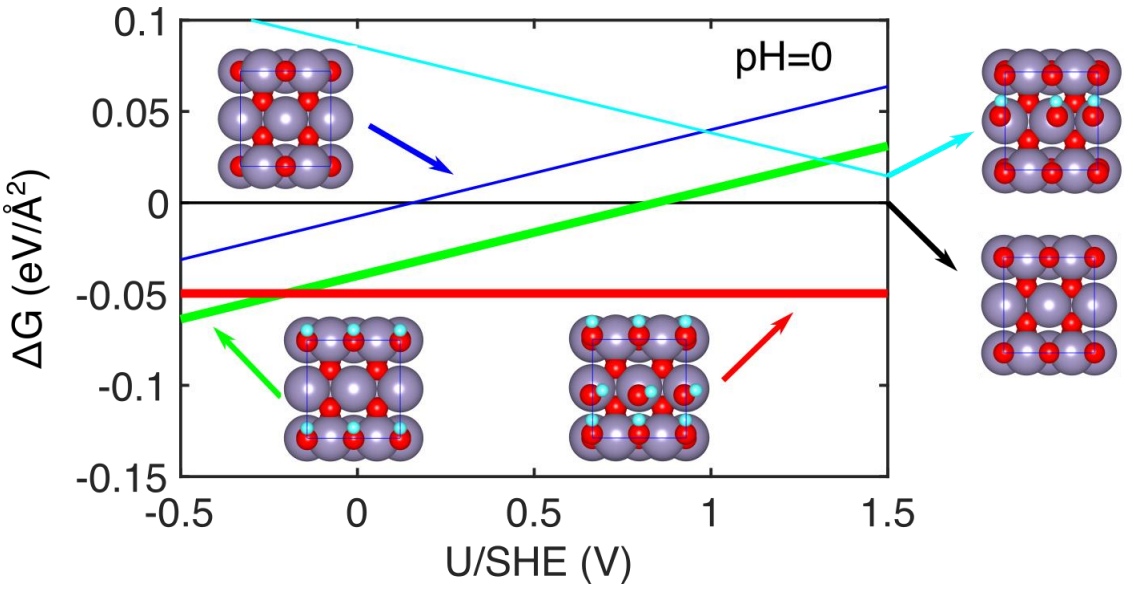

Figure 6.3: Stable adsorbate surface structures of SnO_2(110) as a function of applied potential at pH = 0. Black: clean SnO_2(110) surface, green: hydrogenated SnO_2(110) surface, red: water-dissociated SnO_2(110) surface, blue: SnO_2(110) surface with an oxygen vacancy, cyan: hydroxylated SnO_2(110) surface.

ORR Activity of SnO_2(110)

The Pourbaix diagram (Figure 6.3) indicates that the SnO_2(110) surface is inactive for the ORR under normal operating conditions because $Sn_{5c}OH^-$ cannot be reduced to yield water unless a potential below -0.25 V is applied. The inactivity of the SnO_2(110) surface is further illustrated by plotting the Gibbs free energy profile (FEP) along the ORR coordinate. The resulting FEP is shown in Figure 6.4a along with the adsorbate surface structures. The potential-determining step for the ORR on the hydrogenated SnO_2(110) surface is the reduction of OH* to water, which requires a calculated overpotential of ~1.3 V.

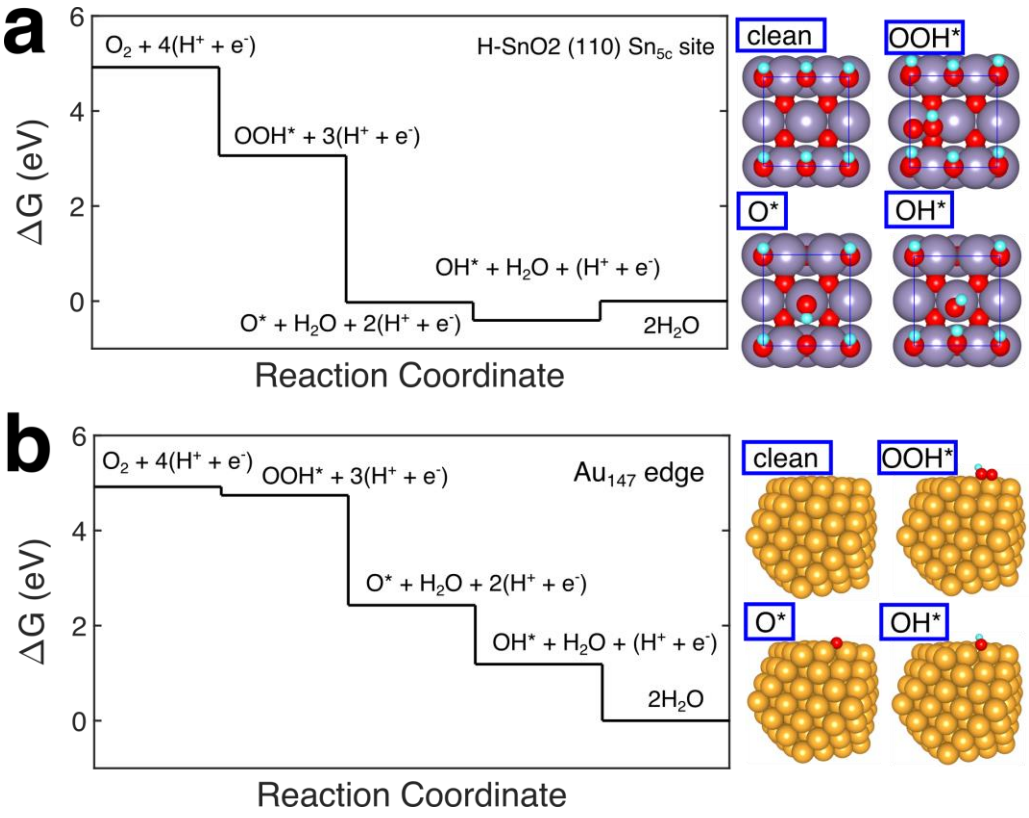

Figure 6.4: Free-energy diagram for oxygen reduction on (a) a hydrogenated $SnO_2(110)$ surface and (b) an edge site of cubo-octahedral Au_{147} NP at U = 0, pH = 0 and T = 298.15 K.

We also investigated the ORR activity of other $SnO_2(110)$ surface structures, including the stoichiometric $SnO_2(110)$ surface and the partially reduced $SnO_2(110)$ surface having oxygen vacancies (O_v). Although these surfaces are not thermodynamically stable according to the surface Pourbaix diagram, they could be kinetically stabilized. The FEP of the ORR on the stoichiometric $SnO_2(110)$ surface is shown in Figure 6.5a. The active site examined was the top site of Sn_{5c}. The atomic structures of various reaction intermediates adsorbed on $SnO_2(110)$ are shown alongside the FEP. The top site of Sn_{5c} requires a large overpotential (~1.3 V) for the ORR due to weak binding strengths of oxygenated species, especially OOH*. Hence, the

overpotential-determining step in this case is the first reduction of O_2 to form OOH*. We also examined the role of O_v for ORR catalysis. Figure 6.5b shows the FEP of ORR at the O_v site on SnO_2(110). The results indicate that the oxygenated species adsorbs too strongly on the O_v site, and once the O_v site is saturated with O*, the O_v site cannot be regenerated to complete the catalytic cycle.

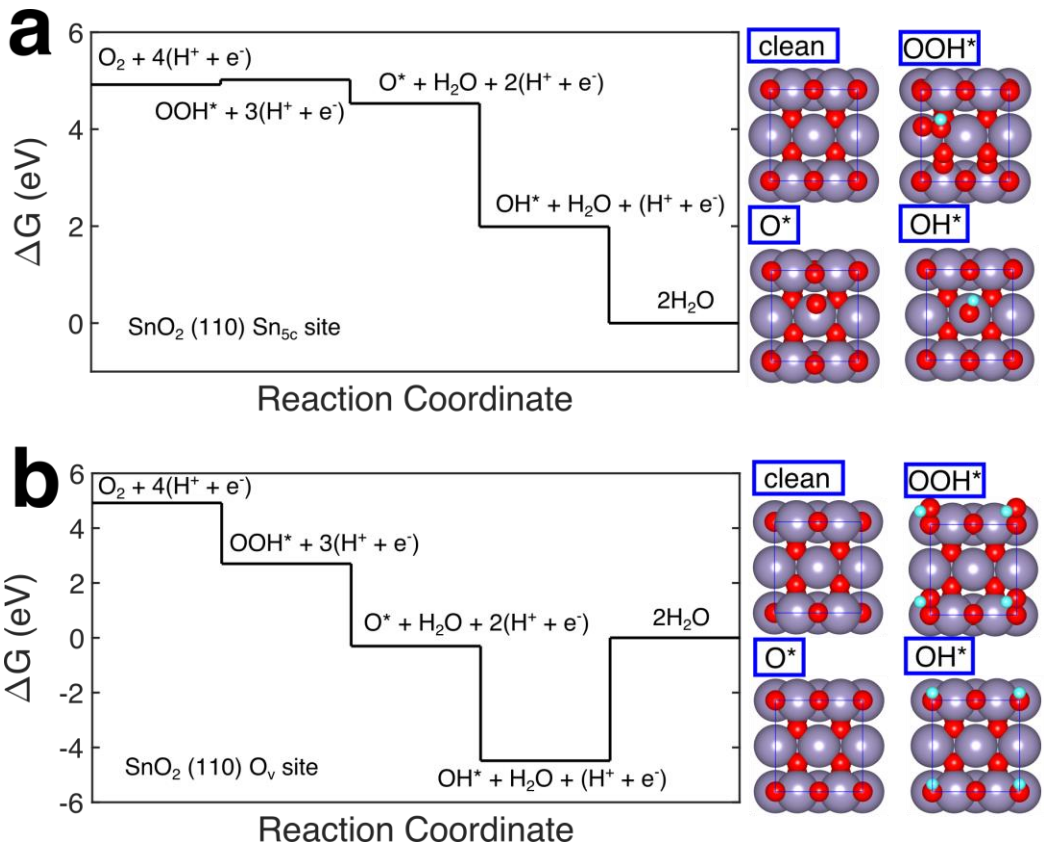

Figure 6.5: Free-energy diagram for the ORR on (a) a stochiometric SnO_2(110) surface and (b) an oxygen vacancy site on SnO_2(110) surface at U = 0, pH = 0 and T = 298.15 K.

ORR Activity of Au_{147}

Given the foregoing discussion of the ORR activity on the SnO_2(110) surface, we turn our attention to the ORR on Au_{147} NPs. For Au_{147}, the FEPs of the ORR were calculated on an edge site, and on (100) and (111) facet sites. The results for the edge site and the atomic structures of the adsorbed intermediates are shown in Figure 6.4b. The calculations indicate that the ORR on the Au_{147} edge site requires a theoretical overpotential of about 1.0 V, and that the potential-determining step is the formation of OOH*. The adsorption strengths of O* and OH* are very close to the ideal binding strength. Hence, one way to improve Au_{147} for ORR catalysis is to stabilize OOH* on Au_{147}. Finally, Figure 6.6 shows the results for the (111) and (100) facets. Compared to the previously discussed edge site, the (111) and (100) facets yield higher theoretical overpotentials due the more closely packed surfaces and correspondingly weaker adsorbate interactions.

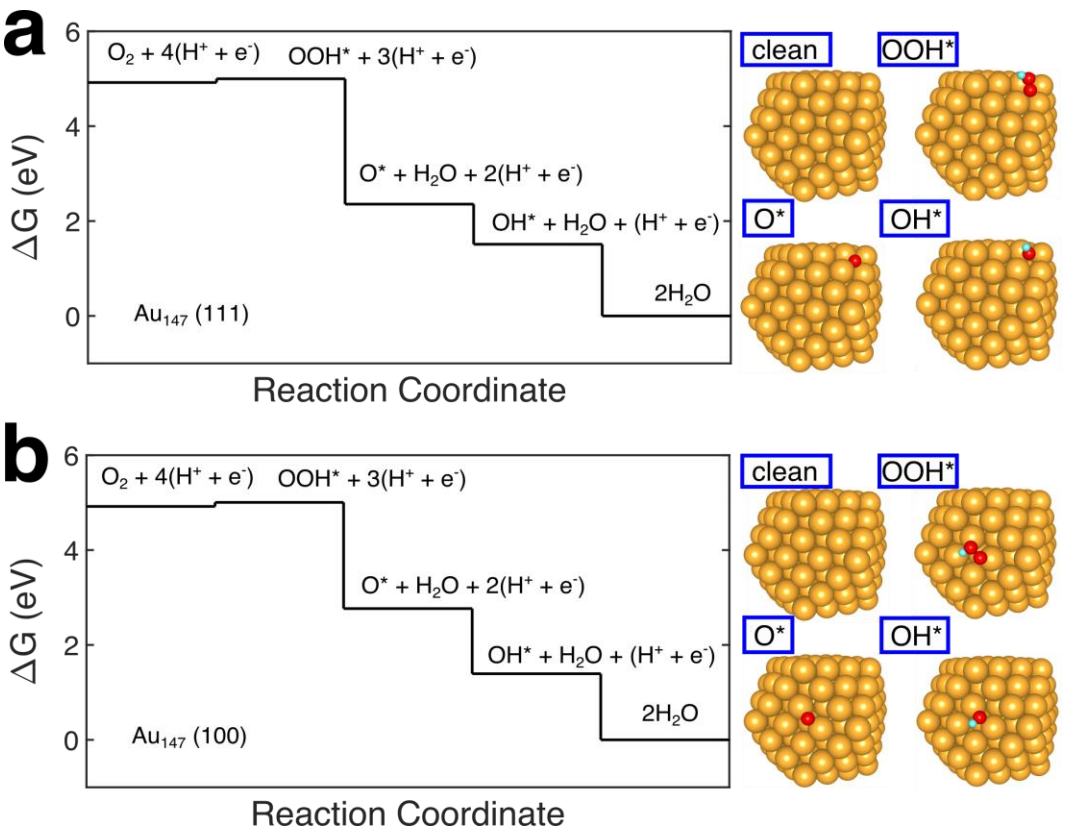

Figure 6.6: Free-energy diagram for the ORR on (a) a (111) facet and (b) a (100) facet of cubo-octahedral Au_{147} NP at U = 0, pH = 0 and T = 298.15 K.

ORR Activity of Au/SnO_2

Hybrid metal/oxide systems often exhibit synergistic effects that can lead to enhancement of catalytic activity. For example, we have previously demonstrated that interfacial adsorption sites exist that can enhance the O_2 adsorption strength on Au/TiO_2 as compared to the individual Au and TiO_2 components.[225,226] In these cases, the enhancement is due to the combined effects of charge transfer and redistribution at the Au/TiO_2 interface.[225] Because the Au_{147} catalyst suffers from weak adsorption of OOH*, which leads to a high predicted ORR overpotential, combining Au with SnO_2 is a possible strategy for increasing the OOH* binding strength.

For the foregoing reason, we investigated O_2 adsorption at the interface perimeter of Au/SnO_2 using a model we used previously for studying the Au/TiO_2 interface.[225] Several adsorption sites for O_2 were examined, and the adsorption surface structures and corresponding adsorption energies are shown in Figure 6.7. The results indicate that O_2 adsorbed at the Au/Sn_{5c}-Sn_{5c} site (Figure 6.7a) has an appreciable adsorption energy (-0.83 eV) which is close to the calculated adsorption energy on Pt of -0.75 eV. The calculated FEP for the ORR (Figure 6.8a) confirms the high ORR activity at this Au/Sn_{5c}-Sn_{5c} site. The predicted theoretical overpotential is 0.5 V, which is 0.7 V lower than the Au_{147} edge sites. This is a consequence of the increased OOH* adsorption strength. We note, however, that this calculation does not take into account the SnO_2 surface structure under typical ORR operating conditions. When the SnO_2 surface is hydrogenated, as predicted by the Pourbaix diagram (Figure 6.3), the interfacial Au/Sn_{5c}-Sn_{5c} site no longer possesses high ORR activity, because the strong interaction between $Sn_{5c}OH^-$ and $O_{bri}H^+$ leads to poisoning of the Sn_{5c} site (Figure 6.8b). The other interfacial sites involving Sn_{5c}, that is the Au-Sn_{5c} dual site and Sn_{5c}-Sn_{5c} site, suffer the same problem of strongly adsorbed OH^- atop Sn_{5c}. Therefore, our calculations exclude the interfacial sites as being active for the ORR.

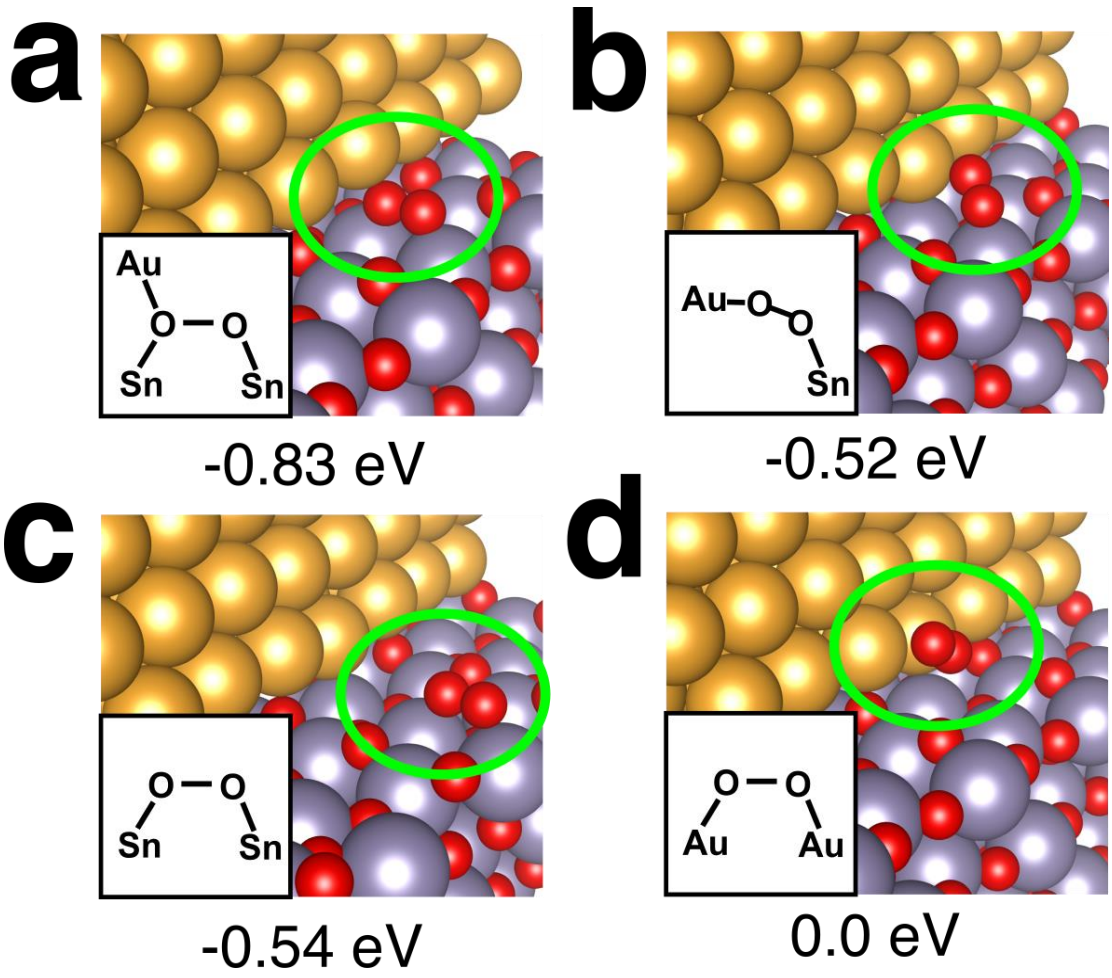

Figure 6.7: O_2 adsorption structures and binding energies at the perimeter of Au/SnO_2: (a) Au/Sn-Sn site, (b) dual Au-Sn site, (c) Sn-Sn site, and (d) Au-Au site.

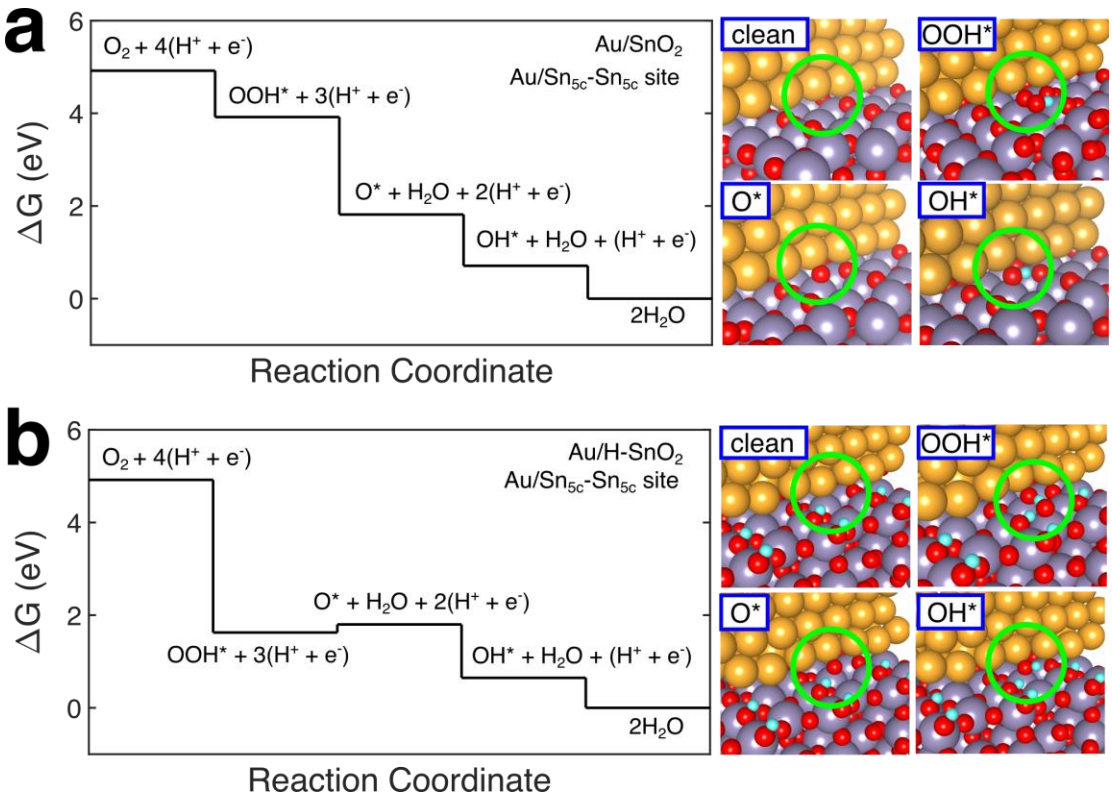

Figure 6.8: Free-energy diagrams for oxygen reduction on (a) Au/Sn_{5c}-Sn_{5c} site at the interface of the Au rod/stoichiometric SnO_2(110) model and (b) Au/Sn_{5c}-Sn_{5c} site at the interface of the Au rod/hydrogenated SnO_2(110) at U = 0, pH = 0 and T = 298.15 K. The atomic structures of active sites and intermediate adsorbates along the reaction coordinates are shown. "Clean" indicates the bare active site without adsorbates. "OOH*", "O*", and "OH*" are structures of adsorbates as indicated by the label. The color code is: yellow for Au, red for O, purple for Sn, and cyan for H.

The calculation represented by Figure 6.7d also indicates that SnO_2 does not promote O_2 adsorption on the AuNP, even considering Au sites near the Au/SnO_2 interface. This supported Au nano-rod model is designed to model the edge of a large (>3 nm) NP. Since the Au_{147} DENs are <2 nm in diameter, we also considered an isolated supported NP on the SnO_2(110) surface, which will better capture the different Au/SnO_2(110) boundary sites. As modeling an entire supported Au_{147} NP was too

computationally expensive, we have used a surrogate Au_{70} hemispherical model and placed it on the water-dissociated $SnO_2(110)$ surface, which is most relevant under reaction conditions. The FEP of the ORR on the edge of Au_{70} supported on $SnO_2(110)$ is shown in Figure 6.9a. The predicted theoretical overpotential is close to that on the edge of unsupported Au_{147}; the limitation of both systems is the same - the lack of binding sites with sufficient adsorption energy for oxygen species, including OOH*.

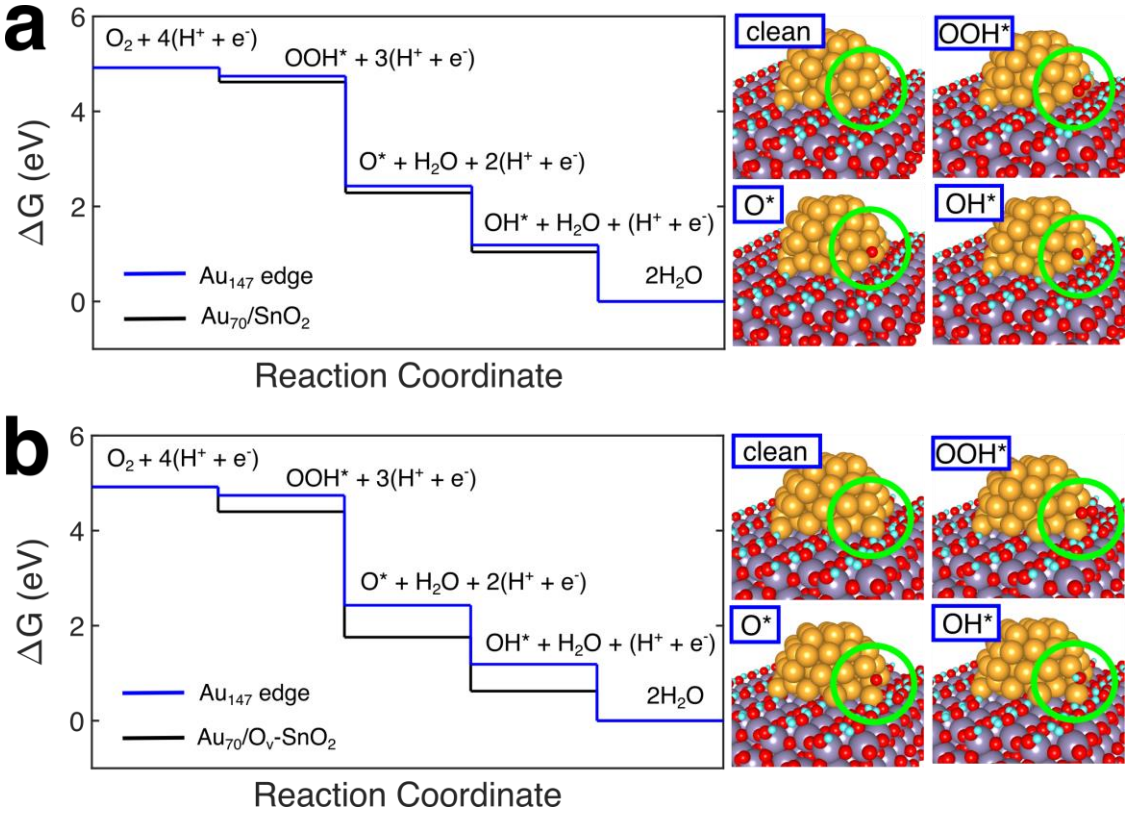

Figure 6.9: Free-energy diagrams for the ORR on (a) an Au edge site of Au_{70}/water-dissociated $SnO_2(110)$ and (b) anionic Au site of Au_{70}/water-dissociated O_v-$SnO_2(110)$ at U = 0, pH = 0 and T = 298.15 K. The atomic structures of active sites and intermediate adsorbates along the reaction coordinates are shown. "Clean" indicates the bare active site without adsorbates. "OOH*", "O*", and "OH*" are structures of adsorbates as indicated by the label. The color code is: yellow for Au, red for O, purple for Sn, and cyan for H.

SnO_2 is a prototypical transparent conductor, exhibiting the seemingly contradictory properties of high metallic conductivity, due to massive structural non-stoichiometry, with nearly complete insulator-like transparency in the visible range. First-principles calculations confirm that O vacancies and Sn interstitials have low formation energies and strong mutual attraction, which explains why SnO_2 can be found in the off-stoichiometric form, SnO_{2-x}[227], as we also see in this study. Hence, we should expect an appreciable concentration of oxygen vacancies on the SnO_2(110) surface. Additionally, the supported AuNPs should prefer to reside on surface oxygen vacancies with stronger adsorption. To capture this effect in our Au_{70}/SnO_2 model, we introduced a surface O_v underneath an Au atom at the edge of the Au-rod model. After relaxation, the Au atom above O_v sinks into the O_v due to the strong interaction, and the Au atom is reduced to a negative charge of -0.38e, according to our Bader analysis. We further calculate the FEP of the ORR at this anionic Au site, as shown in Figure 2b. The calculated theoretical overpotential in this case is 0.7 V, which is decreased by 0.3 V as compared to that at the edge of Au_{147}. The enhancement is due to the stronger binding energy of OOH* at the anionic Au site above the surface O_v on SnO_2(110) as compared to OOH* binding on the metallic Au site in Au_{147}. Thus, our theoretical investigation predicts that by supporting AuNPs on SnO_2, the ORR activity will be significantly enhanced as compared to the unsupported AuNP.

Characterization Surface Properties and Stability of SnO_x (x = 1.7 and 2.0)

$SnO_{1.7}$ and $SnO_{2.0}$ ALD films were prepared following the detailed procedures outlined in the Experimental Section. For the purposes of our experiments, the critical characteristics of these films are that they have well-defined thicknesses, that they are

electrochemically passivating and stable under electrochemical conditions, and that they are uniform over macroscopic dimensions.

The thicknesses of the $SnO_{1.7}$ and $SnO_{2.0}$ films were measured using spectroscopic ellipsometry. The data revealed a linear growth rate of 0.078 ± 0.005 nm/cycle (Figure 6.10) for both materials.[25] This growth rate is consistent with that reported in literature for the deposition of SnO_2 at 150 °C onto PPF (0.078 ± 0.003 nm/cycle) and onto Si(100) (0.07 nm/cycle).[85]

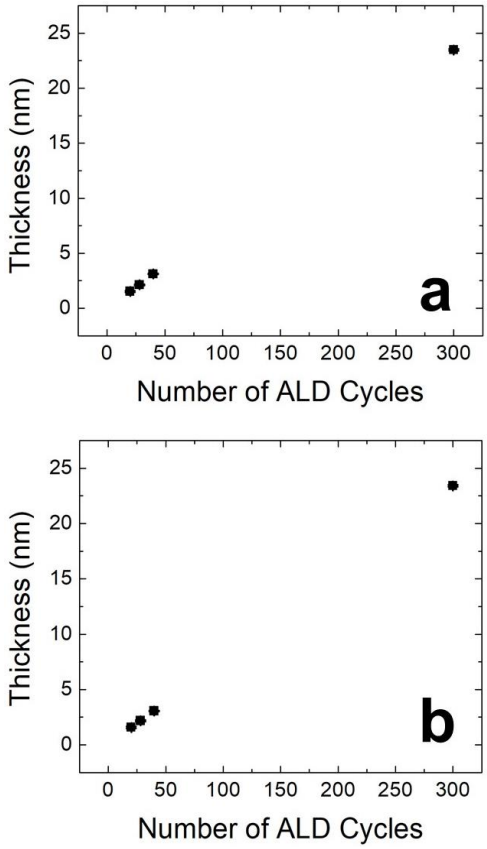

Figure 6.10: Plot of ellipsometric thicknesses as a function of the number of ALD cycles for (a) $SnO_{1.7}$ and (b) $SnO_{2.0}$ electrodes. The error bars (barely visible) represent standard deviation from the mean for three independently prepared films.

We found that a thickness of 2.2 nm (28 ALD cycles) was necessary for both $SnO_{1.7}$ and $SnO_{2.0}$ to completely passivate electron transfer (eT) between the underlying PPF electrode and solution-phase $Fc(MeOH)_2$. For example, Figure 6.11 compares cyclic voltammograms (CVs) of PPF, PPF/$SnO_{1.7}$, PPF/$SnO_{2.0}$, PPF/$SnO_{1.7}$/G6-NH_2(Au_{147}), and PPF/$SnO_{2.0}$/G6-NH_2(Au_{147}) electrodes in the presence of 1.0 mM $Fc(MeOH)_2$. The experimental conditions for immobilization of Au_{147} DENs onto PPF/SnO_x electrodes are discussed in the Experimental Section. Data in Figure 6.11a show that while well-defined oxidation and reduction peaks are observed for a naked PPF electrode (black), these peaks are absent when the same electrochemical scans are carried out with either the PPF/$SnO_{1.7}$ (red) or the PPF/$SnO_{2.0}$ (blue) electrode. This clearly indicates that 2.2 nm of either $SnO_{1.7}$ or $SnO_{2.0}$ is sufficient to completely passivate eT. However, the shapes of the CVs corresponding to PPF/$SnO_{1.7}$/G6-NH_2(Au_{147}) (magenta) and PPF/$SnO_{2.0}$/G6-NH_2(Au_{147}) (green) electrodes are very similar to that of a PPF (black) electrode (Figure 6.11b). This finding indicate that electroactivity is completely reactivated in the presence of Au_{147} DENs.[32,35,112,228]

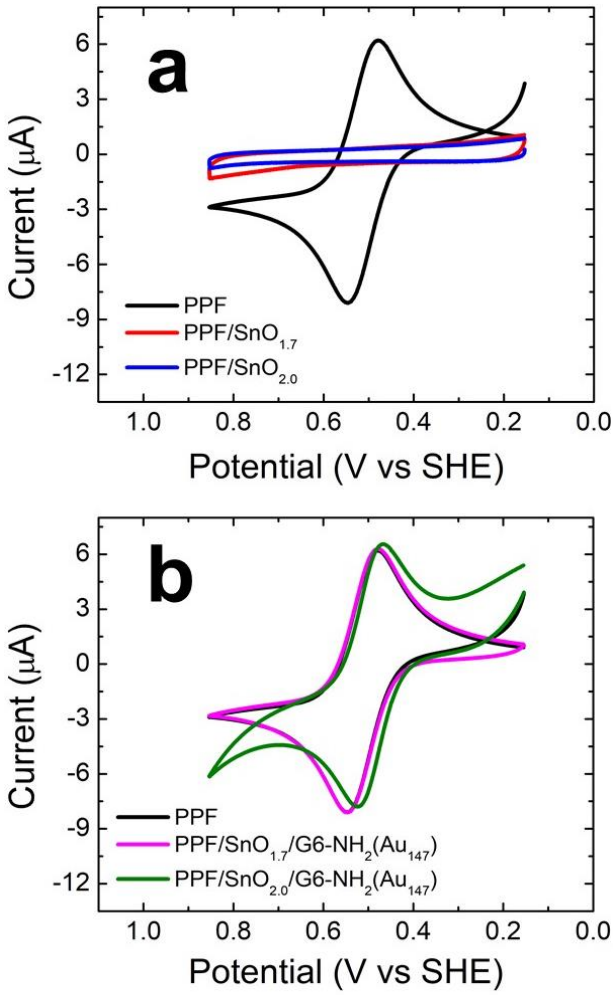

Figure 6.11: CVs obtained at the electrode modifications shown in the figure. The solutions contained aqueous 1.0 mM $Fc(MeOH)_2$ and 0.10 M KNO_3. The scan rate was 0.010 V/s. The geometric area of each electrode was 12.4 mm^2.

We next evaluated the stability of the PPF/SnO_x films under the electrochemical conditions used in our experiments. The Au_{147} DENs were immobilized onto the SnO_x modified PPF electrodes at pH ~3.2, and the ORR experiments were carried out in 0.10 M $HClO_4$ solution. Therefore, to determine the stability of the ALD-modified electrodes under acidic conditions, the PPF/$SnO_{1.7}$ and PPF/$SnO_{2.0}$ electrodes were immersed in 0.10

M $HClO_4$ solution for 2.0 h. Figure 6.12 shows CVs of $Fc(MeOH)_2$ for the PPF/SnO_x electrodes before and after this acid treatment. Changes to the CVs are small and indicate that the ALD films are rather stable under the tested acidic conditions.

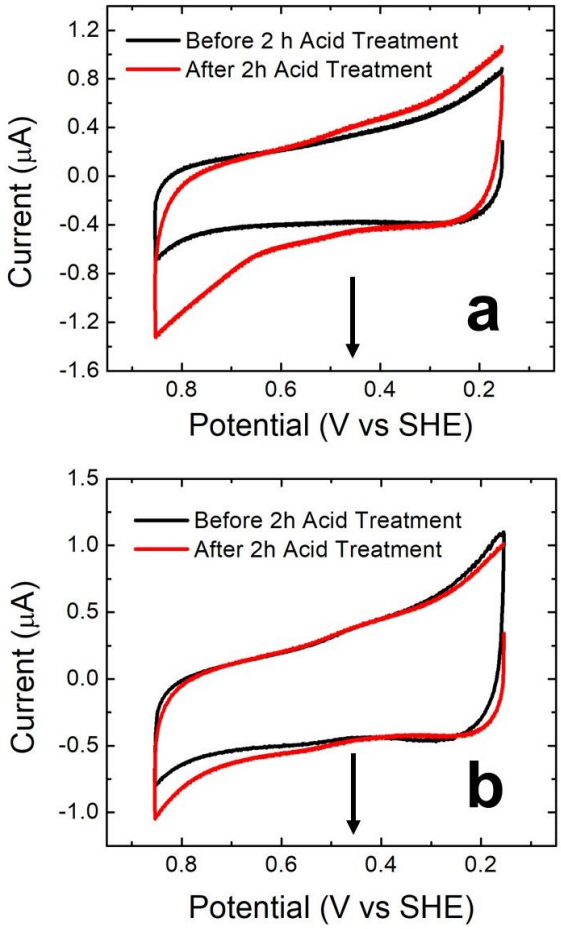

Figure 6.12: Results of a stability test of SnO_x thin films. CVs for (a) PPF/$SnO_{1.7}$ and (b) PPF/$SnO_{2.0}$ electrodes before (black) and after (red) a 2 h exposure to 0.10 M $HClO_4$. The CVs were obtained in an aqueous solutions containing 1.0 mM $Fc(MeOH)_2$ and 0.10 M KNO_3. The scan rate was 0.01 V/s. The before and after CVs were obtained using different electrodes, and this likely accounts for the difference between the pairs of CVs. The arrows indicate the approximate position of the standard reduction potential (E^0) for the redox couple (Fc/Fc^+). The important point is that no electrochemical activity is observed for the redox probe even after the acid treatment.

The surface roughness of SnO_x films was studied using optical profilometry, which revealed surfaces that are uniform and free of cracks. The average rms roughnesses of three independently prepared PPF electrodes coated with 2.2 nm-thick $SnO_{1.7}$ or $SnO_{2.0}$ determined over an area of 48 µm x 64 µm were ~0.63 ± 0.06 nm and ~0.68 ± 0.04 nm, respectively (Figure 6.13).

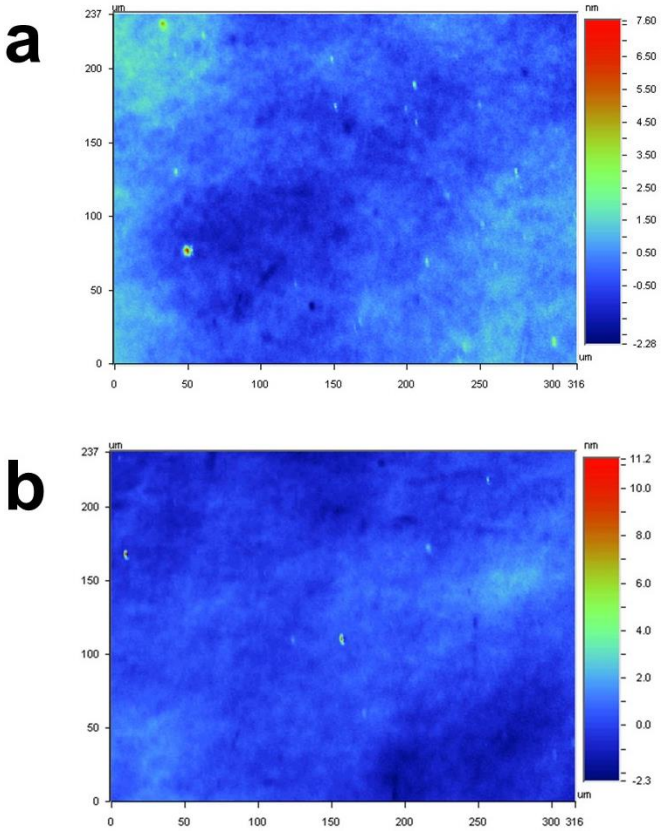

Figure 6.13: Optical profilometry of PPF electrodes modified with (a) 2.1 nm $SnO_{1.7}$ and (b) 2.1 nm $SnO_{2.0}$ films. The rms roughness of the PPF/$SnO_{1.7}$ and PPF/$SnO_{2.0}$ electrodes was ~0.63 nm ± 0.06 and ~0.68 nm ± 0.04, respectively (average of three independently prepared thin films).

As mentioned in the Experimental Section, ALD was used to prepare the $SnO_{1.7}$ films, and the $SnO_{2.0}$ films were prepared by oxidizing the as-prepared $SnO_{1.7}$ films at 150°C. XPS was used to determine the oxidation states of the two types of ALD films. Analysis of a tin oxide sample immediately after the ALD synthesis showed that the ratio of the atomic concentrations of Sn 3d:O 1s was 1.0:1.7 (Figure 6.14a,b and Table 6.1). A similar analysis was done with the ALD film following oxidation at 150°C. In this case, the results indicate that the Sn 3d:O 1s ratio increased to 1.0:2.0 (Figure 6.14c,d and Table 1).

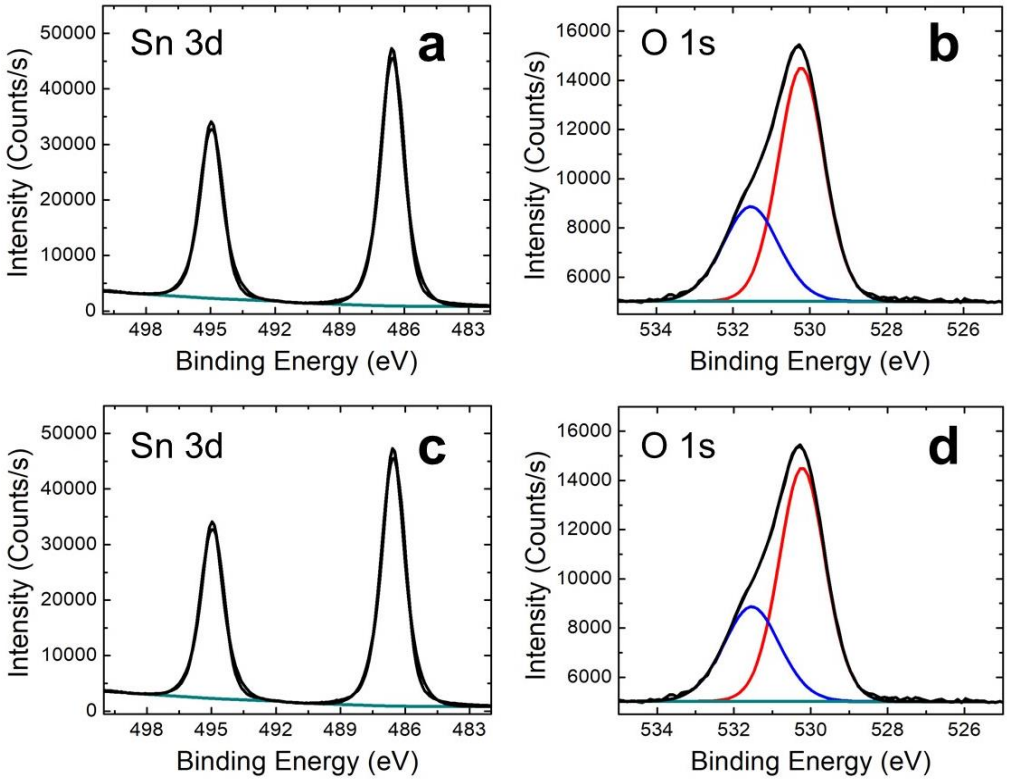

Figure 6.14: High-resolution XPS spectra in the Sn 3d and O 1s regions for (a), (b) a PPF/$SnO_{1.7}$ electrode and (c), (d) a PPF/$SnO_{2.0}$ electrode. All XPS peaks were referenced to the position of the PPF C 1s peak at 284.5 eV.[51,88]

	Atomic % Concentration Sn 3d	Atomic % Concentration O 1s	Sn 3d:O 1s
PPF/$SnO_{1.7}$	37.6	62.4	1.0:1.7
PPF/$SnO_{2.0}$	15.61	30.97	1.0:2.0

Table 6.1: Summary of XPS Sn 3d and O 1s atomic % concentrations and their ratios for PPF/$SnO_{1.7}$ and PPF/$SnO_{2.0}$ electrodes.

Decomposition of G6-NH_2 Dendrimers

In our previous studies, we showed that UV/O_3 can be used to nearly completely remove dendrimers from G6-OH(Pt_{55}) DENs immobilized onto naked PPF electrodes and PPF electrode modified with Al_2O_3.[146,204] In the present case, we switched from G6-OH to G6-NH_2 PAMAM dendrimers because the peripheral hydroxyl groups of G6-OH can prematurely reduce the Au^{3+}/G6-OH DEN precursor complex, resulting in polydisperse AuNPs.[16] This problem is avoided if G6-NH_2 dendrimers are used.[16,208]

Accordingly, we evaluated the extent to which the G6-NH_2 dendrimers are decomposed by UV/O_3 by examining the PPF/$SnO_{1.7}$/G6-NH_2(Au_{147}) interface before and after UV/O_3 treatment. The results indicate that there is a 93% decrease of the dendrimer C 1s signal (Figure 6.15a,b) and an 88% decrease in the dendrimer N 1s signal (Figure 6.15c,d). The XPS results further showed that the UV/O_3 treatment does not cause significant oxidation of Au_{147} NPs. Nonetheless, to ensure zero-valent Au after the UV/O_3, the electrodes were scanned 10 times between 0.45 V to 1.55 V in 0.10 M $HClO_4$ to remove any surface oxide that might be present.

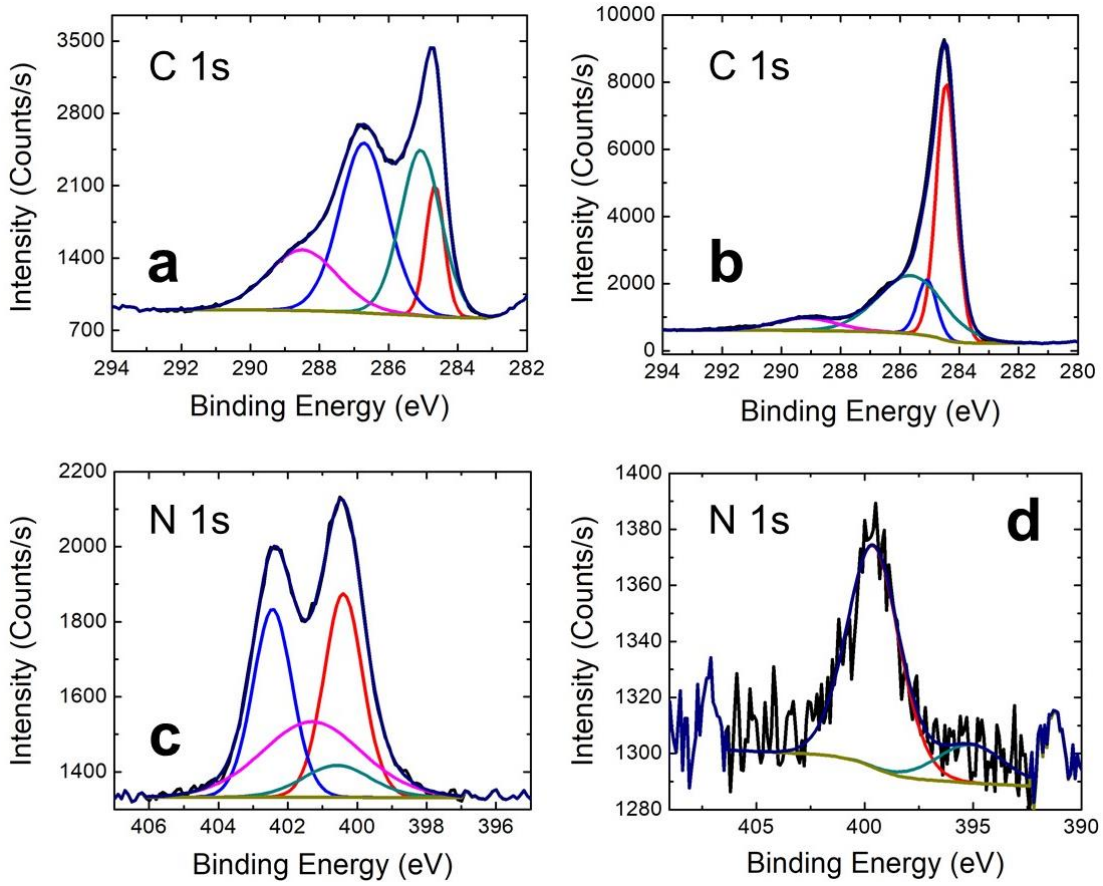

Figure 6.15: High-resolution XPS spectra in the C 1s and N 1s regions for a PPF/$SnO_{1.7}$/G6-NH_2(Au_{147}) electrode before and after UV/O_3 treatment. The C 1s region (a) before and (b) after the UV/O_3 treatment. The N 1s region (c) before and (d) after the UV/O_3 treatment. All XPS peaks were referenced to the position of the PPF C 1s peak at 284.5 eV.[51,88] A mixed Gaussian/Lorentzian model was used for symmetric line-shapes, while an asymmetric Lorentzian model was applied for asymmetric line-shapes. Following the UV/O_3 treatment, a 93% decrease of the dendrimer C 1s signal and an 88% decrease in the dendrimer N 1s signal were observed.

Effect of UV/O_3 Treatment on the Oxidation States of SnO_x (x = 1.7 and 2.0) Films

As mentioned in the previous section, the G6-NH_2 dendrimers are almost completely decomposed when exposed to UV/O_3, but we wondered if this treatment affects the oxidation state of SnO_x. Accordingly, we carried out a control experiment in

which PPF/SnO_x substrates (no immobilized DENs) were subjected to UV/O_3 and then analyzed using XPS. Figure 6.16 summarizes the results of this experiment. Following exposure of the PPF/$SnO_{1.7}$ electrode to UV/O_3, the Sn 3d:O 1s ratio is 1.0:1.9 (Figure 6.16a,b and Table 6.2). This means that after removal of the dendrimer the oxidation state of the support changes from $SnO_{1.7}$ to $SnO_{1.9}$. Accordingly, following exposure to UV/O_3, the PPF/$SnO_{1.7}$/G6-NH_2(Au_{147}) electrode is best represented as PPF/$SnO_{1.9}$/Au_{147} (Scheme 6.2a). This is a small change, but it is important to take it into account when comparing experimental results to theory.

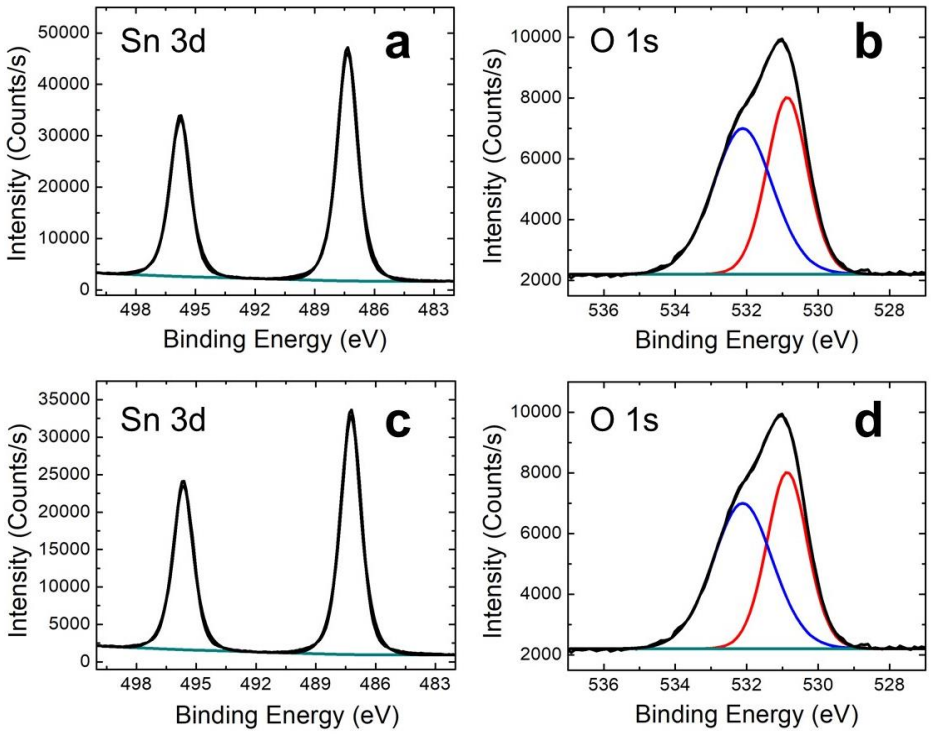

Figure 6.16: High-resolution XPS spectra in the Sn 3d and O 1s regions for (a), (b) PPF/$SnO_{1.7}$ and (c), (d) PPF/$SnO_{2.0}$ electrodes after the UV/O_3 treatment. All XPS peaks were referenced to the position of the PPF C 1s peak at 284.5 eV.[51,88]

	Atomic % Concentration Sn 3d	Atomic % Concentration O 1s	Sn 3d : O 1s
PPF/$SnO_{1.7}$ After UV/O_3 Treatment	34.8	65.2	1.0 : 1.9
PPF/$SnO_{2.0}$ After UV/O_3 Treatment	16.29	33.19	1.0 : 2.0

Table 6.2: Summary of XPS Sn 3d and O 1s atomic % concentrations and their ratios for PPF/$SnO_{1.7}$ and PPF/$SnO_{2.0}$ electrodes after the UV/O_3 treatment.

In contrast to the $SnO_{1.7}$ substrate, UV/O_3 treatment did not significantly affect the oxidation state of $SnO_{2.0}$ (Scheme 6.2b). That is, following UV/O_3 the Sn 3d:O 1s ratio remained 1.0:2.0 (Figure 6.16c,d and Table 6.2). These substrates are therefore referred to henceforth as PPF/$SnO_{2.0}$/G6-NH_2(Au_{147}) and PPF/$SnO_{2.0}$/Au_{147} before and after the exposure to UV/O_3, respectively, where the only difference is presence of the G6-NH_2 dendrimers.

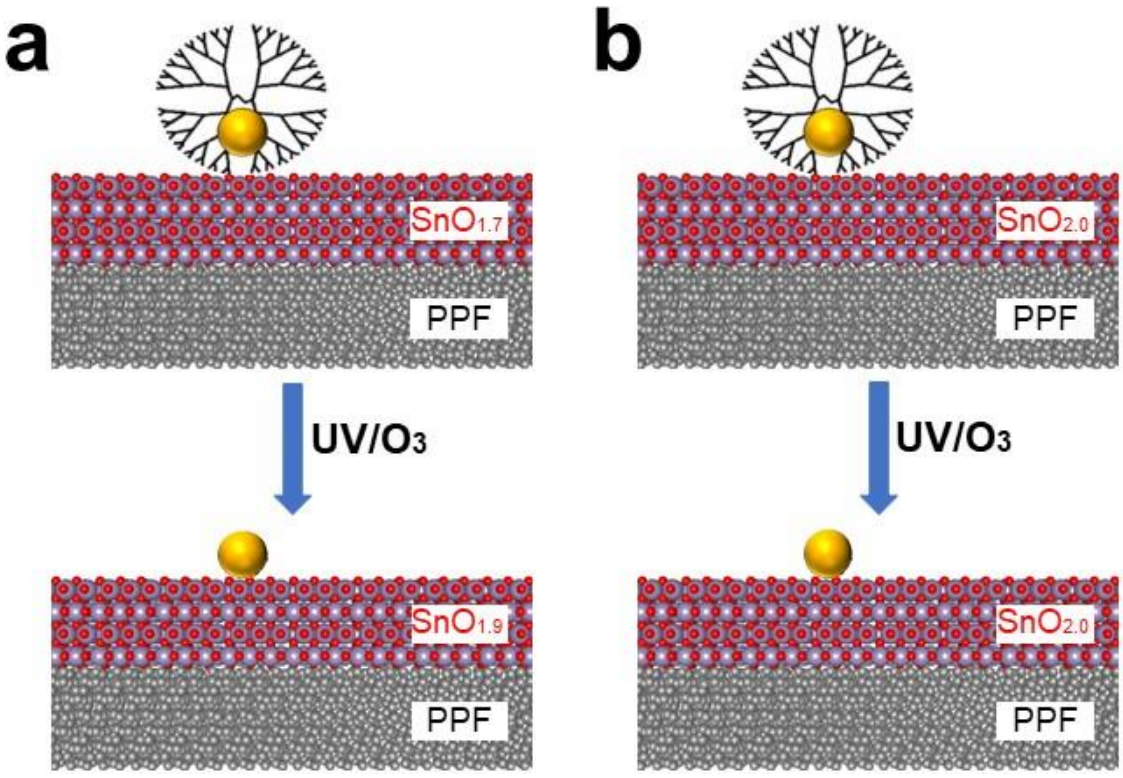

Illustration 6.2: Schematic representation of (a) PPF/$SnO_{1.7}$/G6-NH_2(Au_{147}) and (b) PPF/$SnO_{2.0}$/G6-NH_2(Au_{147}) electrodes before and after the UV/O_3 treatment.

Evaluation of the ORR Onset Potential and Kinetics in the Absence and Presence of Contact between AuNPs and SnO_x (x = 1.7, 1.9, and 2.0) Supports

In the previous sections we showed that dendrimers can be removed from encapsulated AuNPs, which means that it is possible to control whether or not the AuNP is in direct contact with the oxide surface (Scheme 6.2). Accordingly, we now focus on studying the ORR electrocatalyzed by Au_{147} NPs in the absence and presence of contact with $SnO_{1.9}$ and $SnO_{2.0}$ supports.

Prior to electrochemical measurements, the Au_{147} NPs were electrochemically cleaned as described in the Experimental Section. Figure 6.17 shows representative linear

sweep voltammograms (LSVs) for the ORR at PPF/$SnO_{1.7}$/G6-NH_2(Au_{147}) and PPF/$SnO_{2.0}$/G6-NH_2(Au_{147}) in the absence and presence of the interactions between AuNPs and the supports. These LSVs were obtained by scanning the GE electrode from 0.65 V to -0.45 V at 0.050 V/s while flowing O_2-saturated 0.10 M $HClO_4$ through the flow cell (described in the Experimental Section) at 10 μL/min. As mentioned earlier, removal of the dendrimers results in direct interactions between the Au_{147} NPs and the supports. When such direct interactions are introduced between Au_{147} NPs and the $SnO_{1.9}$ support, a 0.33 V positive shift in the onset potential (defined in the figure caption) for the ORR is observed. A shift of similar magnitude (0.28 V) is observed when dendrimers are removed from the PPF/$SnO_{2.0}$/G6-NH_2(Au_{147}) electrode. The observed improvements in the onset potentials following the removal of dendrimers for both $SnO_{2.0}$ and $Sn0_{1.9}$ are in near-quantitative agreement with the calculations discussed earlier, which indicated that after the removal of the dendrimers an onset potential reduction of ~0.3 V should be observed.

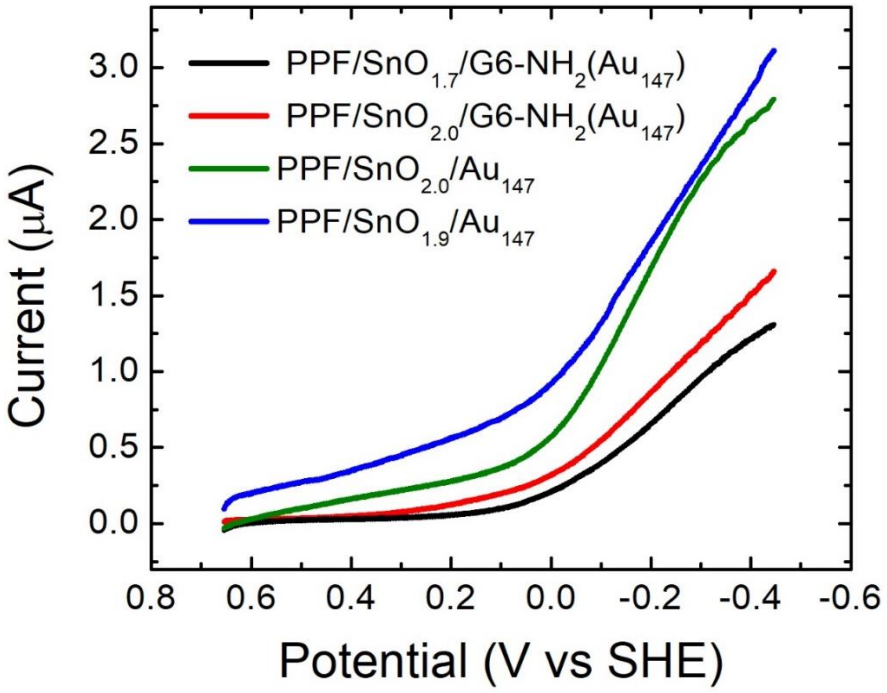

Figure 6.17: LSVs obtained using the indicated generator electrode (GE) modifications. The GE was scanned from 0.65 to −0.45 V (vs. SHE) at 0.050 V/s in O_2-saturated 0.10 M $HClO_4$. The flow rate (V_F) was 10 μL/min. The onset potential was defined as that potential corresponding to 10% of maximum current.

To evaluate the kinetics of the ORR, the experiments described in the previous paragraph were repeated, but this time the flow rate of the solution in the electrochemical flow cell was varied. Figure 6.18 is a plot of i^{GE} vs. $V_F^{1/3}$ for the indicated GE modifications. The value of i^{GE} is defined as current obtained at -0.45 V. The currents for the PPF/$SnO_{1.7}$ electrode are negligible, while just slightly higher currents are observed for the PPF/$SnO_{2.0}$ electrode. In contrast, significantly higher currents are observed in the presence of the DENs (Scheme 6.2). It is important to point out that the currents obtained for these two types of electrode modifications overlap with each other over the entire flow rate range, indicating that the observed ORR activity is due only to the presence of

Au_{147} DENs and that the underlying supports have little effect on the ORR. This is not surprising, because the presence of the dendrimer means the DENs are not in direct contact with the oxides. We further confirmed that the identity of the oxide is not important when the dendrimers are present by carrying out the same experiments using Al_2O_3 ALD supports.[204] Indeed, the ORR currents obtained using a PPF/Al_2O_3/G6-NH_2(Au_{147}) electrode (Figure 6.19) yielded results very similar to those obtained with the PPF/$SnO_{1.7}$/G6-NH_2(Au_{147}) and PPF/$SnO_{2.0}$/G6-NH_2(Au_{147}).

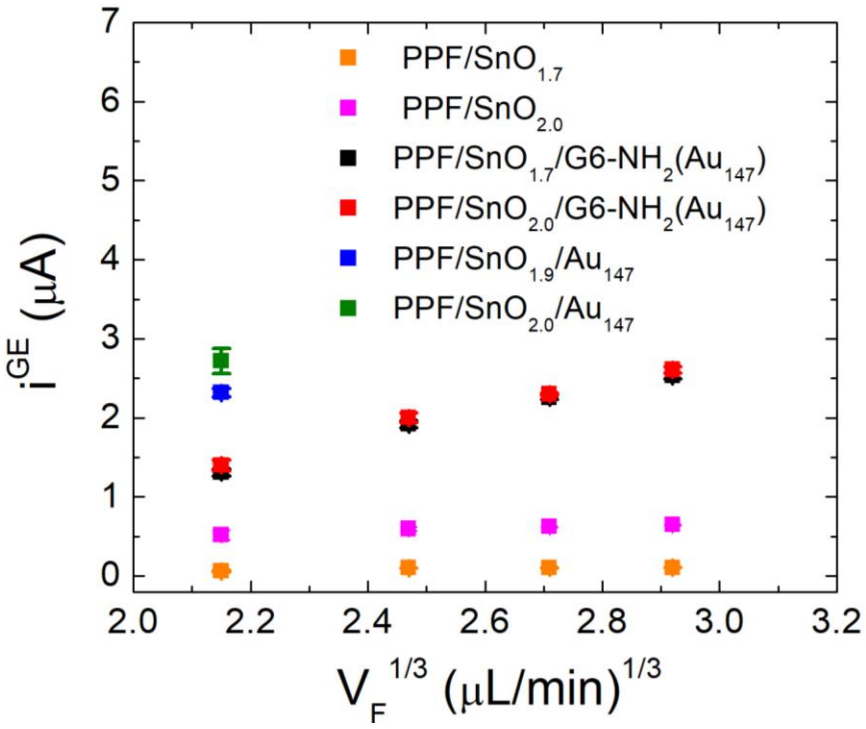

Figure 6.18: Plot showing the relationship between i^{GE} and $V_F^{1/3}$ for the indicated generator electrode (GE) modifications. The GE was scanned from 0.65 to −0.45 V (vs. SHE) at 0.050 V/s in O_2-saturated 0.10 M $HClO_4$. The potential of the collector electrode (CE) was held at 1.35 V. The error bars represent the standard deviations for three measurements that were carried out using independently prepared electrodes.

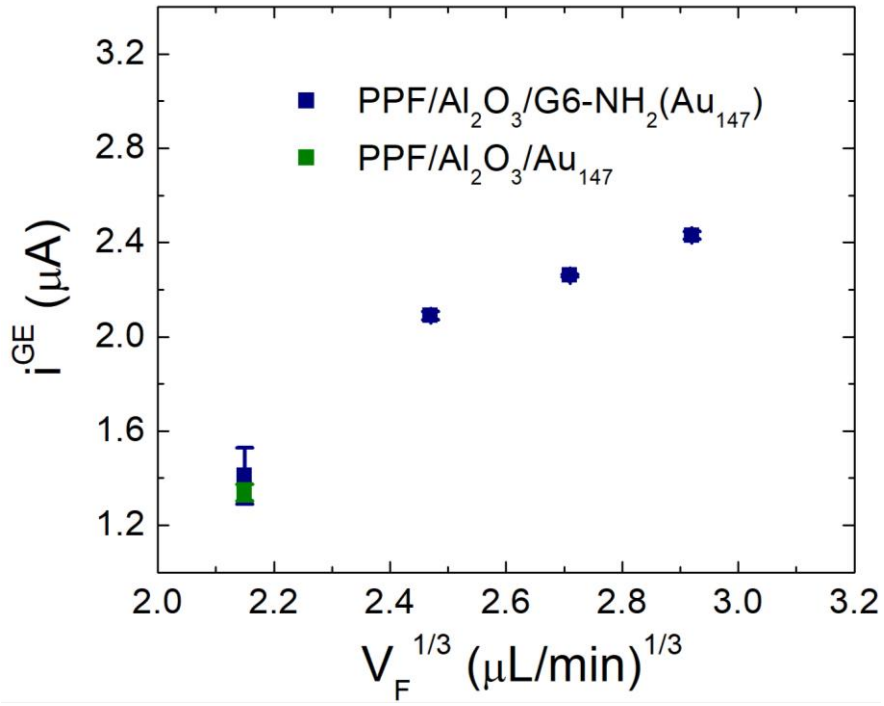

Figure 6.19: Plot showing the relationship between i^{GE} and $V_F^{1/3}$ for the PPF/Al_2O_3/G6-NH_2(Au_{147}) and PPF/Al_2O_3/Au_{147} electrodes. The generator electrode (GE) was scanned from 0.65 to −0.45 V (vs. SHE) at 0.050 V/s in O_2-saturated 0.10 M $HClO_4$. The error bars represent the standard deviations for three measurements that were carried out using independently prepared electrodes.

After removal of the dendrimers, further improvements in the ORR kinetics are observed for the both the PPF/$SnO_{1.9}$/Au_{147} and with PPF/$SnO_{2.0}$/Au_{147} electrodes. These increases are shown as the blue and green squares at $V_F^{1/3}$ = 2.15 in Figure 6.18. Unfortunately, these electrodes modifications were not stable at higher flow rates, indicating that the dendrimer provides a stabilizing scaffold for the encapsulated DENs at higher flow rates. Nevertheless, all the results shown in Figure 6.18 were highly reproducible (the almost negligible error bars in the figure result from at least three trials using independently prepared electrodes), indicating that the near doubling of the current

after removal of the dendrimers is real. To confirm that the increase in current results from support effects, we carried out the same experiment using an inert Al_2O_3 support. In this case, there was no change in current regardless of the presence or absence of the dendrimer (Figure 6.19).

Evaluation of the ORR Pathway in the Absence and Presence of Contact between AuNPs and SnO_x Supports

In this section we describe experiments intended to better understand how the $SnO_{1.9}$ and $SnO_{2.0}$ supports affect the ORR pathway on AuNP electrocatalysts. These experiments were carried out as follows using the flow cell in generation/collection mode. First, O_2-saturated 0.10 M $HClO_4$ was introduced into the electrochemical cell at four different flow rates (10, 15, 20, and 25 μL/min). Second, after the flow rate stabilized the ORR was initiated at the GE by scanning it from 0.65 V to -0.45. H_2O_2 produced at the GE during the ORR, was then detected at the CE via electrochemical oxidation. This was accomplished by holding the potential of the CE at 1.35 V.[204] The values of i^{GE} and i^{CE} obtained at -0.45 V, along with the previously determined value of collection efficiency (N = 57 ± 10%),[204] were used with Equation 5.7 to calculate n_{eff} involved in the ORR.

Figure 6.20 is a plot of n_{eff} vs. $V_F^{1/3}$ for the four electrode modifications indicated in the legend of the figure. Consistent with the previously discussed kinetic measurements, the values of n_{eff} nearly overlap for PPF/$SnO_{1.7}$/G6-NH_2(Au_{147}) and PPF/$SnO_{1.7}$/G6-NH_2(Au_{147}). However, when the dendrimer is removed and the AuNPs are in direct contact with the oxide, there is a dramatic reduction in the amount of peroxide generated. Specifically, n_{eff} increases from 2.1 ± 0.2 to 2.9 ± 0.1 for the PPF/$SnO_{1.7}$/G6-NH_2(Au_{147}) electrode and from 2.2 ± 0.1 to 3.1 ± 0.1 for the

PPF/$SnO_{2.0}$/G6-NH_2(Au_{147}) electrode. These results indicate that direct interactions between Au_{147} NPs and both supports, $SnO_{1.9}$ and $SnO_{2.0}$, have beneficial effects on the ORR pathway.

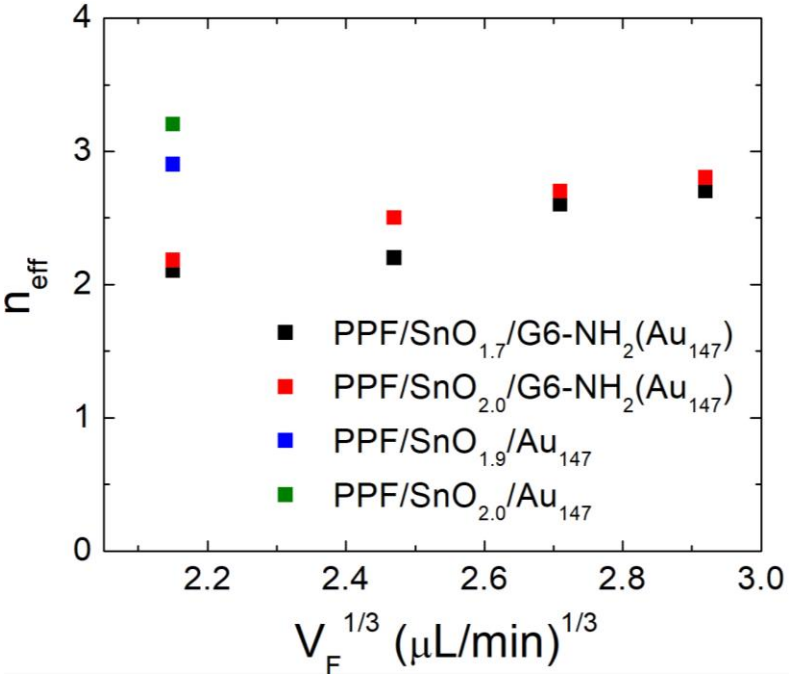

Figure 6.20: Plot of n_{eff} vs. $V_F^{1/3}$ for the indicated electrode modifications. The potential of the collector electrode (CE) was held at 1.35 V (vs. SHE).

Electronic Interactions between AuNPs and $SnO_{1.7}$ and $SnO_{2.0}$ Supports

Theory suggests that the reason for improvements in the ORR electrochemistry are due to electron transfer from surface oxygen vacancies within the SnO_x supports to the AuNPs, which leads to an improved binding strength of OOH* on AuNPs. We next sought to confirm this theoretical finding by finding experimental evidence for electronic interactions between Au_{147} NPs and the SnO_x supports. This was accomplished using

XPS to determine the positions of Au 4f and Sn $3d_{5/2}$ XPS peaks before and after UV/O_3 treatment.

Before the UV/O_3 treatment, the Au 4f region of the PPF/$SnO_{1.7}$/G6-NH_2(Au_{147}) interface can be deconvoluted into two peaks at 84.31 eV (Au $4f_{7/2}$) and 88.0 eV (Au $4f_{5/2}$) (Figure 6.21a). These peaks are assigned to metallic Au.[88,146] Following the UV/O_3 treatment and the subsequent electrochemical reduction, the positions of two Au 4f peaks for PPF/$SnO_{1.9}$/Au_{147} shift by -0.28 eV so that the Au $4f_{7/2}$ peak is now observed at 84.03 eV. Similarly, the positions of the Sn $3d_{5/2}$ peaks before and after UV/O_3 (followed by electrochemical reduction of AuO_x) were found to be at 487.20 eV and 487.37 eV, respectively (Figure 6.21b). This change of +0.17 eV, taken together with the previously discussed negative shift in the Au 4f BE, indicates partial electron transfer from the $SnO_{1.7}$ support to Au_{147} NPs following removal of the dendrimer. The increased asymmetry of the Au 4f peaks following removal of the dendrimers (Figure 6.21a) further confirms partial charge transfer.[126]

Changes in positions of Au 4f and Sn $3d_{5/2}$ peaks were analyzed in a similar fashion for the PPF/$SnO_{2.0}$/G6-NH_2(Au_{147}) interface. Before UV/O_3 treatment, two Au 4f peaks are present at 84.38 eV and 88.10 eV corresponding to metallic Au (Figure 6.21c). The Sn $3d_{5/2}$ peak is at 487.14 eV (Figure 6.21d). Following UV/O_3 treatment, the Au 4f BEs decrease by -0.13 eV and the Au $4f_{7/2}$ peak is now present at 84.25 eV. Following removal of the dendrimers, the Sn $3d_{5/2}$ peak shifts by +0.28 eV to 487.42 eV. As before, this indicates electron transfer from $SnO_{2.0}$ to the Au_{147} NPs.

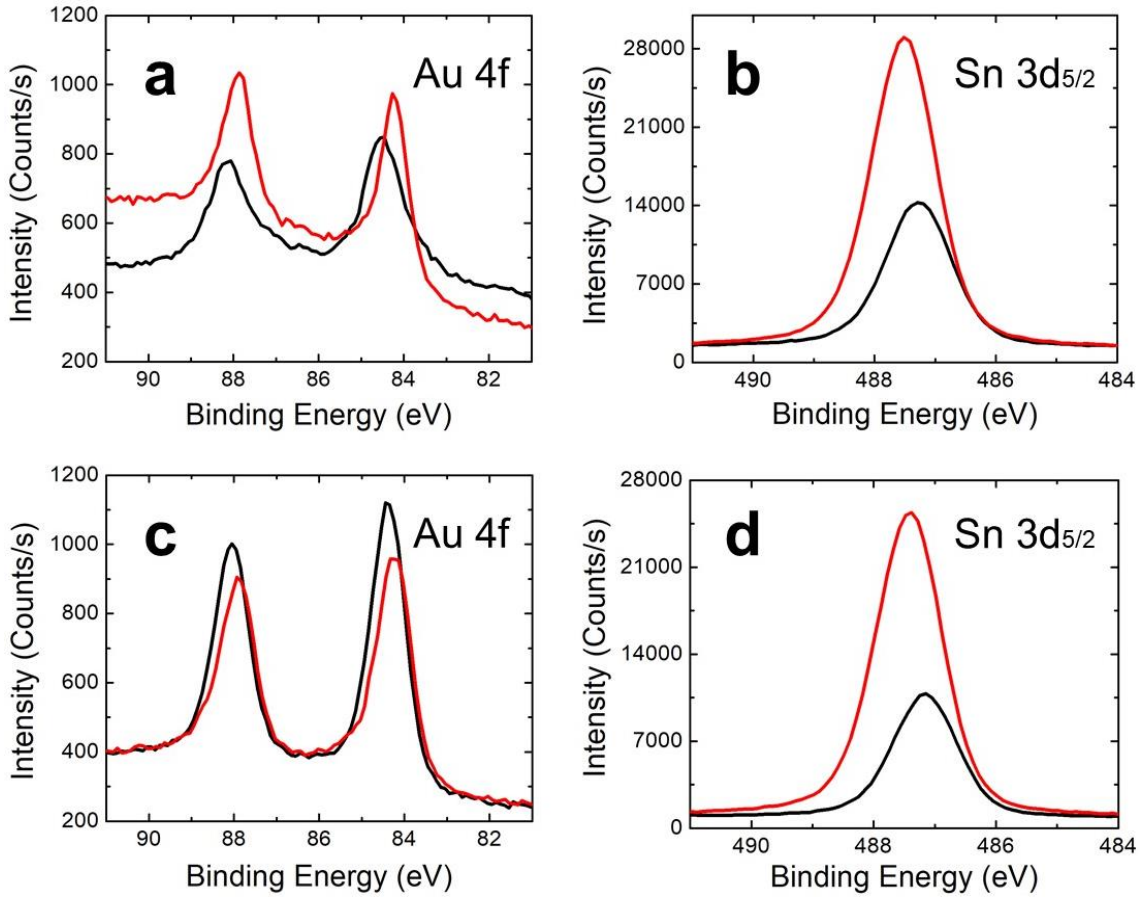

Figure 6.21: High-resolution XPS spectra in the Au 4f and Sn $3d_{5/2}$ regions for (a,b) PPF/$SnO_{1.7}$/G6-NH_2(Au_{147}) and (c,d) PPF/$SnO_{2.0}$/G6-NH_2(Au_{147}) electrodes before the UV/O_3 treatment (black) and after UV/O_3 treatment (followed by electrochemical reduction of Au) (red). All XPS peaks were referenced to the position of the PPF C 1s peak at 284.5 eV.

We previously showed that naked PPF supports and PPF/Al_2O_3 supports do not induce measurable changes in the electronic properties of Pt_{55} NPs.[204] Likewise, there was no change in the onset potential for the ORR regardless of whether the Pt_{55} NPs were in contact with PPF or PPF/Al_2O_3 interfaces. We wondered, however, if these catalytically inactive Al_2O_3 supports behave in the same way when interacting with Au_{147} NPs. Accordingly, we prepared PPF/G6-NH_2(Au_{147}) and PPF/Al_2O_3/G6-NH_2(Au_{147})

electrodes and tested them before and after UV/O_3 treatment using XPS. In both cases, negligible shifts in the positions of the peaks of interest were observed after the removal of the dendrimers. That is, in case of PP/G6-NH_2(Au_{147}), following the UV/O_3 treatment and subsequent electrochemical reduction, the Au 4f peaks shift by -0.04 eV towards lower BE values (Figure 6.22). Similarly, in case of PPF/Al_2O_3/G6-NH_2(Au_{147}), the BEs of the Au 4f and Al 2s peaks shift by 0.01 eV and 0.05 eV, respectively (Figure 6.23). These results indicate that in contrast to the $SnO_{1.7}$ and $SnO_{2.0}$ interfaces, neither the PPF nor the PPF/Al_2O_3 supports exhibit significant electronic interactions with the Au_{147} NPs. This control experiment further supports our contention of partial charge transfer from the SnO_x supports to the Au_{147} NPs.

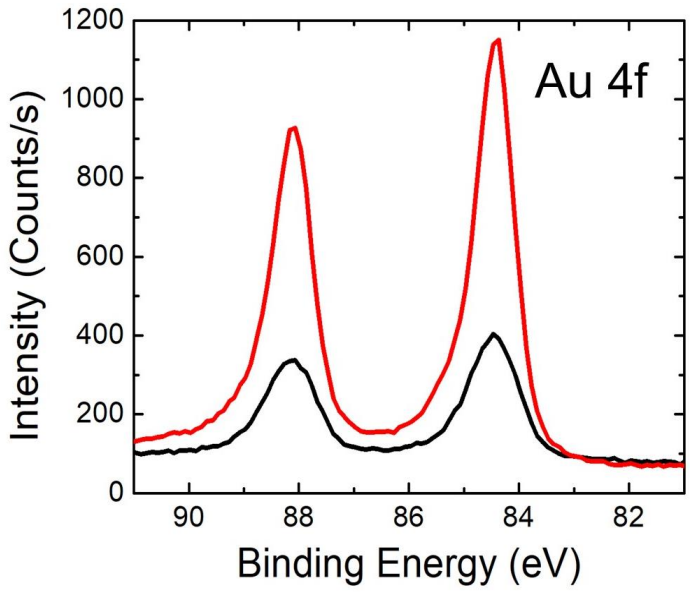

Figure 6.22: High-resolution XPS spectra in the Au 4f region for a PPF/G6-NH_2(Au_{147}) electrode before the UV/O_3 treatment (black) and after UV/O_3 treatment followed by electrochemical reduction of Au (red). The XPS peaks were referenced to the position of the PPF C 1s peak at 284.5 eV.[51,88]

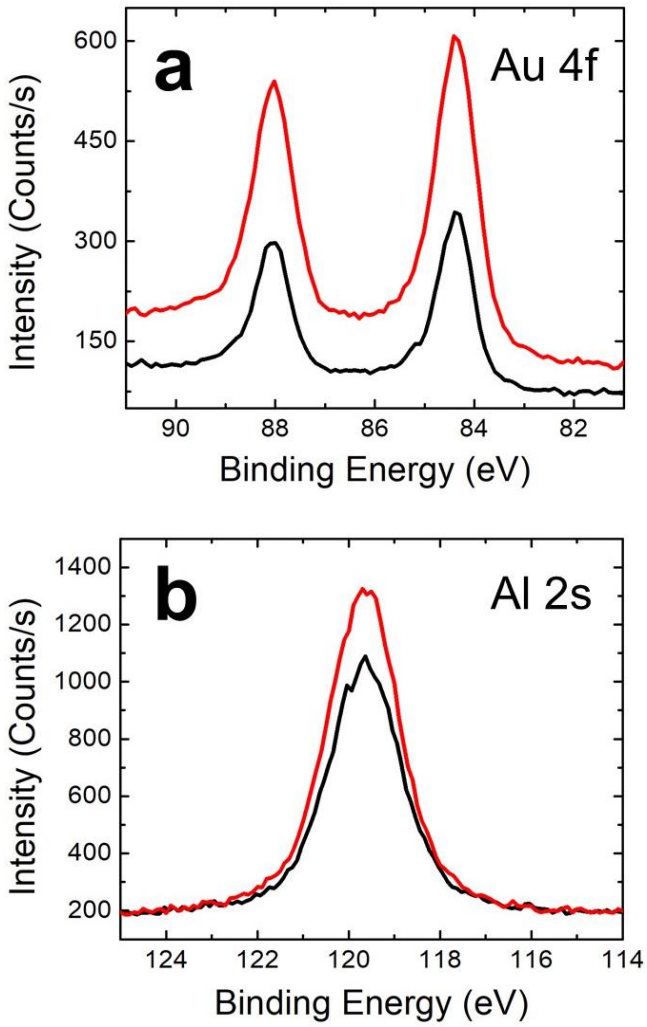

Figure 6.23: High-resolution XPS spectra in the (a) Au 4f and (b) Al 2s regions for a PPF/Al_2O_3/G6-NH_2(Au_{147}) electrode before UV/O_3 treatment (black) and after UV/O_3 treatment followed by electrochemical reduction of Au (red). All XPS peaks were referenced to the position of the PPF C 1s peak at 284.5 eV.[51,88]

SUMMARY AND CONCLUSIONS

Here we have shown that DFT calculations can be used to predict the nature of interactions between SnO_x thin films and AuNPs, and further to understand the effect that

these interactions have on the ability of AuNPs to electrocatalyze the ORR. Specifically, both theoretical predictions and subsequent experimental results have shown that enhancements in the ORR onset potential, kinetics, and pathway occur only when AuNPs directly interact with the SnO_x supports. DFT calculations and experimental results also converge to explain that the observed improvements in the ORR activity arise from electron transfer from surface oxygen vacancies within SnO_x supports to the AuNPs.

The results of this study are significant for three reasons. First, we showed that oxygen surface vacancies can have a significant effect on interactions between supports and overlaying NPs, and that these interactions may have a significant impact on electrocatalytic processes. Second, we have developed a very well-defined experimental model that can be directly correlated to DFT calculations. Third, and most importantly, the calculations reported here were performed prior to the experiments. In other words, this study represents an unusual case of theory accurately predicting the electrocatalytic manifestation of a strong metal support interaction.

The approach described here can help broaden our understanding of the interactions between different metal NPs and metal-oxide supports, and the effect of such interactions on electrocatalytic reactions. We now seek to discover if the predictive approach reported here is unique, or if it can be extended to other combinations of supports and NPs. Experiments are currently underway to determine if predictions made for a second set of materials can be confirmed experimentally. Those results will be reported in due course.

Chapter 7: Conclusions and Outlook

In this dissertation, I have introduced a well-characterized electrocatalyst system suited for studying effects of supports on electrocatalytic activity of overlying metal NPs. Using first principle theory it was possible to accurately model this experimental system, allowing theory to start leading the experimental research. Key points from each chapter are summarized below.

Fist, ultra-thin films of Al_2O_3 (2.5 nm), deposited via ALD, were able to completely passivate eT from underlying PPF electrodes to $Fc(MeOH)_2$ in solution. More importantly, immobilization of G6-OH(Pt_{55}) (1.3 nm) onto the Al_2O_3 surface completely recovered previously passivated eT. Finally, although dendrimers prevented direct contact between the encapsulated Pt_{55} NPs and the underlying Al_2O_3, the PPF/Al_2O_3/G6-OH(Pt_{55}) electrode was active for the ORR.

Second, an efficient UV/O_3 treatment for the removal of G6-OH dendrimers from G6-OH(Pt_{55}) immobilized onto a PPF electrode was presented. The UV/O_3 treatment did not damage PPF electrodes nor did it affect the size, shape, or composition of the encapsulated NPs as confirmed by SEM, STEM, XPS, and electrochemical experiments. Using the developed UV/O_3 treatment is possible to control the expression of interactions between NPs and their supports. This means that the developed system is near-perfect for studying support effects, because the exact same electrode can be examined with support effects turned off or on simply by removing the dendrimer.

Third, a microfluidic flow cell is introduced allowing the study of complex surface modifications such as ALD-modified electrodes or electrodes treated with UV/O_3. The main advantage of this flow cell is that both generation and collection electrodes can be fabricated independently of each other, outside the cell. The electrodes

can then be introduced into the flow cell for analysis, removed from the cell again for modifications, and reintroduced for additional analysis. Using Levich and generation-collection experiments, we showed that neither presence of the dendrimers nor direct interactions between Al_2O_3 and PtNPs affect the PtNP activity for the ORR. This is expected as Al_2O_3 is not a reducible oxide, and it will be used as a control system for the future studies.

Finally, we moved towards a new phase in our research in which theoretical calculations are used to design electrocatalysts with desired properties. The theoretical predictions were then tested experimentally. Specifically, we studied the ORR electrocatalyzed at PPF/$SnO_{1.7}$/G6-NH_2(Au_{147}) and PPF/$SnO_{2.0}$/G6-NH_2(Au_{147}) electrodes in the absence and presence of support/NP interactions. Experimental results of this study agreed perfectly with the DFT calculations. That is, improvements in the ORR activity for both electrodes were only observed when AuNPs interacted directly with SnO_x supports. The enhancements in the electroactivity occurred due to the electron transfer from oxygen vacancies within the SnO_x support to the overlying AuNPs.

Now that we have shown that the experimental system can accurately be modeled using DFT, we will continue using a theory-first approach in the future studies. Our first objective in this regard will focus on understanding the effects of various reducible MO supports (e.g. TiO_2, CeO_2, and MnO_x) on the electrocatalytic activity of monometallic NPs (Pt, Au, and Pd) for the ORR. Next, this collaborative study will be extended to include bimetallic NPs (core@shell and alloy) and more complex reactions that are of crucial importance for the production and use of chemical fuels (alcohol oxidation and formic acid oxidation). Compared to the current paradigm of trial and error discovery,

this fundamental study is a more efficient approach to catalyst design allowing for much needed deeper understanding of support effects in electrocatalysis.

References

(1) Sehested, J.; Larsen, K. E.; Kustov, A. L.; Frey, A. M.; Johannessen, T.; Bligaard, T.; Andersson, M. P.; Nørskov, J. K.; Christensen, C. H. Discovery of Technical Methanation Catalysts Based on Computational Screening. *Top. Catal.* **2007**, *45* (1–4), 9–13.

(2) Cuenya, B. R. Synthesis and Catalytic Properties of Metal Nanoparticles: Size, Shape, Support, Composition, and Oxidation State Effects. *Thin Solid Films* **2010**, *518* (12), 3127–3150.

(3) Daio, T.; Staykov, A.; Guo, L.; Liu, J.; Tanaka, M.; Matthew Lyth, S.; Sasaki, K. Lattice Strain Mapping of Platinum Nanoparticles on Carbon and SnO_2 Supports. *Sci. Rep.* **2015**, *5* (1), 13126.

(4) Jimmy, J. Advanced Electron Microscopy of Metal – Support Interactions in Supported Metal Catalysts. *ChemCatChem* **2011**, *3*, 934–948.

(5) Xing, W.; Yin, G.; Zhang, J. *Rotating Electrode Methods and Oxygen Reduction Electrocatalysts*; Elsevier B.V, 2014.

(6) Garsany, Y.; Epshteyn, A.; Purdy, A. P.; More, K. L.; Swider-Lyons, K. E. High-Activity, Durable Oxygen Reduction Electrocatalyst: Nanoscale Composite of Platinum-Tantalum Oxyphosphate on Vulcan Carbon. *J. Phys. Chem. Lett.* **2010**, *1* (13), 1977–1981.

(7) Sasaki, K.; Zhang, L.; Adzic, R. R. Niobium Oxide-Supported Platinum Ultra-Low Amount Electrocatalysts for Oxygen Reduction. *Phys. Chem. Chem. Phys.* **2008**, *10* (1), 159–167.

(8) Calle-Vallejo, F.; Koper, M. T. M.; Bandarenka, A. S. Tailoring the Catalytic Activity of Electrodes with Monolayer Amounts of Foreign Metals. *Chem. Soc. Rev.* **2013**, *42* (12), 5210.

(9) Liu, J. J. Advanced Electron Microscopy of Metal-Support Interactions in Supported Metal Catalysts. *ChemCatChem* **2011**, *3* (6), 934–948.

(10) Tsai, E. Dendrimer-Encapsulated Nanoparticles : Vehicles for Drug Delivery , with an Emphasis On. *Cosmos* **2011**, *8*, 1–16.

(11) Bronstein, L. M.; Shifrina, Z. B. Dendrimers as Encapsulating, Stabilizing, or Directing Agents for Inorganic Nanoparticles. *Chem. Rev.* **2011**, *111*, 5301–5344.

(12) Dendritech, PAMAM Dendrimers. http://www.dendritech.com/pamam.html (accessed Jul 6, 2018).

(13) Pande, S.; Weir, M. G.; Zaccheo, B. A.; Crooks, R. M. Synthesis, Characterization, and Electrocatalysis Using Pt and Pd Dendrimer-Encapsulated

Nanoparticles Prepared by Galvanic Exchange. *New J. Chem.* **2011**, *35* (10), 2054.

(14) Balogh, L.; Tomalia, D. A. Poly(Amidoamine) Dendrimer-Templated Nanocomposites. 1. Synthesis of Zerovalent Copper Nanoclusters. *J. Am. Chem. Soc.* **1998**, *120* (29), 7355–7356.

(15) Anderson, R. M.; Yancey, D. F.; Loussaert, J. A.; Crooks, R. M. Multistep Galvanic Exchange Synthesis Yielding Fully Reduced Pt Dendrimer-Encapsulated Nanoparticles. *Langmuir* **2014**, *30* (49), 15009–15015.

(16) Kim, Y.-G.; Oh, S.-K.; Crooks, R. M. Preparation and Characterization of 1 - 2 Nm Dendrimer-Encapsulated Gold Nanoparticles Having Very Narrow Size Distributions. *Chem. Mater.* **2004**, *16* (18), 167–172.

(17) Anderson, R. M.; Yancey, D. F.; Zhang, L.; Chill, S. T.; Henkelman, G.; Crooks, R. M. A Theoretical and Experimental Approach for Correlating Nanoparticle Structure and Electrocatalytic Activity. *Acc. Chem. Res.* **2015**, *48* (5), 1351–1357.

(18) Anderson, R. M.; Yancey, D. F.; Loussaert, J. A.; Crooks, R. M.; Nanoparticles, D.; Anderson, R. M.; Yancey, D. F.; Loussaert, J. A.; Crooks, R. M. Multistep Galvanic Exchange Synthesis Yielding Fully Reduced Pt Dendrimer-Encapsulated Nanoparticles. *Langmuir* **2014**, *30* (49), 15009–15015.

(19) Myers, V. S.; Weir, M. G.; Carino, E. V; Yancey, D. F.; Pande, S.; Crooks, R. M. Dendrimer-Encapsulated Nanoparticles : New Synthetic and Characterization Methods and Catalytic Applications. *Chem. Sci* **2011**, *2*, 1632.

(20) Astruc, D. Transition - Metal Nanoparticles in Catalysis : From Historical Background to the State - of - the Art. In *Nanoparticles and Catalysis*; 2008; pp 1–48.

(21) Ye, H.; Scott, R. W. J.; Crooks, R. M. Synthesis , Characterization , and Surface Immobilization of Platinum and Palladium Nanoparticles Encapsulated within Amine-Terminated Poly (Amidoamine) Dendrimers. *Langmuir* **2004**, *20* (5), 10420–10425.

(22) Petkov, V.; Bedford, N.; Knecht, M. R.; Weir, M. G.; Crooks, R. M.; Tang, W.; Henkelman, G.; Frenkel, A. Periodicity and Atomic Ordering in Nanosized Particles of Crystals. *J. Phys. Chem. C* **2008**, *112*, 8907–8911.

(23) Iyyamperumal, R.; Zhang, L.; Henkelman, G.; Crooks, R. M. Efficient Electrocatalytic Oxidation of Formic Acid Using Au@Pt. *J. Am. Chem. Soc.* **2013**, *135*, 5521–5524.

(24) Bard, A. J.; Faulkner, L. R. *Electrochemical Methods: Fundamentals and Applications*, 2nd ed.; John Wiley & Sons: New York, 2001.

(25) Nazarov, D.; Bobrysheva, N. P.; Osmolovskaya, O. M.; Osmolovsky, M. G.; Smirnov, V. M. Atomic Layer Deposition of Tin Dioxide Nanofilms: A Review.

Rev. Adv. Mater. Sci. **2015**, *40*, 262–275.

(26) Instruments, M. K. S. Ozone as the Oxidizing Precursor in Atomic Layer Deposition. **2005**, No. December, 1–4.

(27) George, S. M. Atomic Layer Deposition: An Overview. *Chem. Rev* **2010**, *110*, 111–131.

(28) Goldstein, D. N.; McCormick, J. a.; George, S. M. Al_2O_3 Atomic Layer Deposition with Trimethylaluminum and Ozone Studied by in Situ Transmission FTIR Spectroscopy and Quadrupole Mass Spectrometry. *J. Phys. Chem. C* **2008**, *112* (49), 19530–19539.

(29) Grabar, K. C.; Allison, K. J.; Baker, B. E.; Bright, R. M.; Brown, K. R.; Freeman, R. G.; Fox, A. P.; Keating, C. D.; Musick, M. D.; Natan, M. J. Two-Dimensional Arrays of Colloidal Gold Particles: A Flexible Approach to Macroscopic Metal Surfaces. *Langmuir* **1996**, *12* (10), 2353–2361.

(30) Zhao, J.; Wasem, M.; Bradbury, C. R.; Fermín, D. J. Charge Transfer across Self-Assembled Nanoscale Metal−Insulator−Metal Heterostructures. *J. Phys. Chem. C* **2008**, *112* (18), 7284–7289.

(31) Bradbury, C. R.; Zhao, J.; Fermín, D. J. Distance-Independent Charge-Transfer Resistance at Gold Electrodes Modified by Thiol Monolayers and Metal Nanoparticles. *J. Phys. Chem. C* **2008**, *112* (27), 10153–10160.

(32) Kissling, G. P.; Miles, D. O.; Fermín, D. J. Electrochemical Charge Transfer Mediated by Metal Nanoparticles and Quantum Dots. *Phys. Chem. Chem. Phys.* **2011**, *13* (48), 21175–21185.

(33) Shein, J. B.; Lai, L. M. H.; Eggers, P. K.; Paddon-Row, M. N.; Gooding, J. J. Formation of Efficient Electron Transfer Pathways by Adsorbing Gold Nanoparticles to Self-Assembled Monolayer Modified Electrodes. *Langmuir* **2009**, *25* (18), 11121–11128.

(34) Gooding, J. J.; Alam, M. T.; Barfidokht, A.; Carter, L. Nanoparticle Mediated Electron Transfer Across Organic Layers: From Current Understanding to Applications. *J. Braz. Chem. Soc.* **2013**, *35*, 418–426.

(35) Chazalviel, J.-N.; Allongue, P. On the Origin of the Efficient Nanoparticle Mediated Electron Transfer across a Self-Assembled Monolayer. *J. Am. Chem. Soc.* **2011**, *133* (4), 762–764.

(36) Xiang, W.; Yin, G.; Zhang, J. *Rotating Electrode Methods and Oxydation Reduction Electrocatalysis*; Elsevier B.V: Waltham, MA, 2014.

(37) Sánchez-Sánchez, C. M.; Bard, A. J. Hydrogen Peroxide Production in the Oxygen Reduction Reaction at Different Electrocatalysts as Quantified by Scanning Electrochemical Microscopy. *Anal. Chem.* **2009**, *81* (19), 8094–8100.

(38) Bing, Y.; Liu, H.; Zhang, L.; Ghosh, D.; Zhang, J. Nanostructured Pt-Alloy Electrocatalysts for PEM Fuel Cell Oxygen Reduction Reaction. *Chem. Soc. Rev.* **2010**, *39* (6), 2184.

(39) Koper, M. T. M. *Fuel Cell Catalysis, A Surface Science Approach*; John Wiley & Sons: New Jersey, 2009.

(40) Wang, Y.; Widmann, D.; Behm, R. J. Influence of TiO_2 Bulk Defects on CO Adsorption and CO Oxidation on Au/TiO_2: Electronic Metal-Support Interactions (EMSIs) in Supported Au Catalysts. *ACS Catal.* **2017**, *7* (4), 2339–2345.

(41) Park, S.-A.; Lim, H.; Kim, Y.-T. Enhanced Oxygen Reduction Reaction Activity Due to Electronic Effects between Ag and Mn_3O_4 in Alkaline Media. *ACS Catal.* **2015**, *5* (7), 3995–4002.

(42) Tauster, S. J. Strong Metal-Support Interactions. *Acc. Chem. Res.* **1987**, *20* (11), 389–394.

(43) Peng, X.; Pan, Q.; Rempel, G. L. Bimetallic Dendrimer-Encapsulated Nanoparticles as Catalysts : A Review of the Research Advances. *Chem. So* **2008**, *37*, 1619–1628.

(44) Lang, H.; May, R. A.; Iversen, B. L.; Chandler, B. D. Dendrimer-Encapsulated Nanoparticle Precursors to Supported Platinum Catalysts. *J. Am. Chem. Soc.* **2003**, *125* (48), 14832–14836.

(45) Aikens, C. M. Electronic Structure of Ligand-Passivated Gold and Silver Nanoclusters. *J. Phys. Chem. Lett.* **2011**, *2*, 99–104.

(46) Zhang, L.; Anderson, R. M.; Crooks, R. M.; Henkelman, G. Correlating Structure and Function of Metal Nanoparticles for Catalysis. *Surf. Sci.* **2015**, *640*, 65–72.

(47) Zhang, L.; Iyyamperumal, R.; Yancey, D. F.; Crooks, R. M.; Henkelman, G. Design of Pt-Shell Nanoparticles with Alloy Cores for the Oxygen Reduction Reaction. *ACS Nano* **2013**, *7* (10), 9168–9172.

(48) Anderson, R. M.; Zhang, L.; Loussaert, J. A.; Frenkel, A. I.; Henkelman, G.; Crooks, R. M. An Experimental and Theoretical Investigation of the Inversion of Pd @ Pt. *ACS Nano* **2013**, *7* (10), 9345–9353.

(49) Luo, L.; Zhang, L.; Henkelman, G.; Crooks, R. M. Unusual Activity Trend for CO Oxidation on Pd_xAu_{140-x}@Pt Core@Shell Nanoparticle Electrocatalysts. *J. Phys. Chem. Lett.* **2015**, *6* (13), 2562–2568.

(50) Pozun, Z. D.; Rodenbusch, S. E.; Keller, E.; Tran, K.; Tang, W.; Stevenson, K. J.; Henkelman, G. A Systematic Investigation of p - Nitrophenol Reduction by Bimetallic Dendrimer Encapsulated Nanoparticles. *J. Phys. Chem. C* **2013**, *117*, 7598–7604.

(51) Loussaert, J. A.; Fosdick, S. E.; Crooks, R. M. Electrochemical Properties of Metal-Oxide-Coated Carbon Electrodes Prepared by Atomic Layer Deposition. *Langmuir* **2014**, *30* (45), 13707–13715.

(52) Kim, H. J.; Kearney, K. L.; Le, L. H.; Pekarek, R. T.; Rose, M. J. Platinum-Enhanced Electron Transfer and Surface Passivation through Ultrathin Film Aluminum Oxide (Al_2O_3) on Si(111)–CH_3 Photoelectrodes. *ACS Appl. Mater. Interfaces* **2015**, *7* (16), 8572–8584.

(53) Hoex, B.; Schmidt, J.; Bock, R.; Altermatt, P. P.; van de Sanden, M. C. M.; Kessels, W. M. M. Excellent Passivation of Highly Doped P-Type Si Surfaces by the Negative-Charge-Dielectric Al_2O_3. *Appl. Phys. Lett.* **2007**, *91* (11), 112107.

(54) Liu, Z. H.; Ng, G. I.; Zhou, H.; Arulkumaran, S.; Maung, Y. K. T. Reduced Surface Leakage Current and Trapping Effects in AlGaN/GaN High Electron Mobility Transistors on Silicon with SiN/Al_2O_3 Passivation. *Appl. Phys. Lett.* **2011**, *98* (11), 2009–2012.

(55) Ranganathan, S.; McCreery, R.; Majji, S. M.; Madou, M. Photoresist-Derived Carbon for Microelectromechanical Systems and Electrochemical Applications. *J. Electrochem. Soc.* **2000**, *147* (1), 277–282.

(56) Ranganathan, S.; McCreery, R. L. Electroanalytical Performance of Carbon Films with Near-Atomic Flatness. *Anal. Chem.* **2001**, *73* (5), 893–900.

(57) Self-Assembled Metal Colloids Monolayers: An Approach to SERS Substrates. *Science (80-.).* **1995**, *267*, 1629.

(58) Bethell, D.; Brust, M.; Schiffrin, D. J.; Kiely, C. From Monolayers to Nanostructured Materials: An Organic Chemist's View of Self-Assembly. *J. Electroanal. Chem.* **1996**, *409*, 137–143.

(59) Brust, M.; Bethell, D.; Kiely, C. J.; Schiffrin, D. J. Self-Assembled Gold Nanoparticle Thin Films with Nonmetallic Optical and Electronic Properties. *Langmuir* **1998**, *14* (19), 5425–5429.

(60) Horswell, S. L.; O'Neil, I. a; Schiffrin, D. J. Kinetics of Electron Transfer at Pt Nanostructured Film Electrodes. *J. Phys. Chem. B* **2003**, *107*, 4844–4854.

(61) Zhao, J.; Bradbury, C. R.; Fermin, D. J. Long-Range Electronic Communication between Metal Nanoparticles and Electrode Surfaces Separated by Polyelectrolyte Multilayer Films. *J. Phys. Chem. C* **2008**, *112* (17), 6832–6841.

(62) Zhao, J.; Bradbury, C. R.; Huclova, S.; Potapova, I.; Carrara, M.; Fermín, D. J. Nanoparticle-Mediated Electron Transfer across Ultrathin Self-Assembled Films. *J. Phys. Chem. B* **2005**, *109* (48), 22985–22994.

(63) Barfidokht, A.; Ciampi, S.; Luais, E.; Darwish, N.; Gooding, J. J. Distance-Dependent Electron Transfer at Passivated Electrodes Decorated by Gold

Nanoparticles. *Anal. Chem.* **2013**, *85* (2), 1073–1080.

(64) Nuzzo, R. G.; Allara, D. L. Adsorption of Bifunctional Organic Disulfides on Gold Surfaces. *J. Am. Chem. Soc.* **1983**, *105* (13), 4481–4483.

(65) Kim, J.; Kim, B. K.; Cho, S. K.; Bard, A. J. Tunneling Ultramicroelectrode: Nanoelectrodes and Nanoparticle Collisions. *J. Am. Chem. Soc.* **2014**, *136* (23), 8173–8176.

(66) Zhang, J.; Vukmirovic, M. B.; Sasaki, K.; Nilekar, A. U.; Mavrikakis, M.; Adzic, R. R. Mixed-Metal Pt Monolayer Electrocatalysts for Enhanced Oxygen Reduction Kinetics. *J. Am. Chem. Soc.* **2005**, *127* (36), 12480–12481.

(67) Zhou, W.-P.; Axnanda, S.; White, M. G.; Adzic, R. R.; Hrbek, J. Enhancement in Ethanol Electrooxidation by SnO_x Nanoislands Grown on Pt(111): Effect of Metal Oxide–Metal Interface Sites. *J. Phys. Chem. C* **2011**, *115* (33), 16467–16473.

(68) Wu, Z.-S.; Zhou, G.; Yin, L.-C.; Ren, W.; Li, F.; Cheng, H.-M. Graphene/Metal Oxide Composite Electrode Materials for Energy Storage. *Nano Energy* **2012**, *1* (1), 107–131.

(69) Wang, D.; Kou, R.; Choi, D.; Yang, Z.; Nie, Z.; Li, J.; Saraf, L. V.; Hu, D.; Zhang, J.; Graff, G. L.; et al. Ternary Self-Assembly of Ordered Metal Oxide-Graphene Nanocomposites for Electrochemical Energy Storage. *ACS Nano* **2010**, *4* (3), 1587–1595.

(70) Diao, P.; Liu, Z. Electrochemistry at Chemically Assembled Single-Wall Carbon Nanotube Arrays. *J. Phys. Chem. B* **2005**, *109* (44), 20906–20913.

(71) Su, L.; Gao, F.; Mao, L. Electrochemical Properties of Carbon Nanotube (CNT) Film Electrodes Prepared by Controllable Adsorption of CNTs onto an Alkanethiol Monolayer Self-Assembled on Gold Electrodes. *Anal. Chem.* **2006**, *78* (8), 2651–2657.

(72) Ye, M.; Gong, J.; Lai, Y.; Lin, C.; Lin, Z. High-Efficiency Photoelectrocatalytic Hydrogen Generation Enabled by Palladium Quantum Dots-Sensitized TiO2 Nanotube Arrays. *J. Am. Chem. Soc.* **2012**, *134* (38), 15720–15723.

(73) Chai, H.; Liu, H.; Guo, X.; Zheng, D.; Kutes, Y.; Huey, B. D.; Rusling, J. F.; Hu, N. Long Distance Electron Transfer Across >100 Nm Thick Au Nanoparticle/Polyion Films to a Surface Redox Protein. *Electroanalysis* **2012**, *24* (5), 1129–1140.

(74) Baturina, O. A.; Garsany, Y.; Zega, T. J.; Stroud, R. M.; Schull, T.; Swider-Lyons, K. E. Oxygen Reduction Reaction on Platinum/Tantalum Oxide Electrocatalysts for PEM Fuel Cells. *J. Electrochem. Soc.* **2008**, *155* (12), B1314-1321.

(75) Korovina, A.; Garsany, Y.; Epshteyn, A.; Purdy, A. P.; More, K.; Swider-lyons, K. E.; Ramaker, D. E. Understanding Oxygen Reduction on Tantalum Oxyphosphate

and Tantalum Oxide Supported Platinum by X - Ray Absorption Spectroscopy. *J. Phys. Chem. C* **2012**, *116*, 18175–18183.

(76) Zhou, W.-P.; An, W.; Su, D.; Palomino, R.; Liu, P.; White, M. G.; Adzic, R. R. Electrooxidation of Methanol at SnOx –Pt Interface: A Tunable Activity of Tin Oxide Nanoparticles. *J. Phys. Chem. Lett.* **2012**, *3* (22), 3286–3290.

(77) Donner, S.; Li, H. W.; Yeung, E. S.; Porter, M. D. Fabrication of Optically Transparent Carbon Electrodes by the Pyrolysis of Photoresist Films: Approach to Single-Molecule Spectroelectrochemistry. *Anal. Chem.* **2006**, *78* (8), 2816–2822.

(78) Electrocatalysis of Proton-Coupled Electron-Transfer at Glassy Carbon Electrodes. *J. Am. Chem. Soc.* **1985**, *107*, 1845–1853.

(79) Moulder, J. F.; Stickle, W. F.; Sobol, P. E.; Bomben, K. D. *Handbook of X-Ray Photoelectron Spectroscopy*; Physical Electronics USA, Inc.: Chanhassen, MN, 1995.

(80) Yu, S. S. C.; Downard, A. J. Photochemical Grafting and Activation of Organic Layers on Glassy Carbon and Pyrolyzed Photoresist Films. *Langmuir* **2007**, *23* (8), 4662–4668.

(81) Anariba, F.; DuVall, S. H.; McCreery, R. L. Mono-and Multilayer Formation by Diazonium Reduction on Carbon Surfaces Monitored with Atomic Force Microscopy "Scratching." *Anal. Chem.* **2003**, *75* (15), 3837–3844.

(82) Kostecki, R.; Schnyder, B.; Alliata, D.; Song, X.; Kinoshita, K.; Kötz, R. Surface Studies of Carbon Films from Pyrolyzed Photoresist. *Thin Solid Films* **2001**, *396* (1–2), 36–43.

(83) Childres, I.; Jauregui, L. A.; Park, W.; Cao, H.; Chen, Y. P. Raman Spectroscopy of Graphene and Related Materials. *Dev. Phot. Mater. Res.* **2013**, 978–981.

(84) Nathan, M. I. Raman Spectra of Glassy Carbon. *J. Appl. Phys.* **1974**, *45* (5), 2370.

(85) Cambridge NanoTech, Simply ALD www.cambridgenanotech.com (accessed May 4, 2018).

(86) Sun, L.; Crooks, R. M. Imaging of Defects Contained within N-Alkylthiol Monolayers by Combination of Underpotential Deposition and Scanning Tunneling Microscopy: Kinetics of Self-Assembly. *J. Electrochem. Soc.* **1991**, *138* (8), L23.

(87) Luo, L.; Zhang, L.; Henkelman, G.; Crooks, R. M. Unusual Activity Trend for CO Oxidation on Pd_xAu_{140-x}@Pt Core@Shell Nanoparticle Electrocatalysts. *J. Phys. Chem. Lett.* **2015**, *6* (13), 2562–2568.

(88) NIST X-Ray Photoelectron Spectroscopy Database, Version 4.1, National Institute of Standards and Technology: Gaithersburg, MD http://srdata.nist.gov/xps/.

(89) Anderson, R. M.; Zhang, L.; Loussaert, J. A.; Frenkel, A. I.; Henkelman, G.; Crooks, R. M. An Experimental and Theoretical Investigation of the Inversion of Pd@Pt Core@Shell Dendrimer-Encapsulated Nanoparticles. *ACS Nano* **2013**, *7* (10), 9345–9353.

(90) Ye, H.; Crooks, R. M. Electrocatalytic O2 Reduction at Glassy Carbon Electrodes Modified with Dendrimer-Encapsulated Pt Nanoparticles. *J. Am. Chem. Soc.* **2005**, *127* (13), 4930–4934.

(91) Ye, H.; Crooks, J. A.; Crooks, R. M. Effect of Particle Size on the Kinetics of the Electrocatalytic Oxygen Reduction Reaction Catalyzed by Pt Dendrimer-Encapsulated Nanoparticles. **2007**, No. 26, 11901–11906.

(92) Dumitrescu, I.; Yancey, D. F.; Crooks, R. M. Dual-Electrode Microfluidic Cell for Characterizing Electrocatalysts. *Lab Chip* **2012**, *12* (5), 986.

(93) Anicet, N.; Bourdillon, C.; Moiroux, J.; Savéant, J.-M. Electron Transfer in Organized Assemblies of Biomolecules. Step-by-Step Avidin/Biotin Construction and Dynamic Characteristics of a Spatially Ordered Multilayer Enzyme Electrode. *J. Phys. Chem. B* **1998**, *102* (49), 9844–9849.

(94) Mampallil, D.; Mathwig, K.; Kang, S.; Lemay, S. G. Reversible Adsorption of Outer-Sphere Redox Molecules at Pt Electrodes. *J. Phys. Chem. Lett.* **2014**, *5* (3), 636–640.

(95) Dyne, J.; Lin, Y. S.; Lai, L. M. H.; Ginges, J. Z.; Luais, E.; Peterson, J. R.; Goon, I. Y.; Amal, R.; Gooding, J. J. Some More Observations on the Unique Electrochemical Properties of Electrode-Monolayer-Nanoparticle Constructs. *ChemPhysChem* **2010**, *11* (13), 2807–2813.

(96) Sun, P.; Mirkin, M. V. Kinetics of Electron-Transfer Reactions at Nanoelectrodes. *Anal. Chem.* **2006**, *78* (18), 6526–6534.

(97) *Nanoparticles and Catalysis*; Astruc, D., Ed.; Wiley-VCH: Weinheim, 2008.

(98) Anderson, R. M.; Zhang, L.; Wu, D.; Brankovic, S. R.; Henkelman, G.; Crooks, R. M. A Theoretical and Experimental In-Situ Electrochemical Infrared Spectroscopy Study of Adsorbed CO on Pt Dendrimer-Encapsulated Nanoparticles. *J. Electrochem. Soc.* **2016**, *163* (4), 3061–3065.

(99) Crump, C. J.; Gilbertson, J. D.; Chandler, B. D. CO Oxidation and Toluene Hydrogenation by Pt/TiO2 Catalysts Prepared from Dendrimer Encapsulated Nanoparticle Precursors. *Top Catal* **2008**, *49*, 233–240.

(100) Niu, Y.; Crooks, R. M. Dendrimer-Encapsulated Metal Nanoparticles and Their Applications to Catalysis. *Sci. Direct* **2003**, *6*, 1049–1059.

(101) Buhleier, E.; Wehner, W.; Vogtle, F. ′ Cascade′ - and ′Nonskid-Chain-Likw′ Synthesis of Molecular Cavity Topologies. *Chem. Informationsd.* **1978**, *9* (25).

(102) Scott, R. W. J.; Wilson, O. M.; Crooks, R. M. Synthesis, Characterization, and Applications of Dendrimer-Encapsulated Nanoparticles. *J. Phys. Chem. B* **2005**, *109* (2), 692–704.

(103) Patel, H. N.; Patel, P. M. Dendrimer Applications–a Review. *Int J Pharm Bio Sci* **2013**, *4* (2), 454–463.

(104) Singh, I.; Rehni, A. K.; Kalra, R.; Joshi, G.; Kumar, M. Dendrimers and Their Pharmaceutical Applications–a Review. *Pharmazie* **2008**, *63*, 491–496.

(105) Menjoge, A. R.; Kannan, R. M.; Tomalia, D. A. Dendrimer-Based Drug and Imaging Conjugates : Design Considerations for Nanomedical Applications. *Drug Discov. Today* **2010**, *15* (5–6), 171–185.

(106) Shadrack, D. M.; Mubofu, E. B.; Nyandoro, S. S. Synthesis of Polyamidoamine Dendrimer for Encapsulating Tetramethylscutellarein for Potential Bioactivity Enhancement. *Int. J. Mol. Sci.* **2015**, *16*, 26363–26377.

(107) Zheng, J.; Zhang, C.; Dickson, R. M. Highly Fluorescent, Water-Soluble, Size-Tunable Gold Quantum Dots. *Phys. Rev. Lett.* **2004**, *93* (7), 5–8.

(108) Petty, J. T.; Fan, C.; Story, S. P.; Sengupta, B.; St. John Iyer, A.; Prudowsky, Z.; Dickson, R. M. DNA Encapsulation of 10 Silver Atoms Producing a Bright, Modulatable, near-Infrared-Emitting Cluster. *J. Phys. Chem. Lett.* **2010**, *1* (17), 2524–2529.

(109) Oh, S.; Kim, Y.; Ye, H.; Crooks, R. M. Synthesis , Characterization , and Surface Immobilization of Metal Nanoparticles Encapsulated within Bifunctionalized Dendrimers. *Langmuir* **2003**, *19* (25), 10420–10425.

(110) Yeung, L. K.; Lee Jr., C. T.; Johnston, K. P.; Crooks, R. M. Catalysis in Supercritical CO_2 Using Dendrimer-Encapsulated Palladium Nanoparticles. *Chem. Commun.* **2001**, 2290–2291.

(111) Garcia-Martinez, J. C.; Crooks, R. M. Extraction of Au Nanoparticles Having Narrow Size Distributions from within Dendrimer Templates. *J. Am. Chem. Soc.* **2004**, *126* (49), 16170–16178.

(112) Ostojic, N.; Thorpe, J. H.; Crooks, R. M. Electron Transfer Facilitated by Dendrimer-Encapsulated Pt Nanoparticles Across Ultrathin, Insulating Oxide Films. *JACS* **2016**, *138*, 6829–6837.

(113) Albiter, M. A.; Crooks, R. M.; Zaera, F. Adsorption of Carbon Monoxide on Dendrimer-Encapsulated Platinum Nanoparticles: Liquid versus Gas Phase. *J. Phys. Chem. Lett.* **2010**, *1*, 38–40.

(114) Schalley, C. A.; Verhaelen, C.; Klärner, F. G.; Hahn, U.; Vögtle, F. Gas-Phase Host-Guest Chemistry of Dendritic Viologens and Molecular Tweezers: A Remarkably Strong Effect on Dication Stability. *Angew. Chemie - Int. Ed.* **2005**,

44 (3), 477–480.

(115) Schalley, C. A.; Baytekin, B.; Baytekin, H. T.; Engeser, M.; Felder, T.; Rang, A. Mass Spectrometry as a Tool in Dendrimer Chemistry: From Self-Assembling Dendrimers to Dendrimer Gas-Phase Host–guest Chemistry. *J. Phys. Org. Chem.* **2006**, *19* (8–9), 479–490.

(116) Schalley, C. A. Molecular Recognition and Supramolecular Chemistry in the Gas Phase. *Mass Spectrom. Rev.* **2001**, *20* (5), 253–309.

(117) Fu, Q.; Yang, F.; Bao, X. Interface-Confined Oxide Nanostructures for Catalytic Oxidation Reactions. *Acc. Chem. Res.* **2013**, *46* (8), 1692–1701.

(118) Freund, H. J.; Heyde, M.; Nilius, N.; Schauermann, S.; Shaikhutdinov, S.; Sterrer, M. Model Studies on Heterogeneous Catalysts at the Atomic Scale: From Supported Metal Particles to Two-Dimensional Zeolites. *J. Catal.* **2013**, *308*, 154–167.

(119) Pacchioni, G. Electronic Interactions and Charge Transfers of Metal Atoms and Clusters on Oxide Surfaces. *Phys. Chem. Chem. Phys.* **2013**, *15* (6), 1737.

(120) Geukens, I.; De Vos, D. E. Organic Transformations on Metal Nanoparticles: Controlling Activity, Stability, and Recyclability by Support and Solvent Interactions. *Langmuir* **2013**, *29* (10), 3170–3178.

(121) Aliaga, C.; Park, J. Y.; Yamada, Y.; Lee, H. S.; Tsung, C.-K.; Yang, P.; Somorjai, G. A. Sum Frequency Generation and Catalytic Reaction Studies of the Removal of Organic Capping Agents from Pt Nanoparticles by UV−Ozone Treatment. *J. Phys. Chem. C* **2009**, *113* (15), 6150–6155.

(122) Ozturk, O.; Black, T. J.; Perrine, K.; Pizzolato, K.; Williams, C. T.; Parsons, F. W.; Ratliff, J. S.; Gao, J.; Murphy, C. J.; Xie, H.; et al. Thermal Decomposition of Generation-4 Polyamidoamine Dendrimer Films: Decomposition Catalyzed by Dendrimer-Encapsulated Pt Particles. *Langmuir* **2005**, *21* (9), 3998–4006.

(123) Deutsch, D. S.; Lafaye, G.; Liu, D.; Chandler, B.; Williams, C. T.; Amiridis, M. D. Decomposition and Activation of Pt-Dendrimer Nanocomposites on a Silica Support. *Catal. Letters* **2004**, *97* (3–4), 139–143.

(124) Santiago-Morales, J.; Rosal, R.; Hernando, M. D.; Ulaszewska, M. M.; García-Calvo, E.; Fernández-Alba, A. R. Fate and Transformation Products of Amine-Terminated PAMAM Dendrimers under Ozonation and Irradiation. *J. Hazard. Mater.* **2014**, *266*, 102–113.

(125) Borodko, Y.; Thompson, C. M.; Huang, W.; Yildiz, H. B.; Frei, H.; Somorjai, G. A. Spectroscopic Study of Platinum and Rhodium Dendrimer (PAMAM G4OH) Compounds: Structure and Stability. *J. Phys. Chem. C* **2011**, *115* (11), 4757–4767.

(126) Lewera, A.; Timperman, L.; Roguska, A.; Alonso-Vante, N. Metal–Support

Interactions between Nanosized Pt and Metal Oxides (WO_3 and TiO_2) Studied Using X-Ray Photoelectron Spectroscopy. *J. Phys. Chem. C* **2011**, *115* (41), 20153–20159.

(127) Sasaki, K.; Adzic, R. R. Monolayer-Level Ru- and NbO_2-Supported Platinum Electrocatalysts for Methanol Oxidation. *J. Electrochem. Soc.* **2008**, *155* (2), B180–B186.

(128) Li, M.; Cullen, D. A.; Sasaki, K.; Marinkovic, N. S.; More, K.; Adzic, R. R. Ternary Electrocatalysts for Oxidizing Ethanol to Carbon Dioxide: Making Ir Capable of Splitting C-C Bond. *J. Am. Chem. Soc.* **2013**, *135* (1), 132–141.

(129) Li, M.; Zhou, W. P.; Marinkovic, N. S.; Sasaki, K.; Adzic, R. R. The Role of Rhodium and Tin Oxide in the Platinum-Based Electrocatalysts for Ethanol Oxidation to CO_2. *Electrochim. Acta* **2013**, *104*, 454–461.

(130) Ultraviolet-Ozone Surface Treatment. *Three Bond Technical News*. 1987, pp 1–10.

(131) UV/Ozone Cleaning of Surfaces. **1985**, *3* (3).

(132) *Nist X-Ray Photoelectron Spectroscopy Database, Version 4.1, (National Institute of Standards and Technology, Gaitherburg, 2012); Http://Srdata.Nist.Gov/Xps/.*

(133) Tokuhisa, H.; Zhao, M.; Baker, L. A.; Phan, V. T.; Dermody, D. L.; Garcia, M. E.; Peez, R. F.; Crooks, R. M.; Mayer, T. M. Preparation and Characterization of Dendrimer Monolayers and Dendrimer-Alkanethiol Mixed Monolayers Adsorbed to Gold. *J. Am. Chem. Soc.* **1998**, *120* (18), 4492–4501.

(134) Grabar, K. C.; Allison, K. J.; Baker, B. E.; Bright, R. M.; Brown, K. R.; Freeman, R. G.; Fox, a P.; Keating, C. D.; Musick, M. D.; Natan, M. J. Two-Dimensional Arrays of Colloidal Gold Particles: A Flexible Approach to Macroscopic Metal Surfaces. *Langmuir* **1996**, *12* (10), 2353–2361.

(135) Hill, C. M.; Kim, J.; Bard, A. J. Electrochemistry at a Metal Nanoparticle on a Tunneling Film: A Steady-State Model of Current Densities at a Tunneling Ultramicroelectrode. *J. Am. Chem. Soc.* **2015**, *137* (35), 11321–11326.

(136) Mistry, H.; Varela, A. S.; Kühl, S.; Strasser, P.; Cuenya, B. R. Nanostructured Electrocatalysts with Tunable Activity and Selectivity. *Nat. Rev. Mater.* **2016**, *1* (4), 16009.

(137) Cuenya, B. R. Metal Nanoparticle Catalysts Beginning to Shape-Up. *Acc. Chem. Res.* **2013**, *46* (8), 1682–1691.

(138) Kowal, A.; Li, M.; Shao, M.; Sasaki, K.; Vukmirovic, M. B.; Zhang, J.; Marinkovic, N. S.; Liu, P.; Frenkel, A. I.; Adzic, R. R. Ternary Pt/Rh/SnO_2 Electrocatalysts for Oxidizing Ethanol to CO_2. *Nat. Mater.* **2009**, *8* (4), 325–330.

(139) Zhou, W. P.; Axnanda, S.; White, M. G.; Adzic, R. R.; Hrbek, J. Enhancement in

Ethanol Electrooxidation by SnO_x Nanoislands Grown on Pt(111): Effect of Metal Oxide-Metal Interface Sites. *J. Phys. Chem. C* **2011**, *115* (33), 16467–16473.

(140) Li, M.; Kowal, A.; Sasaki, K.; Marinkovic, N.; Su, D.; Korach, E.; Liu, P.; Adzic, R. R. Ethanol Oxidation on the Ternary Pt-Rh-SnO_2/C Electrocatalysts with Varied Pt:Rh:Sn Ratios. *Electrochim. Acta* **2010**, *55* (14), 4331–4338.

(141) Zhou, W. P.; An, W.; Su, D.; Palomino, R.; Liu, P.; White, M. G.; Adzic, R. R. Electrooxidation of Methanol at SnO_x-Pt Interface: A Tunable Activity of Tin Oxide Nanoparticles. *J. Phys. Chem. Lett.* **2012**, *3* (22), 3286–3290.

(142) Konopka, D. A.; Li, M.; Artyushkova, K.; Marinkovic, N.; Sasaki, K.; Adzic, R.; Ward, T. L.; Atanassov, P. Platinum Supported on $NbRu_yO_z$ as Electrocatalyst for Ethanol Oxidation in Acid and Alkaline Fuel Cells. *J. Phys. Chem. C* **2011**, *115* (7), 3043–3056.

(143) Zhao, J.; Bradbury, C. R.; Fermín, D. J. Long-Range Electronic Communication between Metal Nanoparticles and Electrode Surfaces Separated by Polyelectrolyte Multilayer Films. *J. Phys. Chem. C* **2008**, *112* (17), 6832–6841.

(144) Castaneda, A. D.; Alligrant, T. M.; Loussaert, J. A.; Crooks, R. M. Electrocatalytic Amplification of Nanoparticle Collisions at Electrodes Modified with Polyelectrolyte Multilayer Films. *Langmuir* **2015**, *31* (2), 876–885.

(145) Kim, H. J.; Kearney, K. L.; Le, L. H.; Pekarek, R. T.; Rose, M. J. Platinum-Enhanced Electron Transfer and Surface Passivation through Ultrathin Film Aluminum Oxide (Al_2O_3) on Si(111)-CH_3 Photoelectrodes. *ACS Appl. Mater. Interfaces* **2015**, *7* (16), 8572–8584.

(146) Ostojic, N.; Crooks, R. M. Electrocatalytic Reduction of Oxygen on Platinum Nanoparticles in the Presence and Absence of Interactions with the Electrode Surface. *Langmuir* **2016**, *32*, 9727–9735.

(147) Albery, W. J.; Hitchman, M. L. *Ring-Disc Electrodes*; Clarendon Press: Oxford, 1971.

(148) Albery, W. J.; Jones, C. C.; Mount, A. R. New Hydrodynamic Methods. In *Comprehensive Chemical Kinetics, v29: New Techniques for the Study of Electrodes and Their Reactions*; Compton, R. G., Hamnet, A., Eds.; Elsevier: Amsterdam, 1989; Vol. 29, pp 129–148.

(149) Barnes, E. O.; Lewis, G. E. M.; Dale, S. E. C.; Marken, F.; Compton, R. G. Generator-Collector Double Electrode Systems: A Review. *Analyst* **2012**, *137* (5), 1068–1081.

(150) Compton, R. G.; Harding, M. S.; Pluck, M. R.; Atherton, J. H.; Brennan, C. M. Mechanism of Solid/Liquid Interfacial Reactions: The Dissolution of Benzoic Acid in Aqueous Solution. *J. Phys. Chem.* **1993**, *97* (40), 10416–10420.

(151) Unwin, P. R.; Compton, R. G. Effect of Carboxylic Acids on the Dissolution of Calcite in Aqueous Solution. Part 3.-Polymaleic Acid. *J. Chem. Soc. Faraday Trans.* **1990**, *86* (9), 1517–1525.

(152) Compton, R. G.; Gooding, J. J.; Sokirko, A. Chronoamperometry at Channel Electrodes: Analytical Theory of Transient Behaviour at Double Electrodes. *J. Appl. Electrochem.* **1996**, *26* (5), 463–469.

(153) Compton, R. G.; Coles, B. A.; Fisher, A. C. Chronoamperometry at Channel Electrodes: Theory of Double Electrodes. *J. Phys. Chem.* **1994**, *98* (9), 2441–2445.

(154) Thompson, M.; Klymenko, O. V; Compton, R. G. Modelling Homogeneous Kinetics in the Double Channel Electrode. *J. Electroanal. Chem.* **2005**, *576* (2), 333–338.

(155) Compton, R. G.; Stearn, G. M.; Unwin, P. R.; Barwise, A. J. Double Channel Electrodes and the Measurement of Heterogeneous Reaction Rates at the Solid-Liquid Interface. *J. Appl. Electrochem.* **1988**, *18* (4), 657–665.

(156) Bitziou, E.; Snowden, M. E.; Joseph, M. B.; Leigh, S. J.; Covington, J. A.; Macpherson, J. V; Unwin, P. R. Dual Electrode Micro-Channel Flow Cell for Redox Titrations: Kinetics and Analysis of Homogeneous Ascorbic Acid Oxidation. *J. Electroanal. Chem.* **2013**, *692* (0), 72–79.

(157) Snowden, M. E.; King, P. H.; Covington, J. A.; Macpherson, J. V; Unwin, P. R. Fabrication of Versatile Channel Flow Cells for Quantitative Electroanalysis Using Prototyping. *Anal. Chem.* **2010**, *82* (8), 3124–3131.

(158) Compton, R. G.; Pritchard, K. L.; Unwin, P. R.; Grigg, G.; Silvester, P.; Lees, M.; House, W. A. The Effect of Carboxylic Acids on the Dissolution of Calcite in Aqueous Solution. Part 1.—Maleic and Fumaric Acids. *J. Chem. Soc. Faraday Trans. 1* **1989**, *85* (12), 4335.

(159) Orton, R.; Unwin, P. R. Dolomite Dissolution Kinetics at Low PH: A Channel-Flow Study. *J. Chem. Soc. Faraday Trans.* **1993**, *89* (21), 3947–3954.

(160) Unwin, P. R. The ECE-DISP1 Problem: General Resolution via Double Channel Electrode Collection Efficiency Measurements. *J. Electroanal. Chem.* **1991**, *297* (1), 103–124.

(161) Channon, R. B.; Joseph, M. B.; Bitziou, E.; Bristow, A. W. T.; Ray, A. D.; Macpherson, J. V. Electrochemical Flow Injection Analysis of Hydrazine in an Excess of an Active Pharmaceutical Ingredient: Achieving Pharmaceutical Detection Limits Electrochemically. *Anal. Chem.* **2015**, *87* (19), 10064–10071.

(162) Bitziou, E.; Joseph, M. B.; Read, T. L.; Palmer, N.; Mollart, T.; Newton, M. E.; Macpherson, J. V. In Situ Optimization of PH for Parts-Per-Billion Electrochemical Detection of Dissolved Hydrogen Sulfide Using Boron Doped

Diamond Flow Electrodes. *Anal. Chem.* **2014**, *86* (21), 10834–10840.

(163) Dumitrescu, I.; Crooks, R. M. Effect of Mass Transfer on the Oxygen Reduction Reaction Catalyzed by Platinum Dendrimer Encapsulated Nanoparticles. *Proc. Natl. Acad. Sci.* **2012**, *109* (29), 11493–11497.

(164) Anderson, M. J.; Crooks, R. M. High-Efficiency Generation-Collection Microelectrochemical Platform for Interrogating Electroactive Thin Films. *Anal. Chem.* **2014**, *86* (19), 9962–9969.

(165) Alden, J. A.; Compton, R. G. Hydrodynamic Voltammetry with Channel Microband Electrodes: Axial Diffusion Effects. *J. Electroanal. Chem.* **1996**, *404* (1), 27–35.

(166) Compton, R. G.; Winkler, J. Hydrodynamic Voltammetry with Channel Microband Electrodes - Alternating-Current Impedance Measurements. *J. Phys. Chem.* **1995**, *99* (14), 5029–5034.

(167) Compton, R. G.; Wellington, R. G.; Dobson, P. J.; Leigh, P. A. Hydrodynamic Voltammetry with Channel Microband Electrodes: Resolution of ECE and DISP1 Processes. *J. Electroanal. Chem.* **1994**, *370* (1–2), 129–133.

(168) Compton, R. G.; Fisher, A. C.; Wellington, R. G.; Dobson, P. J.; Leigh, P. A. Hydrodynamic Voltammetry with Microelectrodes: Channel Microband Electrodes; Theory and Experiment. *J. Phys. Chem.* **1993**, *97* (40), 10410–10415.

(169) *Rotating Disk Electrodes: E2, E3 and E5 Series*; Pine Instrument Company: Raleigh, NC 27617.

(170) *Rotating Ring-Disk Electrodes: MT28, MT29, E6 and E7 Series*; Pine Instrument Company: Raleigh, NC 27617.

(171) Compton, R. G.; Harland, R. G.; Unwin, P. R.; Waller, A. M. Rotating-Disc Electrodes. ECE and DISP1 Processes. *J. Chem. Soc. Faraday Trans. 1 Phys. Chem. Condens. Phases* **1987**, *83* (4), 1261–1268.

(172) Cooper, J. A.; Compton, R. G. Channel Electrodes — A Review. *Electroanalysis* **1998**, *10* (3), 141–155.

(173) Compton, R. G.; Coles, B. A.; Gooding, J. J.; Fisher, A. C.; Cox, T. I. Chronoamperometry at Channel Electrodes. Experimental Applications of Double Electrodes. **1994**, *1*, 2446–2451.

(174) Adams, R. N. *Electrochemistry at Solid Electrodes*; Marcel Dekker, inc.: New York, 1969.

(175) Unwin, P. R.; Compton, R. G. The Use of Channel Electrodes in the Investigation of Interfacial Reaction Mechanisms. In *Comprehensive Chemical Kinetics*; Compton, R. G., Ed.; Elsevier, 1989; Vol. 29, pp 173–296.

(176) Albery, W. J.; Bruckenstein, S. Ring-Disc Electrodes. Part 5.-First-Order Kinetic Collection Effciencies at the Ring Electrode. *Trans. Faraday Soc.* **1966**, *62* (0), 1946–1954.

(177) Compton, R. G.; Banks, C. E. *Understanding Voltammetry*; World Scientific Publishing Co.: Singapore, 2007.

(178) Shah, R. K.; London, A. L. *Laminar Flow Forced Convection in Ducts: A Source Book for Compact Heat Exchanger Analytical Data*; Thomas F Irvine, J., Hartnett, J. P., Eds.; Academic Press: New York, 1978; Vol. Supplement.

(179) Levich, V. G.; Scripta Technica, I. *Physiochemical Hydrodynamics*; Prentice-Hall, Inc.: Englewood Cliffs, N.J., 1962.

(180) Konopka, D. A.; Li, M.; Artyushkova, K.; Marinkovic, N.; Sasaki, K.; Adzic, R.; Ward, T. L.; Atanassov, P. Platinum Supported on $NbRu_yO_z$ as Electrocatalyst for Ethanol Oxidation in Acid and Alkaline Fuel Cells. *J. Phys. Chem. C* **2011**, *115* (7), 3043–3056.

(181) Nie, L.; Meng, A.; Yu, J.; Jaroniec, M. Hierarchically Macro-Mesoporous Pt/γ-Al_2O_3 Composite Microspheres for Efficient Formaldehyde Oxidation at Room Temperature. *Sci. Rep.* **2013**, *3* (1), 3215.

(182) Markovic, N. M.; Schmidt, T. J.; Stamenković, V.; Ross, P. N. Oxygen Reduction Reaction on Pt and Pt Bimetallic Surfaces: A Selective Review. *Fuel Cells* **2001**, *1* (2), 105–116.

(183) Zhang, L.; Wei, M.; Wang, S.; Li, Z.; Ding, L.-X.; Wang, H. Highly Stable PtP Alloy Nanotube Arrays as a Catalyst for the Oxygen Reduction Reaction in Acidic Medium. *Chem. Sci.* **2015**, *6* (5), 3211–3216.

(184) Luo, J.; Njoki, P. N.; Lin, Y.; Wang, L.; Zhong, C. J. Activity-Composition Correlation of AuPt Alloy Nanoparticle Catalysts in Electrocatalytic Reduction of Oxygen. *Electrochem. commun.* **2006**, *8* (4), 581–587.

(185) Chen, W.; Ny, D.; Chen, S. SnO_2–Au Hybrid Nanoparticles as Effective Catalysts for Oxygen Electroreduction in Alkaline Media. *J. Power Sources* **2010**, *195* (2), 412–418.

(186) Vayenas, C. G. Promotion, Electrochemical Promotion and Metal-Support Interactions: Their Common Features. *Catal. Letters* **2013**, *143* (11), 1085–1097.

(187) Willinger, M. G.; Zhang, W.; Bondarchuk, O.; Shaikhutdinov, S.; Freund, H. J.; Schlogl, R. A Case of Strong Metal-Support Interactions: Combining Advanced Microscopy and Model Systems to Elucidate the Atomic Structure of Interfaces. *Angew. Chemie - Int. Ed.* **2014**, *53* (23), 5998–6001.

(188) Tauster, S. J.; Fung, S. C.; Garten, R. L. Strong Metal-Support Interactions. Group 8 Noble Metals Supported on Titanium Dioxide. *J. Am. Chem. Soc.* **1978**, *100* (1),

170–175.

(189) Zhang, Z.; Yang, S.; Dou, M.; Liu, H.; Gu, L.; Wang, F. Systematic Study of Transition-Metal (Fe, Co, Ni, Cu) Phthalocyanines as Electrocatalysts for Oxygen Reduction and Their Evaluation by DFT. *RSC Adv.* **2016**, *6* (71), 67049–67056.

(190) Duan, Z.; Henkelman, G. CO Oxidation at the Au/TiO_2 Boundary: The Role of the Au/Ti5c Site. *ACS Catal.* **2015**, *5* (3), 1589–1595.

(191) Kim, H. Y.; Lee, H. M.; Henkelman, G. CO Oxidation Mechanism on CeO_2-Supported Au Nanoparticles. *J. Am. Chem. Soc.* **2012**, *134* (3), 1560–1570.

(192) Xiaoming, G.; Sumboja, A.; Wuu, D.; An, T.; Li, B.; Goh, F. W. T.; Hor, T. S. A.; Zong, Y.; Liu, Z. Oxygen Reduction in Alkaline Media: From Mechanisms to Recent Advances of Catalysts. *ACS Catal.* **2015**, *5* (8), 4643–4667.

(193) Wu, Y. Y.; Mashayekhi, N. A.; Kung, H. H. Au–metal Oxide Support Interface as Catalytic Active Sites. *Catal. Sci. Technol.* **2013**, *3* (11), 2881.

(194) Yu, L.; Liu, Y.; Yang, F.; Evans, J.; Rodriguez, J. A.; Liu, P. CO Oxidation on Gold-Supported Iron Oxides: New Insights into Strong Oxide-Metal Interactions. *J. Phys. Chem. C* **2015**, *119* (29), 16614–16622.

(195) Hsieh, B. J.; Tsai, M. C.; Pan, C. J.; Su, W. N.; Rick, J.; Chou, H. L.; Lee, J. F.; Hwang, B. J. Tuning Metal Support Interactions Enhances the Activity and Durability of TiO_2-Supported Pt Nanocatalysts. *Electrochim. Acta* **2017**, *224*, 452–459.

(196) Axnanda, S.; Zhou, W.-P.; White, M. G. CO Oxidation on Nanostructured SnO_x/Pt(111) Surfaces: Unique Properties of Reduced SnOx. *Phys. Chem. Chem. Phys.* **2012**, *14*, 10207–10214.

(197) Moghaddam, R. B.; Pickup, P. G. Support Effects on the Oxidation of Ethanol at Pt Nanoparticles. *Electrochim. Acta* **2012**, *65*, 210–215.

(198) Dole, H. A. E.; Safady, L. F.; Ntais, S.; Couillard, M.; Baranova, E. A. Electrochemically Enhanced Metal-Support Interaction of Highly Dispersed Ru Nanoparticles with a CeO_2 Support. *J. Catal.* **2014**, *318*, 85–94.

(199) Zhou, W. P.; Axnanda, S.; White, M. G.; Adzic, R. R.; Hrbek, J. Enhancement in Ethanol Electrooxidation by SnO_x Nanoislands Grown on Pt (111): Effect of Metal Oxide–Metal Interface Sites. *J. Phys. Chem. C* **2011**, *115* (33), 16467–16473.

(200) Kowal, A.; Li, M.; Shao, M.; Sasaki, K.; Vukmirovic, M. B.; Zhang, J.; Marinkovic, N. S.; Liu, P.; Frenkel, A. I.; Adzic, R. R. Ternary Pt/Rh/SnO2 Electrocatalysts for Oxidizing Ethanol to CO_2. *Nat. Mater.* **2009**, *8* (4), 325–330.

(201) Zhou, W.-P.; An, W.; Su, D.; Palomino, R.; Liu, P.; White, M. G.; Adzic, R. R. Electrooxidation of Methanol at SnO_x-Pt Interface: A Tunable Activity of Tin

Oxide Nanoparticles. *J. Phys. Chem. Lett.* **2012**, *3*, 3286–3290.

(202) Jimenez-Morales, I.; Cavaliere, S.; Jones, D.; Rozière, J. Strong Metal-Support Interaction Improves Activity and Stability of Pt Electrocatalysts on Doped Metal Oxides. *Phys. Chem. Chem. Phys.* **2018**, *20*, 8765.

(203) Mistry, H.; Varela, A. S.; Kühl, S.; Strasser, P.; Cuenya, B. R. Nanostructured Electrocatalysts with Tunable Activity and Selectivity. *Nat. Rev. Mater.* **2016**, 1–15.

(204) Anderson, M. J.; Ostojic, N.; Crooks, R. M. Microelectrochemical Flow Cell for Studying Electrocatalytic Reactions on Oxide-Coated Electrodes. *Anal. Chem.* **2017**, *89* (20), 11027–11035.

(205) Zheng, N.; Stucky, G. D.; Liu, P. P.; Qin, R.; Fu, G.; Zheng, N.; Zhang, L. L. L. J. L.; Anderson, R. M.; Crooks, R. M.; Henkelman, G.; et al. Nanoparticle Mediated Electron Transfer across Organic Layers: From Current Understanding to Applications. *J. Am. Chem. Soc.* **2013**, *112* (3), 16467–16473.

(206) Zhao, M.; Sun, L.; Crooks, R. M. Preparation of Cu Nanoclusters within Dendrimer Templates. *J. Am. Chem. Soc.* **1998**, *120* (19), 4877–4878.

(207) Lhenry, S.; Jalkh, J.; Leroux, Y. R.; Ruiz, J.; Ciganda, R.; Astruc, D.; Hapiot, P. Tunneling Dendrimers. Enhancing Charge Transport through Insulating Layer Using Redox Molecular Objects. *J. Am. Chem. Soc.* **2014**, *136* (52), 17950–17953.

(208) Myers, V. S.; Weir, M. G.; Carino, E. V.; Yancey, D. F.; Pande, S.; Crooks, R. M. Dendrimer-Encapsulated Nanoparticles: New Synthetic and Characterization Methods and Catalytic Applications. *Chem. Sci.* **2011**, *2* (9), 1632.

(209) Oh, S. K.; Niu, Y.; Crooks, R. M. Size-Selective Catalytic Activity of Pd Nanoparticles Encapsulated within End-Group Functionalized Dendrimers. *Langmuir* **2005**, *21* (22), 10209–10213.

(210) Kresse, G.; Hafner, J. *Ab Initio* Molecular Dynamics for Liquid Metals. *Phys. Rev. B* **1993**, *47* (1), 558–561.

(211) Kresse, G.; Furthmüller, J. Efficiency of Ab-Initio Total Energy Calculations for Metals and Semiconductors Using a Plane-Wave Basis Set. *Comput. Mater. Sci.* **1996**, *6* (1), 15–50.

(212) Kresse, G.; Furthmüller, J. Efficient Iterative Schemes for *Ab Initio* Total-Energy Calculations Using a Plane-Wave Basis Set. *Phys. Rev. B* **1996**, *54* (16), 11169–11186.

(213) Perdew, J. P.; Wang, Y. Accurate and Simple Analytic Representation of the Electron-Gas Correlation Energy. *Phys. Rev. B* **1992**, *45* (23), 13244–13249.

(214) Blöchl, P. E. Projector Augmented-Wave Method. *Phys. Rev. B* **1994**, *50* (24),

17953–17979.

(215) Dudarev, S. L.; Botton, G. A.; Savrasov, S. Y.; Humphreys, C. J.; Sutton, A. P. Electron-Energy-Loss Spectra and the Structural Stability of Nickel Oxide: An LSDA+U Study. *Phys. Rev. B* **1998**, *57* (3), 1505–1509.

(216) Singh, A. K.; Janotti, A.; Scheffler, M.; Van de Walle, C. G. Sources of Electrical Conductivity in SnO_2. *Phys. Rev. Lett.* **2008**, *101* (5), 055502.

(217) Henkelman, G.; Arnaldsson, A.; Jónsson, H. A Fast and Robust Algorithm for Bader Decomposition of Charge Density. *Comput. Mater. Sci.* **2006**, *36* (3), 354–360.

(218) Tang, W.; Sanville, E.; Henkelman, G. A Grid-Based Bader Analysis Algorithm without Lattice Bias. *J. Phys. Condens. Matter* **2009**, *21* (8), 084204.

(219) Mulheran, P. A.; Harding, J. H. The Stability of SnO_2 Surfaces. *Model. Simul. Mater. Sci. Eng.* **1992**, *1* (1), 39–43.

(220) Monkhorst, H. J.; Pack, J. D. Special Points for Brillouin-Zone Integrations. *Phys. Rev. B* **1976**, *13* (12), 5188–5192.

(221) Nørskov, J. K.; Rossmeisl, J.; Logadottir, A.; Lindqvist, L.; Kitchin, J. R.; Bligaard, T.; Jónsson, H. Origin of the Overpotential for Oxygen Reduction at a Fuel-Cell Cathode. *J. Phys. Chem. B* **2004**, *108* (46), 17886–17892.

(222) Su, H.-Y.; Gorlin, Y.; Man, I. C.; Calle-Vallejo, F.; Nørskov, J. K.; Jaramillo, T. F.; Rossmeisl, J. Identifying Active Surface Phases for Metal Oxide Electrocatalysts: A Study of Manganese Oxide Bi-Functional Catalysts for Oxygen Reduction and Water Oxidation Catalysis. *Phys. Chem. Chem. Phys.* **2012**, *14* (40), 14010.

(223) Hansen, H. A.; Rossmeisl, J.; Nørskov, J. K. Surface Pourbaix Diagrams and Oxygen Reduction Activity of Pt, Ag and Ni(111) Surfaces Studied by DFT. *Phys. Chem. Chem. Phys.* **2008**, *10* (25), 3722.

(224) Trindell, J. A.; Clausmeyer, J.; Crooks, R. M. Size Stability and H_2/CO Selectivity for Au Nanoparticles during Electrocatalytic CO2Reduction. *J. Am. Chem. Soc.* **2017**, *139* (45), 16161–16167.

(225) Duan, Z.; Henkelman, G. CO Oxidation at the Au/TiO_2 Boundary: The Role of the Au/Ti_{5c} Site. *ACS Catal.* **2015**, *5* (3), 1589–1595.

(226) Duan, Z.; Henkelman, G. Calculations of CO Oxidation over a Au/TiO_2 Catalyst: A Study of Active Sites, Catalyst Deactivation, and Moisture Effects. *ACS Catal.* **2018**, *8* (2), 1376–1383.

(227) Kılıç, Ç.; Zunger, A. Origins of Coexistence of Conductivity and Transparency in SnO_2. *Phys. Rev. Lett.* **2002**, *88* (9), 095501.

(228) Gooding, J. J.; Alam, M. T.; Barfidokht, A.; Carter, L. Nanoparticle Mediated Electron Transfer across Organic Layers: From Current Understanding to Applications. *J. Braz. Chem. Soc.* **2014**, *25* (3), 418–426.